**PhD Thesis**


**ADVANCEMENTS IN NUCLEAR WASTE ASSAY**



**Debbie Curtis**


**Supervisor: Dr. M. Wormald**


**Supervisor: Dr. P. Norman**



**Academic Years 2004-2007**


UNIVERSITY OF
BIRMINGHAM

CANBERRA

# ABSTRACT

The research described in this thesis is directed at advancing the state of the practice of the non-destructive gamma-ray assay of nuclear waste containers. A number of potentially accuracy-limiting issues were identified and addressed, resulting in new developments which were implemented on an instrument prior to entering it into service.

A set of Pu reference sources used for experimental data have been studied to determine the internal composition (density and fill height) of the sources to assist with validation of a point kernel model. This model has been used to observe the behaviour of gamma-rays in lumps of fissile material from plutonium over the mass range 0.001g to 350g, for a number of densities corresponding to Pu, $PuO_2$ and $PuF_3$. Established lump corrections have been analysed and have been found to produce large over- and under-corrected results for the range of masses. Due to the inadequacies of current techniques, a new Pu self-absorption correction method has been developed using the data from numerical simulations, allowing nature to reveal the correlations rather than traditional approaches based upon approximate models. For a 25g 1cm-high Pu flat-plate of density 15g.cm$^{-3}$, the developed Pu correction produces a result of $(24.9 \pm 8.8)$g compared to $(19.5 \pm 0.9)$g for the Fleissner 2-line method, and $(14.7 \pm 0.4)$g for the Infinite Energy Extrapolation method.

The developed Pu correction method has been extended to the application of uranium lumps in waste matrices, provided the enrichment of the sample is known or may be determined via sophisticated isotopic analysis methods such as MGAU or FRAM. The U self-absorption correction method has been found to produce results within 30% of the true mass of the sample for the lumps studied.

An analysis of 'real drum' effects has been performed, including the revisiting of the Total Measurement Uncertainty (incorporating the uncertainty components of the new Pu and U self-absorption corrections) and results from known sources placed in artificial inhomogeneous waste matrices assayed inside a Canberra Auto Q2 system.

# CONTENTS

# FIGURES

# TABLES

# NOMENCLATURE

| | |
|---|---|
| BEGe | - Broad Energy Germanium detector |
| CSN | - Count Sequence Number |
| DMSS | - Dual Multi-Spectrum Scaling |
| DU | - Depleted uranium (<0.7% $^{235}$U) i.e. less than the natural abundance of $^{235}$U |
| FRAM | - Fixed-Energy Response Function Analysis with Multiple Efficiency, an isotopics software code |
| FWHM | - Full Width Half Maximum |
| GAA | - Genie 2000's Gamma Acquisition and Analysis program |
| Ge(Li) | - Lithium drifted germanium |
| HDPE | - High Density Polyethylene |
| HEU | - High enrichment uranium (~93% $^{235}$U) |
| HPGe | - High purity Germanium |
| HLW | - High Level Waste |
| HTGR | - High Temperature Gas Reactor |
| IAEA | - International Atomic Energy Agency |
| IEE | - Infinite Energy Extrapolation method |
| IEU | - Intermediate enrichment uranium (~40% $^{235}$U) |
| ILW | - Intermediate Level Waste |
| ISOCS | - Canberra's *In Situ* Object Counting System/Software |
| LANL | - Los Alamos National Laboratory |
| LLW | - Low Level Waste |
| MCNP | - Monte Carlo N-Particle transport code developed by LANL |
| MDA | - Minimum Detectable Activity |
| MGA | - Multiple Group Analysis, an isotopics software code |
| MGAU | - Multiple Group Analysis for Uranium, an isotopics software code |
| NaI(Tl) | - Thalium activated sodium iodide |
| NDA2000 | - Canberra's waste assay software for the Genie 2000 family of systems |
| NDE | - Non-Destructive Examination |

| | |
|---|---|
| NID | - Nuclide Identification |
| Nirex | - Nuclear Industry Radioactive Waste Executive |
| NUDS | - Non-Uniformity Detection Software |
| PDT | - Pacific Daylight Time |
| PNCC | - Passive Neutron Coincidence Counter |
| $^{240}Pu_{eff}$ | - The effective $^{240}Pu$ mass of a sample from PNCC assay. $^{240}Pu$ is typically the primary source of fission neutrons from Pu in the fuel cycle |
| $R^2$ | - A statistical measure between 0 and 1 indicating how well a regression line approximates to data points |
| ROI | - Region of Interest in a gamma spectrum |
| RTR | - Real Time Radiography |
| SAC | - Self-Absorption Correction |
| SAF | - Self-Absorption Factor |
| SGS | - Segmented Gamma-Ray Scanner |
| SILWAS | - Solid ILW Assay System |
| SNM | - Special Nuclear Material |
| TGS | - Tomographic Gamma Scanner |
| TMU | - Total Measurement Uncertainty |
| VLLW | - Very Low Level Waste |
| VWA | - Volume Weighted Average |
| Z | - Atomic number |

# 1 INTRODUCTION

This work addresses a number of issues with current gamma techniques for Non-Destructive Assay (NDA) of nuclear waste. Modelling is used to form an understanding that leads to improve algorithms and correction methodologies, with the aim of advancing the science of NDA.

## 1.1 Background

### 1.1.1 What is Nuclear Waste?

Nuclear Waste is defined as: "any material contaminated by or incorporating radioactivity above thresholds defined in legislation is known as radioactive waste." [1]. It originates from a number of different sources such as power stations, nuclear weapons processing, hospitals, science laboratories etc, in a number of chemical forms and has four main types in the International Atomic Energy Authority [2]: high, intermediate, low and very low level wastes [3].

High level waste (HLW) consists mainly of spent fuel and waste from reprocessing of nuclear fuels in liquid form. High level waste is highly radioactive and consequently has a high thermal power output (typically greater than 2kW/m$^3$) which must be taken into account for storage and hence must be stored behind appropriate shielding. It can be made into solid glass waste through the vitrification process.

Intermediate level waste (ILW) consists of material that is more radioactive than LLW boundaries but that does not require heat to be removed (thermal power output is less than 2kW/m$^3$). It is often in the form of irradiated material from reactors, contaminated equipment from decommissioning, chemical sludges, fuel cans etc. The concentration is > 4GBq/g of α or 12GBq/g of β/γ. Pending a suitable repository ILW is typically stored in dry, above ground facilities. Pu contaminated materials often fall into the ILW category but may have low surface doses depending on their origin.

Below this concentration the waste is classified as Low Level Waste (LLW). LLW consists typically of material from active areas such as protective clothing (e.g. gloves, tools, filters etc)

that can not be disposed of in normal waste streams and is typically sent to the Drigg Disposal Facility [4] after compaction or incineration. It requires significantly less shielding during transport and storage than ILW.

Very Low Level Waste (VLLW) may be disposed of in ordinary waste streams i.e. a landfill site. VLLW is defined such that each $0.1m^3$ of material must contain less than 0.4MBq of β/γ activity [2].

## 1.1.2 Nuclear Waste Characteristics

For the algorithms in question in this thesis we are mainly concerned with the assay of sealed drums of solid waste which need to be categorised into either ILW or LLW. This is performed for cost effective storage, or storage in terms of criticality or danger to humans and the environment which may occur if the waste is stored incorrectly.

The storage containers may consist of a variety of different thickness drums (mostly 205 litre steel drums) with a range of liners (HDPE or steel). The radioactive material may be contained within matrices of various compositions: paper/plastics/steel/lead and may range from milligrams to several hundred grams (to cover the operational criticality limit of 120g for fissile material) of Pu and U, possibly in close contact with low-Z elements.

## 1.2 Measurement Methods

Nuclear waste may be measured using either Destructive Analysis (DA) or Non-Destructive Assay. These are defined in the IAEA Safeguards Glossary [4] as:

- DA - "determination of nuclear material content and, if required, of the isotopic composition of chemical elements present in the sample. Destructive analysis normally involves destruction of the physical form of the sample."
- NDA - "a measurement of the nuclear material content or of the element or isotopic concentration of an item without producing significant physical or chemical changes in the item."

Destructive Analysis uses a sample of waste as a representative of a larger group; it involves transporting the sample to an appropriate laboratory for analysis, creates secondary waste and is often relatively time consuming. Although the laboratory analysis of the sample is more accurate than NDA, NDA has the benefit of measuring the whole item (for example, a drum) *in situ* in real time without disturbing the waste. It is non-intrusive and does not involve opening of the container.

For the purpose of this PhD we are concerned only with Non-Destructive Assay methods. NDA may be categorised as either passive (from spontaneous emissions of gamma-rays or neutrons) or active (from stimulated emission) analysis. Within the passive category there are a number of techniques such as calorimetry, PNCC (Passive Neutron Coincidence counting) or gamma-ray spectrometry.

X-rays may also be used to provide information on the nature of the waste e.g. using an RTR system (real-time radiography) for Non-Destructive Examination (NDE). NDE is mostly concerned with checking the waste for prohibited items and for verifying packing information or quality objectives. It can also serve to estimate the relative abundance of metals etc. This may be fed into qualitative NDA methods although on its own NDE is not regarded as assay.

## 1.2.1 Calorimetry

Calorimetry is the study of energy exchange between the reaction system and its environment. In terms of radiometric calorimetry this involves measuring the thermal power output for heat-producing special nuclear material (SNM), such as Pu, that are not generally be affected by the matrix or any shielding.

To measure the heat output of a Pu sample, for example, the sample would be placed into an insulated cylinder wrapped in a resistive wire inside a heat bath at constant temperature. This cylinder would be used as part of a Wheatstone bridge along with an identical control cylinder. The change in resistance can be used to give an accurate measurement of the heat output. The procedure generally takes several hours to obtain an accurate measurement and is less useful for

samples with a lower heat output, such as $^{235}$U. Also it is not possible to distinguish between nuclides using this method and so it must be used with an isotopic measurement.

Calorimetry is not currently used for drummed waste due to the large time required for the waste to reach equilibrium (around 24h per item) and its poor sensitivity at the mg level, and so this method is not considered further here. This method is typically applied to bulk products, weapon components or to high ($\alpha$,n) residues in small containers.

## 1.2.2 Passive Neutron Coincidence Counting

PNCC uses the fact that neutrons from induced or spontaneous fission are emitted in groups. $^{238,240,242}$Pu have sufficiently large spontaneous fission neutron emission rates to allow detection, and the count rate of these correlated neutrons (for fixed isotope ratios) will be a function of the total Pu mass of the sample. The PNCC system consists of a number of $^{3}$He proportional counter tubes embedded in polyethylene (the moderator) which will thermalise the neutrons so that they may be captured by the $^{3}$He tubes. The captured neutrons produce a pulse train which is then analysed by a shift register able to distinguish between isolated (from ($\alpha$,n) reactions) and correlated neutrons, to determine the $^{240}$Pu$_{eff}$ mass of the sample [5].

## 1.2.3 Gamma-Ray Spectrometry

Gamma-ray spectrometry uses the fact that, for a particular Special Nuclear Material (SNM) isotope the emission of gamma-rays is proportional to the mass of that isotope in the assayed sample. However the emitted radiation may not all be detected by the detector. The assay result is affected by the energy dependent full energy peak efficiency of the detector and is also impeded by the material in its path to the detector such as the measurement container, matrix and also within the source itself (self-absorption). Some of these effects may be corrected with efficiency and transmission calibrations. These are explained in more detail in Section 2.

## 1.3  Areas of Study

The following sections briefly outline the three areas of non-destructive analysis using gamma-rays that have been studied in this work.

Previous studies have observed an over-correction of 50% whilst measuring sources on a Canberra Segmented Gamma Scanner (SGS). These results prompted a study into the current Fleissner correction method and modelling of a range of size and shape Pu sources, which has shown it to over-correct by a factor of 1.5 at intermediate masses and under-correct at higher masses. Other methods such as the Infinite Energy Extrapolation method have also been analysed and their performance has been found to be inadequate over the range of lump sizes and shapes that may be present in a typical waste drum. The motivation behind the present study was to find a more generic approach with broader applicability [6] and an improved performance compared to the current techniques.

Correction methods such as the Fleissner and Infinite Energy Extrapolation methods require some degree of approximation and attempt to constrain the behaviour of the self-absorption to fit a simple, reproducible form. However, analysis has shown that this is not possible and so a method has been developed that involves calculating the behaviour of a large range of lump types (shapes, compounds and densities) and letting the model reveal the correlations. As a result, a new correction technique is proposed by the author in section 3 based on modelled data to correct for Pu self-absorption using the $^{239}$Pu apparent masses at 129 keV and 414 keV.

Currently uranium self-absorption corrections are not applied; one possible technique to account for self-absorption involves incorporating a "lump" parameter into the estimate of the Total Measurement Uncertainty (TMU) to account for the case where all the U in a sample is concentrated into a single spherical lump (see section 5.4). The Pu self-absorption correction method developed in section 3 has been successfully adapted to be used for U (in section 4) using the $^{235}$U 186 keV and $^{238}$U 1001 keV lines respectively, and assuming that the enrichment is known or can be estimated.

The TMU of an assayed result encompasses all significant sources of uncertainty within the measurement and post-analysis process [7]. Current techniques provide spatial variation corrections, however these assume the photopeak may be approximated to a Gaussian distribution and only allow for the correction parameters to be inputted for one particular energy per assay. In section 5, the contribution to spatial uncertainties has been explored as a function of energy allowing for the asymmetry of the probability distribution. The method of combining uncertainties from different correction techniques for collimated and uncollimated segments has also been revisited, including the method of combination of the Pu and U self-absorption methods.

The work in section 5 has been performed as part of a project team at Canberra UK Ltd. for the SILWAS project. The contribution from the author has involved modelling of the gamma source spatial distribution and matrix effects with the Pu SAC algorithm, plus performing Pu and U measurements on the AQ2 as part of CUK Factory Acceptance Tests. Data analysis has been performed on measured results using NDA2000 and the dedicated SILWAS post analysis engines software including an early version of the developed Pu SAC and U SAC algorithms.

# 2 PRINCIPLES OF GAMMA RAY ASSAY

The purpose of this section is to outline the main principles of gamma-radiation, their interactions with matter and the basic concepts of gamma assay which are used throughout this report.

## 2.1 Gamma-Ray Emission

The emission of a gamma ray generally occurs when an excited nucleus undergoes a transition to a lower energy state of the same nuclide [8]. Their emission usually occurs after another process has occurred in the nucleus leaving it in an excited state, e.g. after $\beta$ or $\alpha$ decay. High energy electromagnetic photons may also be produced by other processes, for example bremsstrahlung or annihilation interactions.

Gamma rays provide opportunities for detection, since unlike charged particles they cannot be deflected by electric/magnetic fields and they are much more penetrating to matter (10-100 times more penetrating that $\beta$ particles [9]). The interactions of the uncharged radiation ($\gamma$ rays) with matter (see Section 2.2) are used in the detection process since they transfer their energy to charged particles which are then detected via excitation and ionisation in the detector.

## 2.2 Interactions with Matter

### 2.2.1 Interaction Mechanisms

The three most important interaction mechanisms between gamma rays and matter are Compton scattering, pair production and photoelectric absorption, and all these methods result in the conversion of gamma photon energy to electron energy.

Compton scattering ([9], [10]) occurs when an incident gamma-ray photon interacts with a target electron via the electromagnetic force and consequently transfers a fraction of its energy to the recoil electron. The incident photon and the electron may be scattered through any angle and so any fraction of the gamma-ray energy may be transferred above a minimum corresponding to $180^{\circ}$ scattering. The electron is considered to be "free" although it is in fact bound to the nucleus in the outer shell.

In the presence of a nucleus, a gamma-ray photon may be converted into an electron-positron pair. This interaction is known as pair production and can only occur if the incident gamma-ray energy is at least double the electron rest mass i.e. 1.02 MeV; the excess energy is used for the kinetic energy of the created pair.

The photoelectric absorption process may occur when a gamma-ray photon is incident upon an atom and is absorbed, and a photoelectron is emitted. This emission creates a vacancy in the shell that was occupied by the electron which is filled by a transition of an electron from another shell, consequently releasing a characteristic X-ray.

## 2.2.2 Attenuation of Gamma-Rays

If a narrow beam of gamma radiation is incident on a detector, the radiation may be scattered or absorbed by the three interactions described above. The ratio of the number of photons that reaches the detector ($I$) to the number that would reach the detector without an absorber ($I_o$) is given by:

$$\frac{I}{I_o} = e^{-\mu.\rho.x}$$ **Eqn. 1**

where $\mu$ is the mass attenuation coefficient (equal to the linear attenuation coefficient divided by $\rho$), $\rho$ is the density of the absorbing material and $x$ is the distance travelled through that material. $\mu$ is a property of an element with a γ-energy dependence and these are well documented [11], [12]. $\mu$s for compound or mixed element materials can be derived by weight fraction weighted summing.

For the purpose of the point source model used for analysis (section 3.2) and the data in Figure 6 the Genie ISOCS mass attenuation coefficient data have been used [13]. Although the original source of these data is not known for certain, it is thought to have been extracted from MCNP V.4B [14]. The data in the MCNP libraries consist of attenuation coefficient tables (separated into contributions for different interactions) versus energy at discrete energy ordinates per atomic number (element). The ISOCS program has adapted these data so that the different interaction contributions are summed and then fitted to polynomials rather than using table interpolation

within ISOCS. If there is a K-edge in the energy range then multiple polynomials are used. ISOCS uses total minus coherent scattering mass attenuation coefficients since for many geometries, in and out scattering without energy loss cancels so that coherent scattering may be ignored.

One of the 'best' (current and comprehensive) sources of mass attenuation coefficient data is the NIST XCOM database [15]. This database may be used to calculate photon cross-sections and total attenuation coefficients, plus individual coherent and incoherent scattering, photoelectric absorption and pair production cross-sections for any element compound or mixture within the energy range 1 keV to 100 GeV.
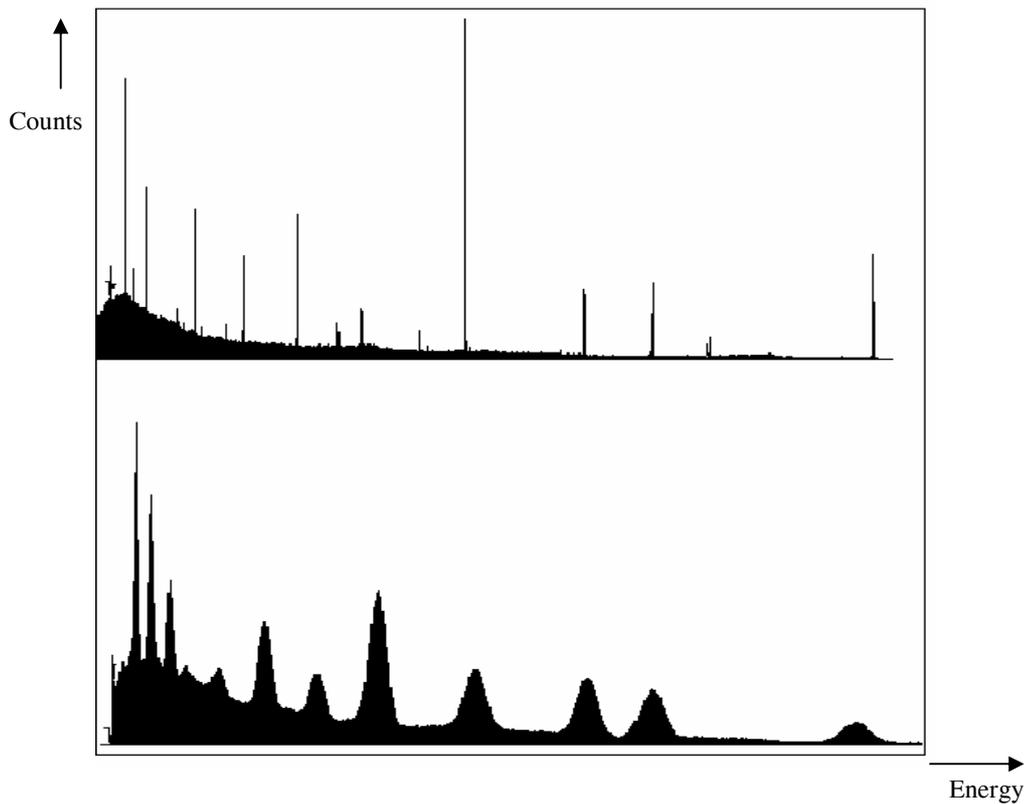


**Figure 1: Example of γ specta from NaI(Tl) (bottom) and Ge detectors (top) showing the higher resolution of the Ge detector compared to NaI(Tl) for a similar energy range [16].**

## 2.3   Gamma Spectra

The two main types of detectors used for gamma radiation detection in waste assay are the Ge semi-conductors and NaI(Tl) scintillator detectors. The NaI(Tl) detector has a higher detection efficiency but the Ge detector has a much better energy resolution (allowing a nuclide identification to be performed for complex waste spectra) and so compensates to have a comparable detection limit.

Figure 1 and Figure 2 show examples of Ge and NaI(Tl) spectra. As shown, the individual peaks of the Ge spectrum may be easily resolved in this example.
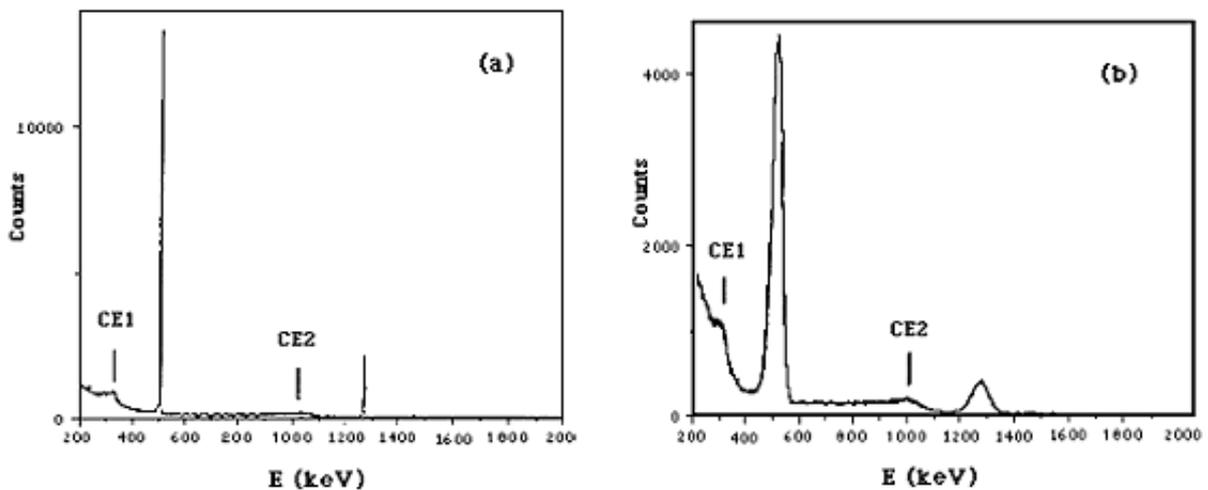


**Figure 2: Gamma ray spectra of $^{22}$Na using (a) a Ge(Li) and (b) a NaI(Tl) detector [17].**

Figure 2 compares the spectra over the same energy range for a $^{22}$Na source. The $^{22}$Na peak is seen at 1275 keV and also because $^{22}$Na is a $\beta^+$ emitter annihilation radiation is observed at 511 keV. Additionally two other features are labelled as CE1 and CE2 - the Compton edges. The CE2 points where a 1275 keV gamma ray enters the detectors, interacts via Compton scattering with an electron such that its direction is completely reversed and then leaves the detector without further interaction. The region before CE2 is its Compton "plateau" which results from other (non-backscatter) Compton interactions where the reduced energy photon escapes the detector. CE1 is the corresponding Compton edge for the 511 keV peak.

## 2.4    Spectral Analysis

### 2.4.1 Calibrations

To obtain qualitative data, such as nuclide identity and activity measurement, from gamma-ray spectra a number of stages must first be performed such as an energy calibration and efficiency calibration. In addition, if the system has a transmission gauge (used to derive a matrix attenuation correction factor), a transmission calibration is required. These serve to provide the analysis software with information about the system's setup and overall behaviour.

The energy calibration (performed with known sources) determines the energy-to-channel relationship. The final positions of the peaks within the spectrum are defined using the amplifier gain (to determine the distance between peaks) and the ADC zero (the zero offset to set the exact peak positions). Modern energy calibration software will also calibrate the resolution (FWHM) and energy tail of the peaks.

The efficiency is required to interpret count rates for a given measurement geometry into bequerels. This is dependent on the geometry of the detector i.e. the detector-sample distance, spatial distribution, sample density and intrinsic detector efficiency. The absolute efficiency [18] is defined as:

$$\text{Absolute efficiency} = \frac{\text{Counts per sec observed in the detector}}{\text{Gammas per sec emitted by the source}}$$    **Eqn. 2**

An efficiency measurement is performed with a known multi-line source and the efficiency as a function of energy is calculated as:

$$eff(E) = \frac{A_P(E)}{t \times Act \times Abundance \times D}$$    **Eqn. 3**

where $A_p$ is the net peak area, $t$ is the live time (secs), $Act$ is the activity in Bq of the source at the calibration certificate time and $D$ is a factor to decay correct the activity to that at the acquisition start time:

$$D = e^{-\frac{\ln(2) \times t_w}{T_{1/2}}}$$    **Eqn. 4**

11

where $t_w$ is the decay time of the calibration source and $T_{1/2}$ is the half life of the calibration nuclide [19].

Since only a few energies (e.g. for $^{152}$Eu, 14 lines) are available within the calibration source interpolation is used for the curve to determine the efficiency in between these energies.

If the detector system has an active gamma-ray transmission facility then a transmission calibration will be performed, which is dependent on energy and geometry. For this a reference measurement of the count rate collected by the detector with the transmission source exposed for an empty container is required. Since only the lines of the transmission source will be found in the spectrum a transmission curve must be interpolated, as for the efficiency calibration.

During the main assay the transmission calibration is compared to the transmission measurement to determine the average density of the matrix inside the container, assuming the matrix is homogenous [8]. One problem that can occur is if the transmission beam passes through a solid lump of material, for example Pu. In this case the software would assume that the average density of the drum matrix is much higher than is the case.

## 2.4.2 Assay Analysis Software Stages

Once the calibrations have been performed and the system has been set up correctly, a transmission measurement (if required) and a passive assay are performed. At this stage generally software is invoked to perform the spectral analysis. This may consist of a large number of stages. The main stages that may be used are listed below:

- Peak analysis - the peaks are first detected above the background by the software and their energies and peak areas are determined.
- Nuclide Identification (NID) - The peaks are identified against nuclides and isotopes defined in a nuclide library based upon energies etc. A number of line energies may be checked to determine if an isotope is really within the assayed container.
- Efficiency correction - The true activity of the line is calculated based upon the efficiency curve calculated by the efficiency calibration performed previously and the equation stated in section 2.4.1 [20].

- Transmission correction (if required) - The expected matrix attenuation factor is calculated from the transmission ratios in the (active) transmission CAM files and used to calculate a corrected efficiency that would give the true activity in the segment on the assumption of uniform matrix density and uniform distribution of activity.

- Other corrections - other corrections may then be performed for self-absorption within Pu in the container for example.

- TMU and MDA analysis [21] - the Total Measurement Uncertainty (TMU) of a nuclide/isotope is quoted if the nuclide has been identified by NID. This uncertainty aims to encompass all the possible uncertainties that could have affected the measurement e.g. spatial, lump, statistical, systematic uncertainties etc. The Minimum Detectable Activity (MDA) (or a Less-Than Level) is quoted when a nuclide has not been identified by NID; it is the minimum activity that must be present to be sure an isotope is present. The value is then quoted as less than (<) this value.

## 2.5   The AQ2 - An Example of a Waste Assay System

An example of a gamma waste assay system is Canberra's AQ2 ([22], [23]), as shown in Figure 3. The AQ2 consists of a shielded chamber within which a drum is rotated (to average out heterogeneity) and assayed using three fixed Broad Energy Germanium detectors (BEGe), visible on the right hand side of the inner chamber wall. The BEGe detectors are sensitive to gamma rays in the energy range 3keV to 3MeV.



**Figure 3: Canberra's AQ2 gamma scanner used as part of the SILWAS to measure the AE4043/nn sources.**

An AQ2 has been used to perform simulated waste measurements in sections of this thesis as part of the Solid Intermediate Level Waste Assay System (SILWAS) (see Figure 4). The SILWAS was designed to measure the fissile content of solid waste drums and hence sentence them as LLW or ILW, using two components: an Auto Q2 (AQ2) and a High-Efficiency Neutron Counter (HENC) ([24], [25]) both operating with Canberra's NDA2000. The two systems work complimentarily, controlled by a 'Master control' PC with external analysis and decision making software (see

following sections) to decide which instrument offers the best result based upon effects of substances present in the waste drums (attenuation, multiplication etc), and to give activities of selected nuclides, hence sentencing the drum.
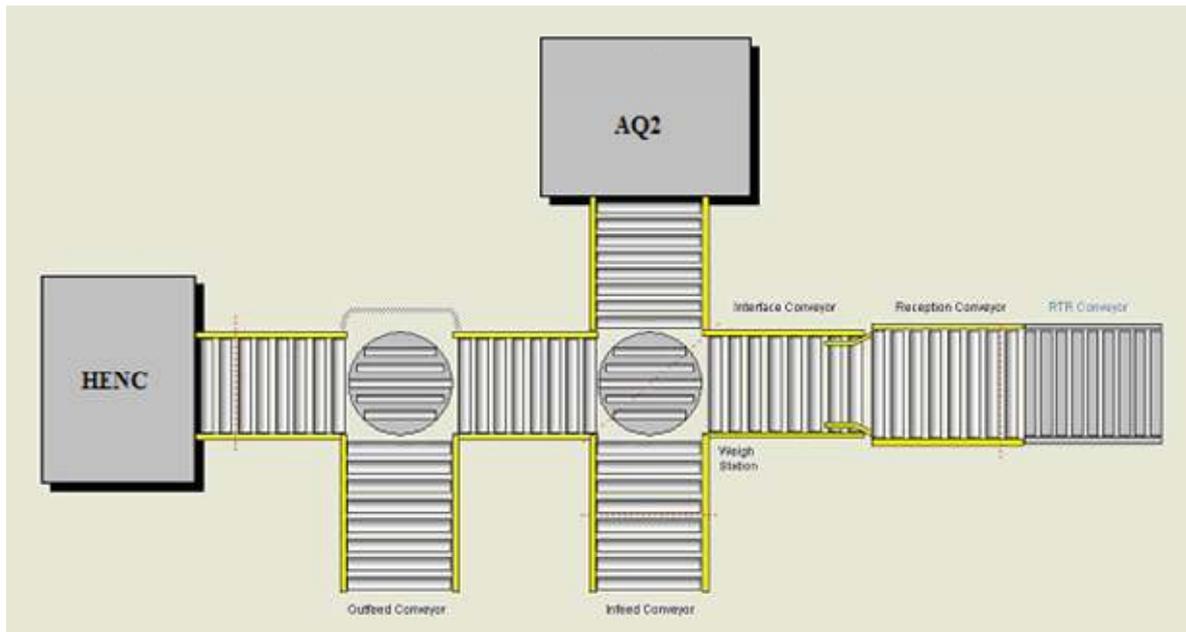


**Figure 4: A plan view of the SILWAS system showing the AQ2 and HENC chambers with connecting conveyors and turntables.**

The shield of the AQ2 is constructed from 10cm-thick low-background steel. The steel and other materials used to construct the instrument are chosen so as to minimise the naturally occurring γ emitters that could be present.

Three BEGe 2820 detectors [26] are used to minimise spatial source distribution effects and to increase sensitivity. (The individual detector results are also referred to as segment results). Three [152]Eu transmission sources (approximately 370 MBq each, emitting at 122 keV, 244 keV, 344 keV, 779 keV, 964 keV, 1112 keV and 1408 keV) are mounted in a shielded container on the outside of the chamber opposite the three detectors to determine the mean density of the matrix at

the three heights through attenuation. Mechanically-operated shutters are operated by the system to expose and shield the transmission sources inside the chamber.

Inside the shield, the drum is placed onto a rotating platform to minimise the effects of source and matrix non-uniformity. This rotation is used with the Dual Multi-Spectrum Scaling (DMSS) allowing spectra to be obtained for eight rotation sections. The use of this method known as NUDS is discussed in section 2.5.1.2.

This AQ2 has been calibrated for the 6 main drum types listed below with their SILWAS drum types and a brief description of the contents:

- IND10164 – 205 litre drum with no internal furniture other than a PVC bag and fibreboard liners
- AWG565 – a 205 litre drum with a 5 mm HDPE push-lid liner
- AWG588 – a 205 litre drum with a 7 mm HDPE screw-lid liner
- ASC047 Option 2 – a 210 litre drum with no liner and with a 100 litre drum in the centre
- ASC047 Option 3 – similar to an Option 2 but with a 1.5 mm steel inner liner
- ASC047 Option 4 – similar to an Option 2 but with a 2.5 mm steel inner liner

## 2.5.1 Analysis Stages

The analysis of results for SILWAS is performed in several different stages:

- The AQ2 performs a brief 100s assay of the drum and performs a drum type calculation based upon the transmission of the top transmission source (which does not pass through the matrix)
- The determined drum type is used as the basis for the efficiency and transmission calibrations for the main (120s active and 300s passive) measurement. NDA 2000 performs the measurements and basis spectral analysis e.g. NID, matrix attenuation correction, isotopic determination, etc.
- The drum is conveyed to the HENC to perform the neutron assay measurement using NDA2000, followed by basic neutron analysis.
- A set of Post Analysis engines are used to perform additional analyses including Pu and U lump correction, NUDS analysis, isotopics combination, TMU and MDA calculations, light

element neutron multiplication analysis, Pu combination decision making, α and β activity tables and LLW/ILW sentencing. These are described in the next section.

A custom report generator is then called to report the data in the specified user format. Selected post analysis engines are outlined in the sections below.

### 2.5.1.1 Lump corrections

The Post Analysis engines perform self-absorption corrections for Pu and U on an instrument basis i.e. summing the individual detector results before performing the correction. The methods for these corrections are described in detail in sections 3 and 4. However, since the SILWAS was installed whilst the SAC methodology was in its early stages of development, the first generation (6$^{th}$ order log polynomial) method has been used for the curve fits (see section 3.8.2). The selected isotopics are used to convert the total Pu mass results for each of the Pu isotopes.

If the U self-absorption correction cannot be performed due to one of the lines not being identified for example, a U lump component is incorporated into the TMU.

### 2.5.1.2 Non-Uniformity Detection Software (NUDS)

The non-uniformity detection software (NUDS) has been designed by Canberra to identify any non-uniform matrix density and source distribution [27]. A Dual Multi-Spectrum Scaling (DMSS) is used to obtain eight separate spectra for the eight rotation sections while the drum rotates during the measurement.

The passive counts for each octant for the 186 keV line for $^{235}$U, 1001 keV line for $^{238}$U and 414 keV line for $^{239}$Pu, plus the nearest transmission line for each octant for each for these lines are stored. The program then calculates the longitudinal and vertical, matrix and source NUDS values and errors for each of the three isotopes. The results are presented graphically in the report (see Figure 56 as an example).

The source longitudinal value for the $^{235}$U record is also used and compared to a 'lump threshold' set by the user to determine if the sample may be considered to be uniform or not i.e. if the value is greater than the lump threshold set by the user the sample is said to be non-uniform and the user specified minimum number of lumps is used as the number of U spheres (when the U self-absorption correction has not been performed - see section 2.5.1.1).

### 2.5.1.3    MDAs and TMUs

The MDA engine reads NDA 2000 calculated MDA values for those nuclides that are not detected for each segment and applies a correction for matrix attenuation and for spatial variations (see section 5.5 and 5.2). If $^{239}$Pu is an MDA then the other Pu isotope records are found and have their MDAs scaled according to the current isotopics. A similar method is performed if both $^{235}$U and $^{238}$U are MDAs. This is performed before the attenuation and spatial MDA corrections so that all MDAs on the report are corrected accordingly.

The TMUs (see section 5) are made up from the following sources:

- NDA 2000 NID uncertainties which include counting statistics in the assay data, detection efficiency calibrations, transmission calibrations, nuclear data in the nuclide library etc
- Source spatial variations
- Lump TMU contribution for $^{235}$U

The gamma-ray used to determine the $^{235}$U result is 186 keV which is highly attenuated in uranium metal. In view of the likelihood that the uranium may be present in the waste in the form of metal pieces, a 'worst-case' contribution to the positive TMU for $^{235}$U is calculated. This is based on the assumptions that the U will be present in a number of equi-sized spheres with density 18.7 g/ml and that the number of spheres will be either a minimum or maximum (user set) number of lumps according to whether the longitudinal non-uniformity parameter for passive $^{235}$U calculated in the NUDS engine exceeds the *LumpThreshold* value.

If USAC has not been performed then a $^{235}$U lump uncertainty is additionally combined. This lump uncertainty is calculated and combined with the other sources of error on a segment basis.

#### 2.5.1.4  Light Element Multiplication

The Light Element Multiplication engine looks for $^{22}$Na (indicating fluorine in intimate contact with α-emitting material) and $^{9}$Be in the spectrum and compares the activities/count rates to threshold values set by the user to determine if any light element multiplication has taken place, e.g. in the interaction:

$$^{19}F + {}^{4}\alpha \rightarrow {}^{22}Na + {}^{1}n$$
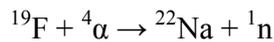
If the activity is greater than the limit set by the user then the a flag is set, otherwise it is assumed that there is no $^{19}$F(α,n) reaction taking place.

#### 2.5.1.5  Source of Result Decisions and ILW/LLW Sentencing

A complex decision tree has been devised to determine which instrument offers the best source of Pu result based upon the calculated mass and uncertainty or MDA, plus other factors such as evidence of light element multiplication and the HENC reals to totals ratio. This process will not be described in detail in this report but more information may be found in Canberra documentation [28]. The chosen source of result is combined with the other data and user-specified limits to determine:

- If the combined Pu and $^{235}$U mass is below the allowed fissile mass limit (~120g)

- If the total alpha activity $\dfrac{Total\alpha + k\sigma_{\alpha}}{grossweight}$ is less than the UK LLW alpha limit of 4 kBq/g

- If the total beta activity $\dfrac{Total\beta + k\sigma_{\alpha}}{grossweight}$ is less than the UK LLW beta limit is 12 kBq/g.

where k is a user-specified confidence factor.

### 2.5.2 Calibration

### 2.5.2.1 AQ2 Energy and Transmission Calibrations

The energy and FWHM calibration of the γ-ray spectrum has been performed using the normal Genie 2000 method, as described in the Genie 2000 Operations Manual [29]. The spectrum gain may be set by collecting a spectrum from a multi-line gamma source in front of the detector using Genie 2000 'Gamma Acquisition and Analysis' (GAA). For this purpose the $^{152}$Eu transmission source is used by exposing the source using the transmission shutters. The coarse and fine gains are adjusted until the 1408 keV $^{152}$Eu line is placed at channel 15000 to give as much spread between peaks without going off the channel limit. The conversion of channel number to energy i.e. the calibration of the spectra can be performed by selecting *Calibrate| Energy Full| By Certificate File* and choosing the appropriate certificate file for the source.

The system also requires transmission calibrations for each container and geometry type. Transmission Calibrations are performed in the standard manner, as described in the NDA 2000 User's Manual [30]. The process involves placing an empty drum in the AQ2 and performing a Transmission Count on the AQ2 PC specifying the drum type in the information set-up screen. The NDA 2000 Calibrations program is then opened and the relevant counter type, calibration type, geometry and container type are selected. The method is followed as described in the NDA 2000 User's Manual [30].

### 2.5.2.2 AQ2 Efficiency Calibration

The SILWAS was intended to assay two different sizes of drums, 205 litre and 210 litre, each of which have 3 variations of internal furniture, giving a total of 6 main physical drum types (as described in section 2.5). Efficiency calibrations are required - two for each container type to account for the cases with and without the sliding filters (1.5mm thick sheets of tin to reduce the countrate for very active drums). Thus 12 efficiency calibrations are required in total.

The effects of γ-ray absorption in the internal furniture and the walls of the drums are incorporated in the efficiency calibration for each drum type. The effect of γ-ray absorption in the waste material inside the drum (matrix), which can vary from drum to drum, is handled by using the

gamma transmission measurement (see section 5.5). The matrix analysis makes the assumption that the matrix attenuation is uniform at least throughout each detector segment.

In practise it proves difficult to measure the VWA efficiency because of the difficulties in accurately simulating a VWA γ-ray source throughout the internal volume of the drum. Consequently the efficiencies have been derived by numerical integration of contributions to the detector count rate from individual voxels with a computer model (NDA Model [31]).

Spectra have been acquired for a calibrated multi-line near-point disc source on the rotation axis of the turntable at the same height and known distances from the detectors, to provide absolute peak efficiency data for the model. The source was placed inside a drum to support the source only. The attenuation in the drum wall is factored out in the subsequent calculations and replaced with the calculated drum wall attenuation for the container being modelled.

A Certificate File is created for the multi-line source, containing the number of gamma-rays emitted per second by the source for each line calculated at a single date and time (obtained from the source's calibration certificate). Using this Certificate file and the measured spectrum file an efficiency calibration is generated using GAA. The NDA model can then use the point-source efficiency data in this file to calculate the probability that photons that strike the detectors will produce a peak event.

The NDA Model produces VWA efficiencies for a range of energies selected to span the spectral range of interest i.e. 60 keV to 1500 keV. These efficiency triplets (energy, efficiency and uncertainty) are then entered into an NDA 2000 Calibration which is a set of files maintained by NDA2000.

Five of the six container-type efficiencies could not be created by direct measurement because gamma sources were not available to reproduce accurately a uniformly distributed activity. For this case, rod sources were used that are the correct length for 205 litre drums with no internal furniture. The VWA efficiency for the IND10164 container has therefore been separately

measured purely as a supporting check on the validity of the method used for the computed efficiencies.

The rod sources are a set of 7 calibrated multi-line sources that are placed within the drum in a jig to simulate a uniform spatial distribution of activity for the rotating drum. These sources are 830mm long (with a 2mm end cap at each end giving an active length of 826mm) thin aluminium tubes filled with epoxy that has been doped with known amounts of selected gamma-ray emitting isotopes. Table 1 lists the isotopes and their activities.

**Table 1: Activities of isotopes in CUK Rod Sources used for the AQ2 Efficiency Calibration.**

| Line | Source | 10035 | 10036 | 10037 | 10038 | 10039 | 10041 | 10042 | Total |
|------|--------|-------|-------|-------|-------|-------|-------|-------|-------|
| Isotope | Half-life (years) | kBq | kBq | kBq | kBq | kBq | kBq | kBq | kBq |
| Am-241 | 432.7 | 830.8 | 798 | 849.4 | 826.2 | 827.4 | 827.9 | 820.6 | 5780.3 |
| Ba-133 | 10.54 | 450.7 | 432.9 | 460.8 | 448.2 | 448.9 | 449.2 | 445.2 | 3135.9 |
| Eu-152 | 13.33 | 458.5 | 440.5 | 468.8 | 456.1 | 456.7 | 457 | 452.9 | 3190.5 |
| Cs-137 | 30.17 | 92.07 | 88.44 | 94.13 | 91.57 | 91.69 | 91.75 | 90.94 | 640.59 |
| | | Strengths quoted are 1200hrs PDT July1 2001 in kBq | | | | | | | |

Figure 5 shows a plot of the VWA efficiency computed for the IND10164 Container type for each of the 3 detectors and the directly measured efficiencies obtained using the rod sources. The Detector 2 curves lie on top of each other fairly well and consistently with the error bars. These errors are dominated by the contribution from the absolute uncertainty on the activities of the sources in the certificate files.

Detectors 1 and 3 show small systematic differences between the measured and computed which can be attributed to difficulties in reproducing a truly VWA source distribution with rod sources. The problem is more apparent at the ends of the sources where the real drum and line source dimensions do not exactly match the model ideals.

The comparison provides confidence that the computed efficiencies are consistent with real measurements and justifies the use of computed values, which are found to be universally more reliable and consistent than measured ones.
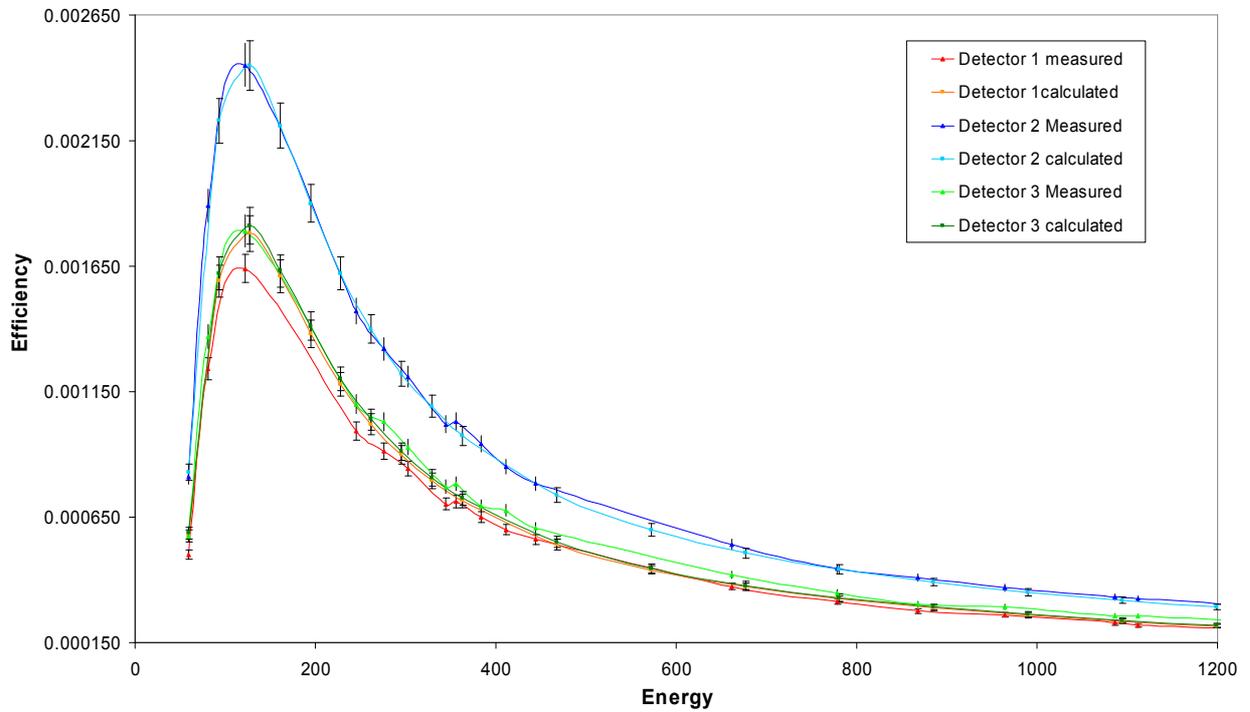
**Figure 5: Plot comparing computed VWA peak efficiencies for the IND10164 drum type with a measurement of the same drum type using 7 calibrated rod sources.**

### 2.5.2.3   HENC Calibration

The calibration of the HENC includes an add-a-source calibration, neutron multiplicity characterisation and Pu mass calibration. These calibration methods will not be detailed in this thesis, however more information may be found in Canberra documentation ([32], [33]).

# 3 PLUTONIUM SELF ABSORPTION

## 3.1   Introduction

During previous work an issue with the current plutonium self-absorption correction was highlighted; for an AE 4043/5 Pu sample [31], a consistent over-correction of 50% was observed when measuring with an SGS (Segmented Gamma Scanner). The possibility of inaccurate measured line intensities as the source of the problem was ruled-out by comparing uncorrected 129keV and 414keV assay results with calculated SAC (self absorption corrected) emission rates for this sample. This prompted detailed analysis of the Pu self-absorption behaviour for various lump shapes and materials (densities) and hence the search for a more accurate SAC method. One resolution to this problem is to calculate self-absorption factors using analytical methods [35]. Due to the extreme non-linearity in the nature of gamma attenuation these methods generally require some degree of approximation.

The bias caused by self-absorption in lumps is long known [36], though advances failed to develop until the early 1980s when computer processing became more widely available. In 1981, work concentrating on the analysis of HTGR fuel resulted in a correction algorithm assuming single-sized lumps in heterogeneous materials [37]. This assumption was also used for LANL SGS and TGS correction techniques, using a least squares weighting algorithm ([38], [39]). This work has been extended for a mixture of lumps, separated into two main portions which are treated separately [40]. Recent work by Croft et al. [41] has developed and examined calculation tools for analysing the self-absorption within specific shapes in the far-field approximation.

This chapter initially examines the problem of self-absorption within lumps of Pu using current SAC techniques, concentrating on the Fleissner method [42] as a standard correction technique (available as a module in Canberra's NDA2000 suite). Data were modelled for Pu lumps of various sizes and shapes in the near-field, using a numerical approach, reducing any assumptions about the sample and its distribution. A new SAC algorithm is then proposed and tested using modelled data for three different lump types.

The new technique is then tested using measured data from encapsulated AE4043/nn PuO$_2$ samples, following an investigation into the sources themselves and an estimation of their average density based upon observations from measurements.

The results from both the measured and modelled data are examined. There is also a brief study to investigate the use of the new SAC algorithm with multiple lumps present.

### 3.1.1 Why is Pu a Problem?

The measurement of Pu poses a problem in each of the three measurement techniques described in Section 1.3. Both calorimetry and PNCC measurements require the isotopic composition of the sample to be known. This is not always the case for waste and so a further measurement, using a HPGe detector, for example, is generally required. Also for the PNCC, multiplication may occur if light elements are in close contact with the Pu. Pu in compact form is self multiplying and if the ($\alpha$,n) yield is also high (e.g. $^{241}$Am-rich and if low-Z materials are present) the induced fission component can be significant. Similarly if the Pu is in intimate contact with materials that can also be fissioned or multiply fast neutrons (n,2n). In parallel, $\gamma$-ray assay suffers from attenuation within the Pu itself.

Although $^{239}$Pu emits many lines, for $\gamma$-ray assay Pu is generally measured using $^{239}$Pu lines at around 400 keV e.g. 375 keV and 414 keV since these are least affected by matrix attenuation and lump effects. These lines exhibit the best detector properties of good penetration in waste and lumps and show a reasonably high intensity. The assay of plutonium in waste is complicated by the physical form in which it may occur, such as particles or even large lumps which may exhibit a high degree of self-attenuation effects due to the mass attenuation coefficients at the assay energy.
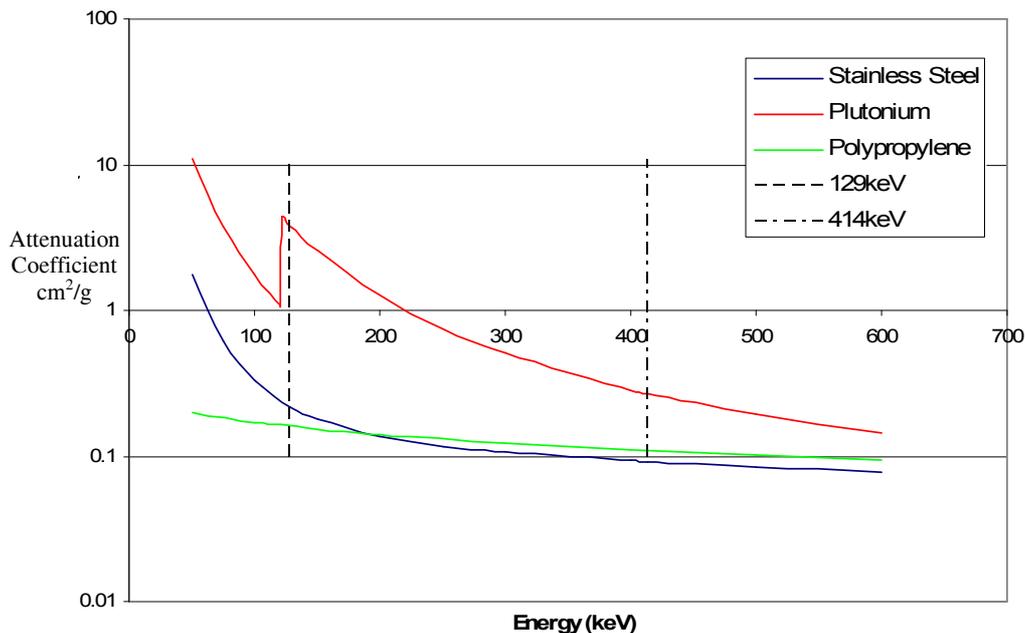
**Figure 6: μ vs Energy for various materials generated from Genie ISOCS attenuation coefficient data (mu04_8lb.txt file).**

Figure 6 shows the mass attenuation coefficient (μ) versus energy (E) for three different materials: stainless steel, polypropylene and plutonium, and the location of the 414 keV line is indicated. Also shown is the location of the strong 129 keV line from [239]Pu. The ratio of the mass attenuation coefficients for the two energies (129 keV and 414 keV) for polypropylene and stainless steel is much less than that for Pu. Also the 129 keV energy line lies just above the K-edge of the Pu curve (121.8 keV), hence Pu suffers much more strongly from attenuation effects at these energies. Consequently the 129 keV and 414 keV pair offers a better differential absorption in this set of more prominent γ-ray spectra lines. Those properties of the 129 keV and 414 keV lines form the basis of methods for correction for self-absorption in Pu.

### 3.1.2 The Fleissner Method

A standard SAC algorithm offered in Canberra's NDA2000 data acquisition and analysis suite [43] was developed empirically by John Fleissner [42] for the assay of canned radioactive waste containing a distribution of lump sizes: The approach involved comparing gamma-assay results

against calorimetric-based assays of the same item and fitting mass as a function of energy. The form of the correction using just two lines is shown below:

$$M_i = M^o e^{-\frac{\beta}{E_i}}$$
Eqn. 5

where $M_i$ and $E_i$ are the apparent intensity and energy of the i'th line respectively, $M^o$ is the corrected activity of the nuclide and $\beta$ is a model parameter. This correction can be derived from first principles under the assumptions that the self-absorption is not severe and therefore the method may be less appropriate for single lumps and encapsulated sources. This basic model assumes that all of the nuclide experiences self-absorption. If some of the material does not experience self-absorption then multiple energy lines may be used in the equation below:

$$M_i = M^o \left( 1 + \alpha \left( e^{-\frac{\beta}{E_i}} - 1 \right) \right)$$
**Eqn. 6**

where $\alpha$ is the ratio of the self-absorbed activity to the corrected activity and is constrained to be ≤1. The equation may also be expressed as:

$$M_i = \left\{ M^0 (1 - \alpha) \right\} + \left\{ M^0 \alpha e^{-\frac{\beta}{E_i}} \right\}$$
**Eqn. 7**

where the first component of the apparent mass that is due to zero self-absorbing material (i.e. the matrix), and the second component is the fraction of apparent mass that is due to the self-absorbing material itself. Therefore if $\alpha$ is zero then the apparent masses have suffered no self-absorption; and if α is unity then the apparent masses are due to self-absorption within the lump only, and the equation simplifies to the two-line method (see above).

The Fleissner SAC methods are made available with NDA2000 with the onus being on the user to validate its suitability for the particular waste form; the Molten Salt Extract residue for which the approach was initially developed may not be a good match for another person's needs.

The basic two-line and the three-line methods have been analysed using a point source model which is described in Section 3.2. Another possible route for study that has not been considered in this PhD is to investigate the extension of the Fleissner equations to cases of $E_n$.

### 3.1.3 The Infinite Energy Extrapolation Method

The infinite energy extrapolation method [44] determines an estimate of the self-absorption corrected mass based upon a curve of the apparent mass ($m_i$) versus the reciprocal of the energy ($1/E_i$), for example, for a series of lines (i) from the same isotope. For example, for a 28g $PuO_2$ (24.7g Pu) stainless steel encapsulated source (see section 3.3) in an empty 200 litre drum, measured for 300s using an AQ2 as described in section 2.5, the measured $^{239}Pu$ lines are 129 keV, 203 keV, 345 keV, 375 keV, 392 keV, 414 keV and 451 keV. A graph of the apparent mass versus 1/E is shown in Figure 7.
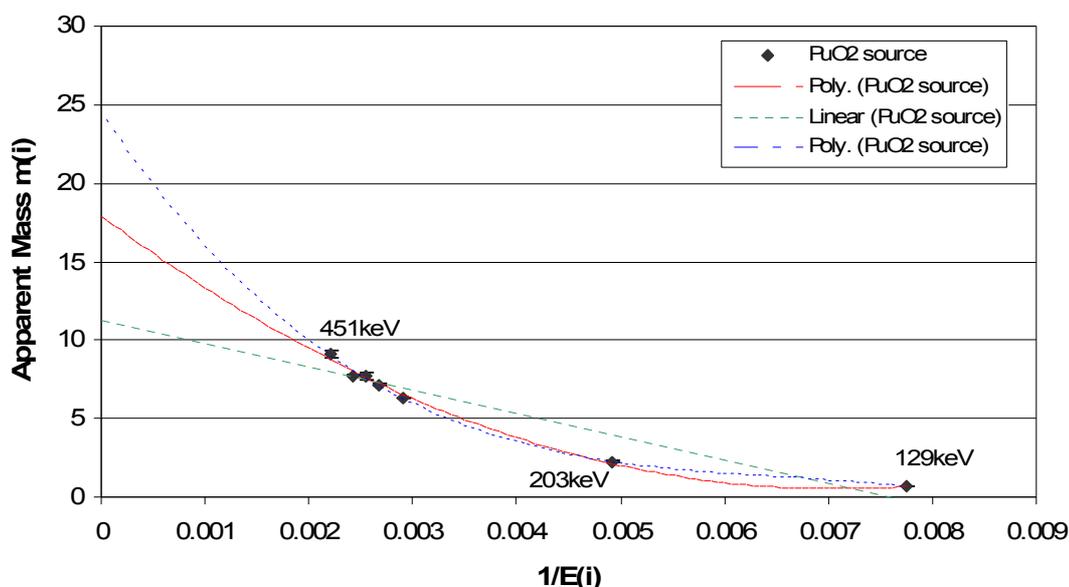


**Figure 7: Graph showing the apparent $^{239}Pu$ mass $m_i$ (g) and uncertainties against $1/E_i$ for AE4043/10 in an empty 200 litre drum showing a linear, 2$^{nd}$ (green) and 3$^{rd}$ (blue) order polynomial curve fits.**

The extrapolation intercept of the curve will give an estimate of the $^{239}Pu$ mass of the sample. The graph shows three types of curve fits to the data: linear, 2$^{nd}$ and 3$^{rd}$ order polynomial fits. The 3$^{rd}$ order polynomial fits this set of data the best with an $R^2$ of 0.997 ($R^2$=0.994 for 2$^{nd}$ order polynomial and 0.908 for the linear fit). This fit estimates a Pu result of approximately 32.3 g, an

overestimation compared to the true Pu mass of 24.7 g. The 2<sup>nd</sup> order polynomial fit gives a good estimation of 23.6g, whereas the linear fit underestimates the mass as 14.7 g.

Another possibility is to plot the natural logarithm of the apparent mass versus 1/E. This method is linked to the 2-line Fleissner method since the Fleissner equation (see section 3.1.2) may be rearranged into the form:

$$\ln(M_i) = -\frac{\beta}{E_i} + \ln(M^o) \qquad \textbf{Eqn. 8}$$

where the y-axis may be given by $ln(M_i)$ and the x-axis as $1/E_i$, with the y-intercept as $ln(M^o)$ and negative gradient of the graph as $\beta$.

These methods are compared to the three line Fleissner techniques and the new Pu SAC method in section 3.12.

## 3.2 Description of the Point Source Model

To perform the calculations for the analysis of the basic Fleissner method and other self-absorption modelling a point source model developed by M. Wormald [31] has been used. It is based upon the physical principles, requires only the photopeak energies (since it is based upon a germanium detector set-up) and assumes only knowledge of nuclear data.

The model allows a lump size, shape (cylinder or cuboidal shapes) and composition to be specified by the user. The model breaks the lump up into a specified number of voxels (volume elements - see section 3.6), defined by radial, polar and height integration intervals for cylindrical lumps, and lateral, depth, height and rotation integration intervals for cuboidal lumps.

The model sets the gamma-ray production in each voxel as the volume of the voxel and computes the probability of the gamma-rays reaching the detector without scattering or absorption. The voxel contributions are integrated over the whole lump and the calculation repeated with the density in the attenuation function set to zero, the ratio of these results defines the self-attenuation factor (SAF) for that gamma-ray line energy (i), i.e.

$$SAF_i = \frac{R_{0i}}{R_{si}}$$   **Eqn. 9**

where $R_{si}$ is the detected count rate from the sample and $R_{0i}$ is the detection rate there would be with no self absorption in the sample for the energy i. The apparent masses may then be calculated using:

$$M_i = SAF_i.M_T$$   **Eqn. 10**

where $M_i$ is the apparent mass at the line energy i, $SAF_i$ is the self attenuation factor at energy i, and $M_T$ is the true mass of the modelled sample.

The incoherently scattered component of the gamma-ray flux reaching the detector can safely be ignored where high resolution Ge detectors are to be used in the measurement since the scattered photons are almost invariably energy-degraded to the continuum below the photo-peak. The coherent scattered component (which does not involve energy loss) may be neglected since it is assumed that the flux in and out of the geometry will cancel.

## 3.3   AE4043/nn Sources

In order to better validate the point source model the modelled sources should be compared to experimentally-measured sources. Since bare sources are not available for safety purposes the model was tested with stainless steel encapsulated sources. In order to correctly model the sources themselves they must first be examined and their structure understood in detail. In this section we compare the fabrication details of the sources with empirical validation measurements to reveal some subtle differences. These differences are important when using the sources to test any Pu SAC algorithm.

**Table 2: Isotopics for AE4043/nn sources, measured 27 January 1990  [45] and calculated 20 January 2007.**

|  | Measured 27/01/90 | | Calculated 20/01/07 | |
|---|---|---|---|---|
| Isotope | Weight % | Uncertainty % | Weight % | Uncertainty % |
| Pu-238 | 0.121 | 0.001 | 0.107 | 0.001 |
| Pu-239 | 76.792 | 0.022 | 76.702 | 0.022 |
| Pu-240 | 21.336 | 0.019 | 21.564 | 0.019 |
| Pu-241 | 2.052 | 0.002 | 0.917 | 0.010 |
| Pu-242 | 0.701 | 0.002 | 0.710 | 0.002 |
| Am-241 (with respect to Pu) | 817 ppm | 2 ppm | 12228 ppm | 103 ppm |

The sources which have been used to test the Pu SAC algorithm experimentally are the AE4043/nn sources. These are stainless steel (double) encapsulated $PuO_2$ sources containing the relative isotopic composition in Table 2. Although the outer structure of the sources is documented thoroughly ( [45], [46]), the internal composition ($PuO_2$ density, fill height, symmetry etc.) is not well known.

The sources consist of a series of 1.3mm thick stainless steel capsules, shown separately in Figure 8 and Figure 9. Figure 8 shows the components of the stainless steel encapsulated sources, including the tools for extracting the inner piston and compressing the $PuO_2$.
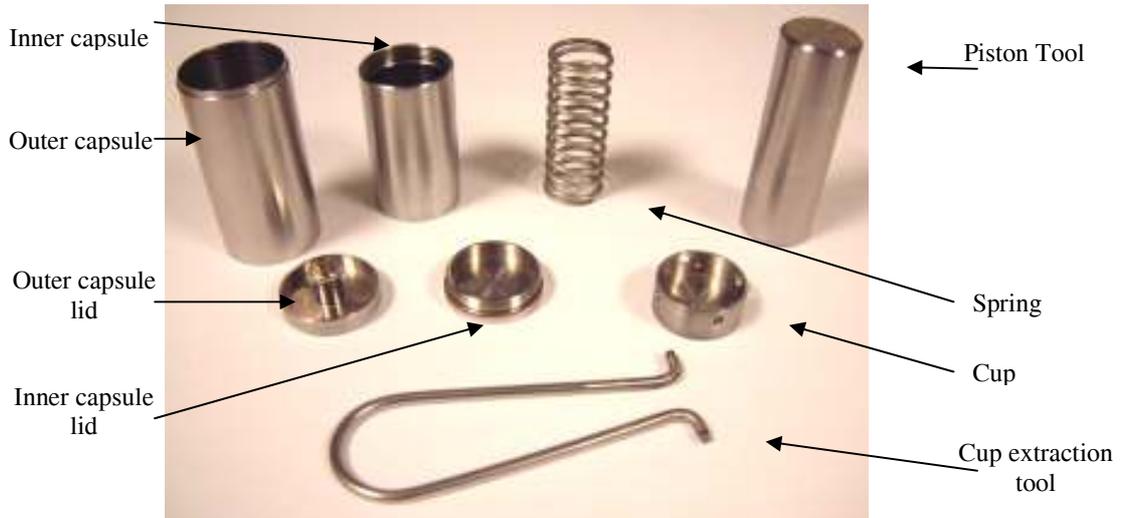
**Figure 8: The AE4043/nn source components including the inner and outer capsule and lids, cup, spring, piston tool and cup extraction tool (excluding the spring locators).**



**Figure 9: The AE4043/nn source component configuration minus the spring locators.**

The source components are configured as shown in the photograph in Figure 9 and the internal sketch in Figure 10. The $PuO_2$ is compressed into the base of the inner capsule using the piston tool and the cup. This is then held in place firmly by the spring and locators, which is secured between the cup and the inner capsule lid. The inner capsule is then fitted into the outer capsule and sealed. The spring was not fitted for sources containing greater than 28 g of $PuO_2$ (items AE4043/9 and /10).
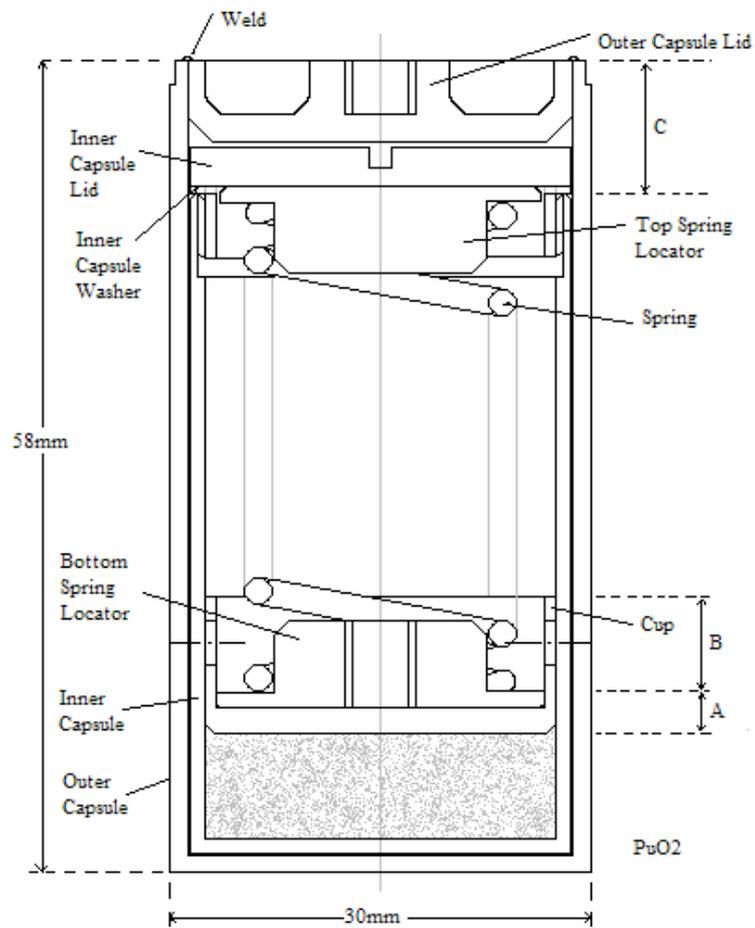
**Figure 10: The AE4043/nn source internal capsule components and basic dimensions, re-sketched from Crossley et al, 1991 [45].**

**Table 3: AE4043/nn source Pu and PuO$_2$ content and calculated fill heights assuming a density of 1.856 g.cm$^{-3}$.**

| Source ID | PuO$_2$ mass (g) | Pu mass (g) | Fill height (mm) |
|-----------|------------------|-------------|------------------|
| AE4043/1  | 0.113 | 0.099 | 0.12 |
| AE4043/2  | 0.565 | 0.494 | 0.62 |
| AE4043/3  | 1.128 | 0.986 | 1.24 |
| AE4043/4  | 2.261 | 1.977 | 2.48 |
| AE4043/5  | 5.650 | 4.941 | 6.20 |
| AE4043/6  | 8.479 | 7.414 | 9.31 |
| AE4043/7  | 11.298 | 9.879 | 12.40 |
| AE4043/8  | 22.597 | 19.758 | 24.80 |
| AE4043/9  | 28.246 | 24.697 | 31.00 |
| AE4043/10 | 28.252 | 24.702 | 31.01 |

The source sizes used in this work range from 0.099 g to 24.70 g of Pu (0.11 g to 28.25 g of $PuO_2$) as shown in Table 3. This table also contains an estimate of the $PuO_2$ fill height within the inner capsule based upon a density of 1.856 $g.cm^{-3}$; however the true density of the powder is not specified. From the original sketch and micrometer measurements (Figure 10) the internal diameter of the inner capsule is accurately 25 mm, the inner capsule is 1.11 mm thick, the outer capsule is 1.14 mm thick and the gap between the two capsules is 0.25 mm.

### 3.3.1 AE4043/nn Preliminary Source Measurements

Two identical sets of measurements have been performed using a single 70 mm diameter by 20 mm thick BEGe3820 detector, to observe the behaviour of the SAC algorithm for the AE4043/nn sources whilst not within drums or waste matrices. The apparatus was constructed on a horizontal bench, as shown in Figure 11, so that the active source material was approximately level with the centre of the detector, with the relevant edge of the source casing at 40cm and 43cm from the detector. The AE4043/nn sources were measured in two different orientations: upright (as shown with the active material at the base) and horizontally (on their side with the active material nearest to the detector). The sources were separated from the detector with a 1.5 mm thick Cd attenuator sheet to reduce the high count rate from the lower energy gamma rays especially the intense 60 keV radiation from [241]Am which grows in from the decay of [241]Pu.
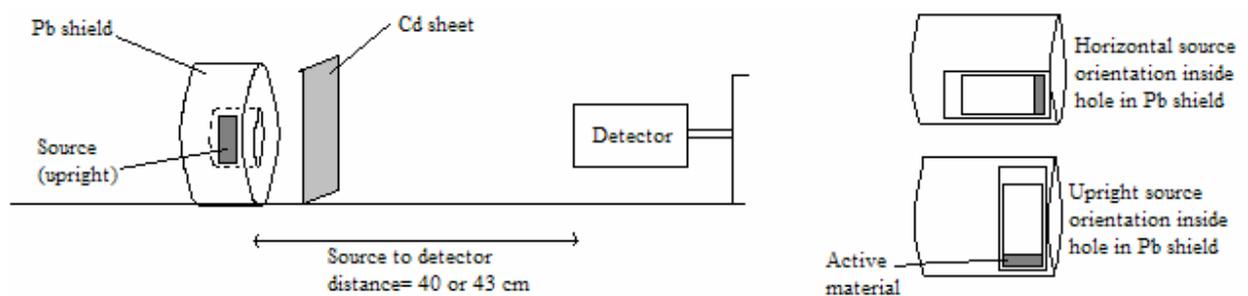


**Figure 11: AE4043/nn sources preliminary test measurements with source in the upright position.**

Energy and efficiency calibrations were performed with a multi-line ([241]Am, [133]Ba, ^{137}Cs, [152]Eu) source and a reference pulser was used to perform the deadtime correction. The 129 keV and 414 keV apparent mass results are plotted in Figure 12 and Figure 13 respectively for both measurement sets and source orientations, including measurement errors.
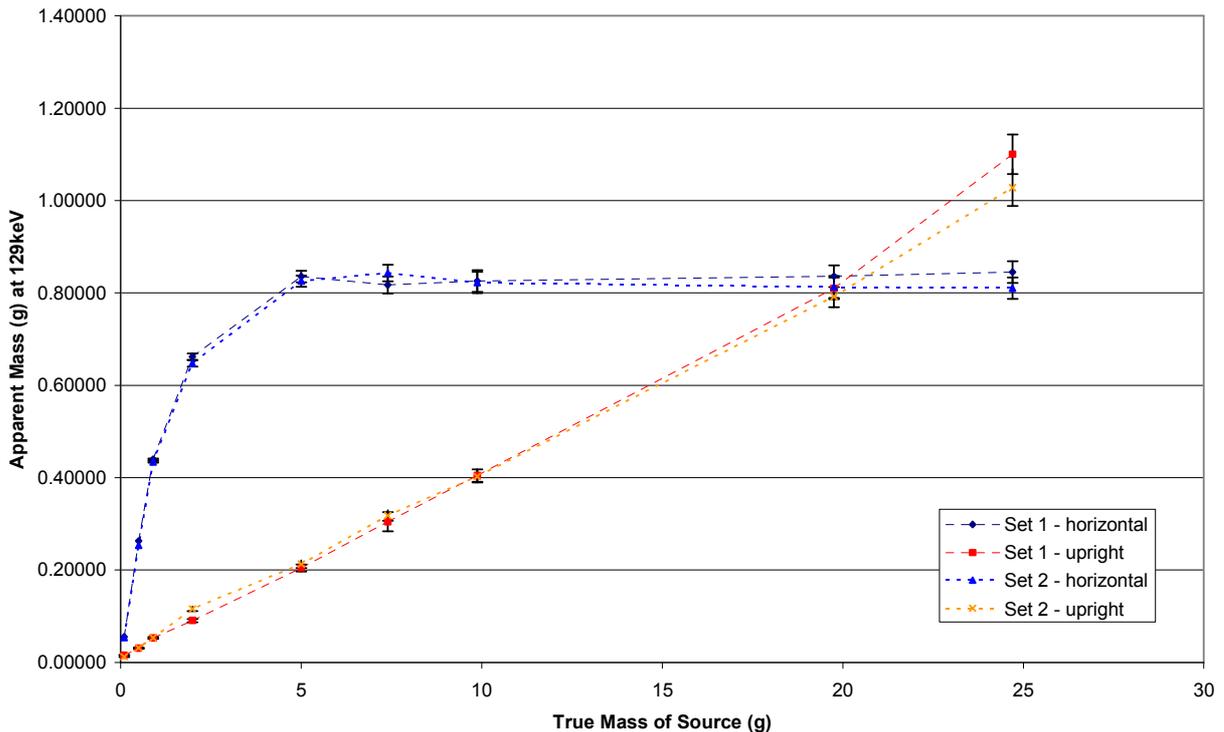


**Figure 12: Graph showing the measured apparent masses for two sets of measurements at 129keV for the AE4043/nn sources for both horizontal and upright source orientations.**

For the sources orientated in the upright position, with the axis of the source material normal to the detector axis, the thickness of $PuO_2$ seen by the detector remains constant as the mass (and fill height) increases. Consequently the apparent masses of the 129 keV and 414 keV lines increase linearly (allowing for statistical fluctuations) in direct proportion to the fill height assuming that the bulk density is constant for all sources (see section 3.3.2). For the sources lying horizontally with the circular base at right angles to the detector axis, the apparent mass of $PuO_2$ increases with source mass until the gamma-rays can no longer penetrate the $PuO_2$ on route to the detector. For

the 129 keV lines this occurs at a source mass of approximately 5g (apparent mass 0.83 ±0.16 g). Figure 13 demonstrates that the 414 keV gamma rays do also suffer from the effect but much less strongly.
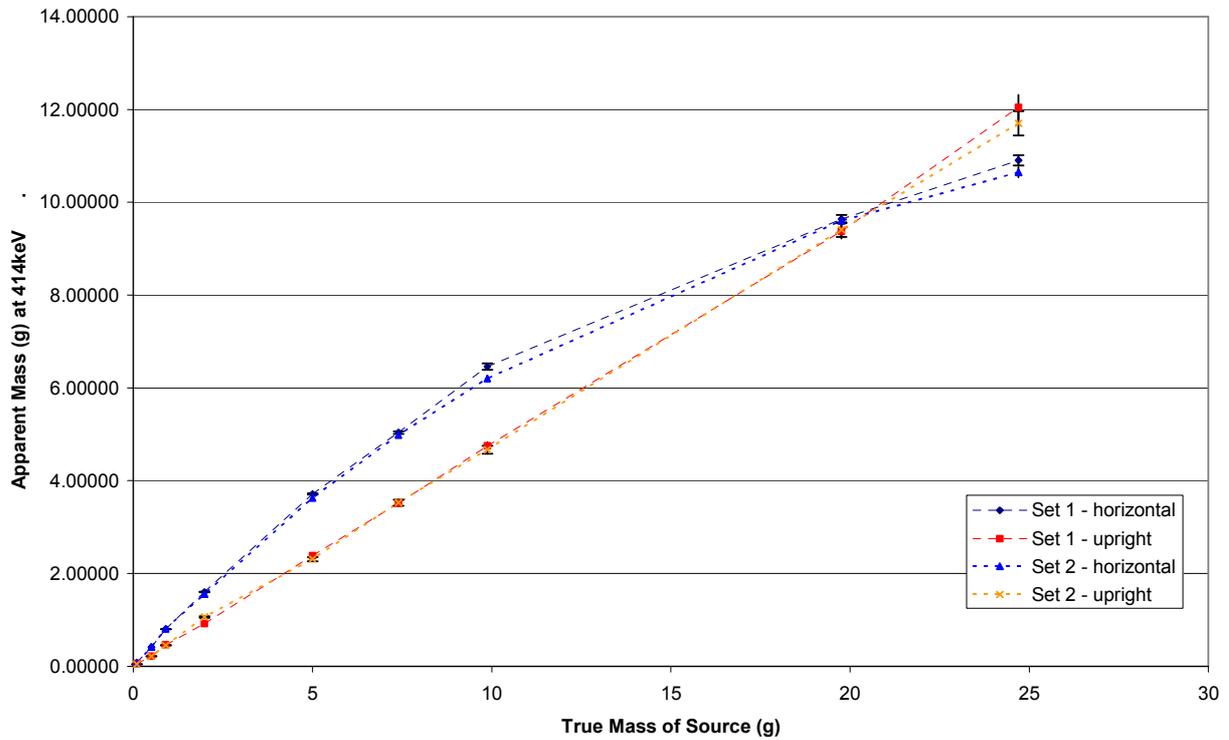


**Figure 13: Graph showing the measured apparent masses for two sets of measurements at 414keV for the AE4043/nn sources for both horizontal and upright source orientations.**

### 3.3.2  AE4043/nn PuO$_2$ Density Determination

In order to be able to model the sources correctly, the density of the PuO$_2$ inside the inner capsule of the AE4043/nn sources must be known. Despite the detailed mechanical descriptions of the sources, the fill heights and densities of the source PuO$_2$ powder have not been stated.

Previous studies at Canberra by Croft et al [46] have assumed a density of 1.51 g/cm$^3$ for all sources, estimated assuming that the PuO$_2$ powder in AE4043/9 and /10 fills the inner capsules since their springs are not present. These studies were later revisited [47] and densities between

1.72 g/cm$^3$ and 2.03 g/cm$^3$ were adopted for the sources based upon assumptions about the length of the spring which holds the cap in place.

In order to better estimate and independently confirm the density of the AE4043/nn sources the fill-height of a selection of sources must be determined from experimental data [48]. An experiment has been set up for this purpose, as shown in Figure 14.
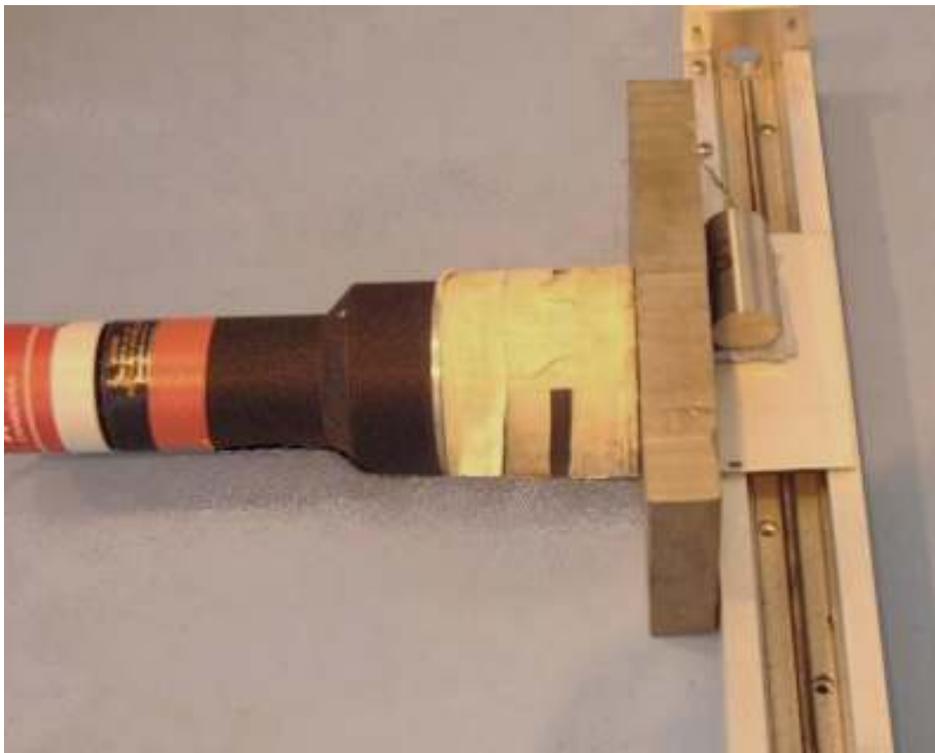


**Figure 14: Photograph of the machine slide experiment used for powder distribution and fill-height measurements of the AE4043/nn sources.**

The equipment consists of a 7cm diameter NaI detector connected to a Canberra UniSpec MCA, set perpendicular to a machine slide, and separated from the source by a 30 mm deep tungsten collimator with a 1 mm hole. The instruments are secured to the table so that the source detector and machine slide cannot move independently (not shown in the figure). The initial source position is beyond the view of the detector through the collimator and is moved in 0.25-0.5 mm

intervals using the manually-operated machine slide so that the side of the source passes along the sight of the collimator, until the measured countrate returns to its original value and remains at this level for several measurements.

The deadtime-corrected counts in the 60 keV peak region of interest (ROI) (from [241]Am) are recorded for regular periods (the duration depends on source strength) using Genie[TM] 2000 Gamma Acquisition and Analysis [49]. The 60 keV peak has been chosen since it has a high intensity and is at a relatively low energy and so will not be affected by the collimator as much as any higher-energy peaks.

For the purpose of this experiment it is assumed that at the very edge of the active material the collimated detector will observe half of what it would observe for an infinite material because the edge of the source is exactly half way across the collimator gap. Consequently the FWHM of the spatial count rate profile should give an estimate of the thickness (height) of active material in the source. In order for this assumption to apply the spatial profile must also reach a definite peak region so the FWHM may be correctly calculated. Therefore the source must be of sufficient height so that a flat region is observed where the countrate is unaffected by the edges of the active material. Calculations show that the field of view of the source from the detector is approximately 1.4mm and so the measured source must have a fill height greater than this value. Consequently, this process has been performed for 6 sources: AE4043/5, 6, 7, 8, 9 and 10 (approximately 5g, 7.5g, 10g , 20g, 25g and 25g respectively) (see Table 5). An example of the spatial profile for AE4043/6 is shown in Figure 15.
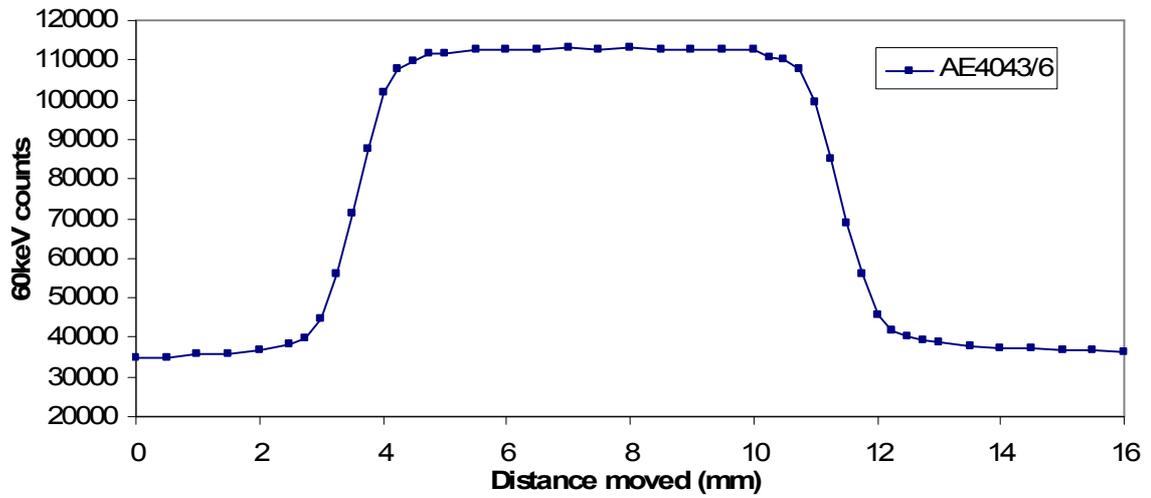
**Figure 15: Spatial profile for 60 keV activity distribution in the 7.5 g AE4043/6 source.**

To calculate the density of the $PuO_2$ in the source the FWHM of the distribution must first be found. For this example (Figure 15) the background countrate is averaged at 35500 counts, and the peak counts are averaged at 112800 counts. Therefore the Half Maximum value is 74150 counts (after accounting for the background) and it can then be determined between which two pairs of source locations the FWHM should be calculated. It is assumed that the graph is linear between the pair of the points and so by plotting the straight line and using the Half Maximum value as the co-ordinate the FWHM may be determined. Table 4 and Figure 16 show the results for four of the six sources. The remaining two sources have been omitted as explained below.
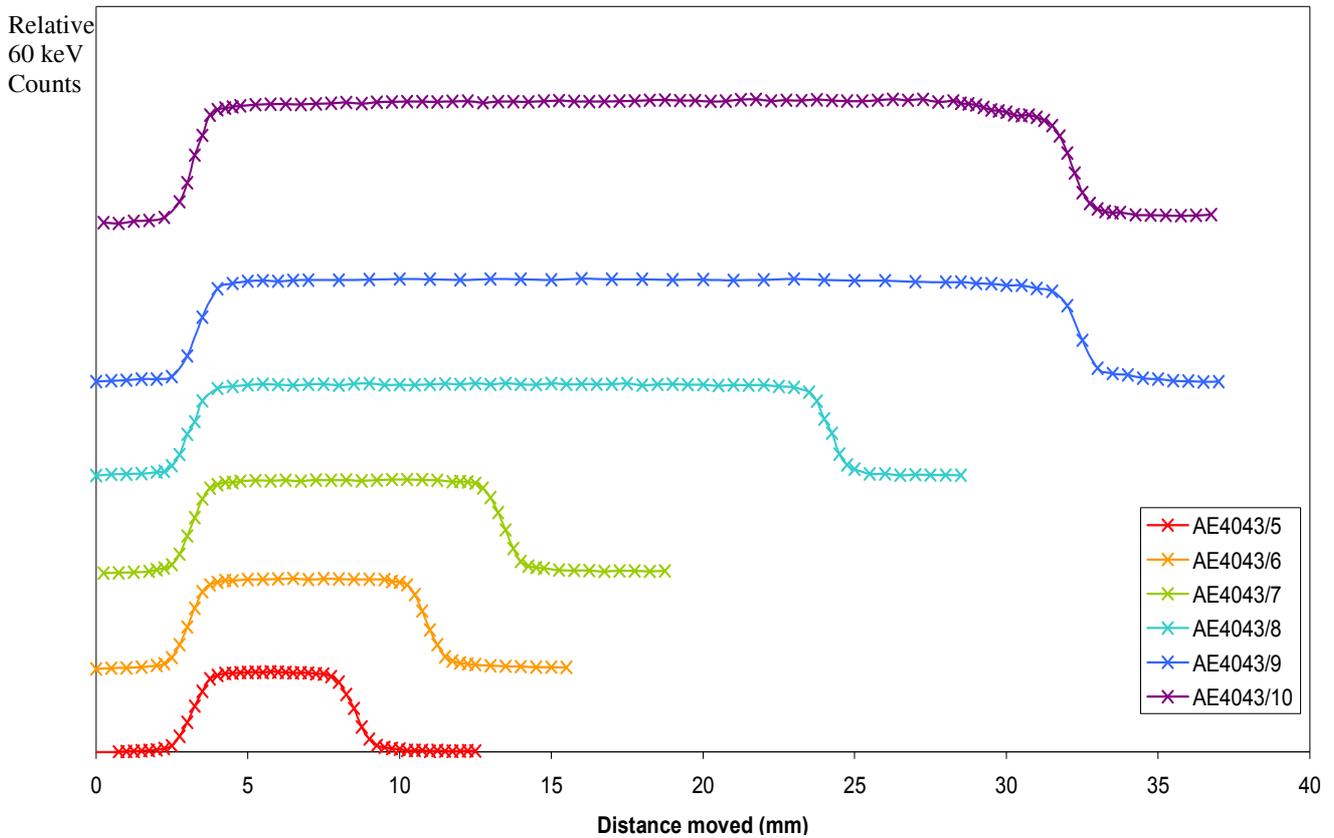
**Figure 16: Graph showing the relative 60 keV counts versus the distance moved for sources AE4043/5-10.**

**Table 4: AE 4043/5, 6, 7 & 8 measured FWHM and calculated densities using a NaI detector and Canberra Unispec.**

| Source | FWHM = fill height (mm) | Mass of $PuO_2$ (g) | Calculated Density (g.cm$^{-3}$) | Uncertainty (g.cm$^{-3}$) |
|---|---|---|---|---|
| AE4043/5 | $5.390 \pm 0.14$ | 5.56 | 2.14 | 0.11 |
| AE4043/6 | $7.876 \pm 0.14$ | 8.48 | 2.20 | 0.05 |
| AE4043/7 | $10.310 \pm 0.14$ | 11.30 | 2.23 | 0.03 |
| AE4043/8 | $21.092 \pm 0.14$ | 22.60 | 2.18 | 0.01 |

The heights of the maximum and minimum flat regions have been calculated using an average of all data points at this level and so their error is treated as negligible. Similarly, since the gradient is determined from the nearest two points then the gradient uncertainty is neglected. The FWHM uncertainty is calculated as the quadrature summing of the statistical measurement uncertainty ($\sqrt{N}$ where N is the number of counts) and the uncertainty in the location of the machine slide

(approximately 0.1 mm). The uncertainty in the density is then calculated by propagating through the uncertainty in the FWHM.

In some of the sources measured there is a small difference in start and end values, which may be due to the cap having a small groove along its outer edge, designed to allow air to flow out whilst it is being put in place, or may be due to loose powder residing above the cap if the inner capsule was contaminated during assembly. It should also be noted that these measurements were not background subtracted since an ROI was used to determine the 60keV counts rather than using the net peak area. Consequently the background may increase as the source is moved to a position where coherent scattering could affect the number of counts reaching the detector. Similarly if the side of the source was not completely parallel to the detector face then the flat top of the profile may appear to rise or fall as the source is scanned. Where a difference in start and end values is observed an average of the start and end value (the background level with the collimator not viewing the source) has been used as the background signal in the density calculations.

The results indicate that the $PuO_2$ powder inside the capsules have an average density of $\sim(2.19\pm0.04)$ g.cm$^{-3}$. However, it appears from the lower three results that the density is increasing with mass. This may be since the cap which holds the powder in place is held down by a cut spring. The uncompressed length of the cut springs is not documented. As the fill height increases there may more pressure from the spring and so the powder may be more compressed. However, observations of data from Figure 13 indicate that the 414 keV apparent mass behaves linearly with mass and so it is assumed that the density is approximately constant through the set of sources.

Observations of the spatial profile of the AE4043/10 (approximately 25g Pu) source (and AE4043/9 to a lesser extent) indicate that the internal geometry of the source is different to the others and so this result is not valid for the purpose of an average density estimation.
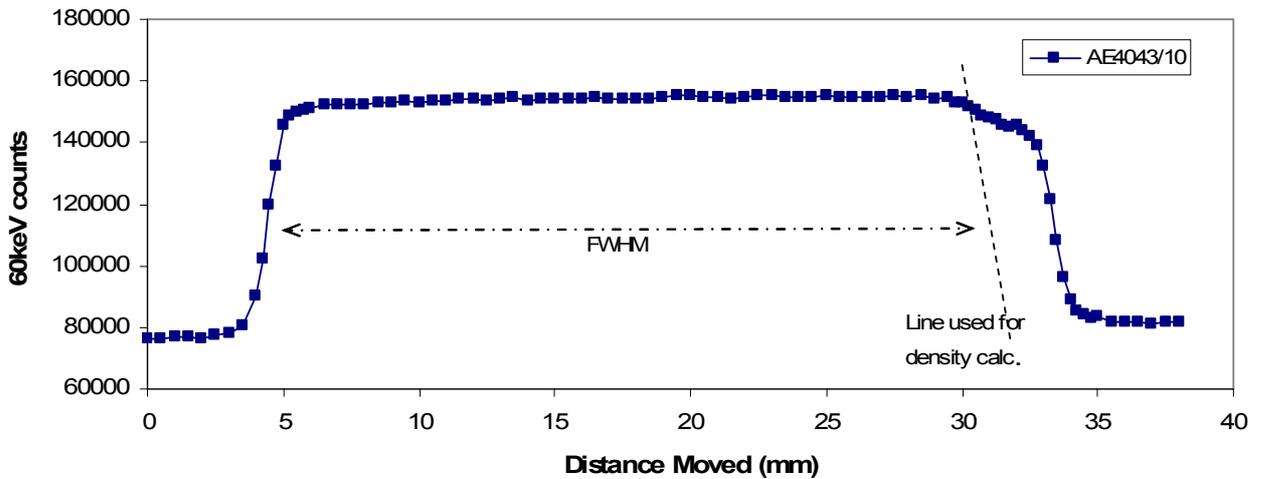
**Figure 17: Spatial profile for 60 keV activity distribution in the 25 g AE4043/10 source.**

The number of 60 keV counts versus distance moved graph for AE4043/10 is shown in Figure 17. The number of 60 keV counts rises similarly to the other sources, however the descending curve behaves somewhat differently; there is an initial slower decrease in the number of counts from 30 mm to 33 mm and then the number of counts decreases to a value slightly higher than the initial background level. This initial decrease may be due to the fact that this higher mass source does not contain a spring to hold the cap in place and so it is possible that the cap may have moved, allowing the $PuO_2$ powder to move more freely at the top of the capsule, and hence be less dense than the main body of powder.

To calculate the density of the main body of $PuO_2$ powder of the AE4043/10 source it has been assumed that the FWHM can be taken from the half maximum on the ascending line and the half maximum at an imaginary line drawn from where the countrate initially starts to descend. This assumption will give an approximate density of 2.17 $g.cm^{-3}$, whereas using the plotted descending line gives an average density of 1.99 $g.cm^{-3}$. A similar analysis of the AE4043/9 source gives 2.08 $g.cm^{-3}$ and 1.98 $g.cm^{-3}$ respectively.

### 3.3.3 AE4043/nn Powder Distribution Measurements

Previous testing of the AE4043/nn sources has shown the AE4043/1 source to have a consistently low mass of approximately 55 mg by gamma assay [50]. The cause of the low measured Pu mass

for the AE4043/1 sample may be a result of an asymmetrical Pu powder distribution, or the powder may reside within a ring on the outer diameter of the inner capsule due to the small fill-height, held in place by the raised edge on the base of the cup (see Figure 10). An experiment was set up to test this hypothesis.

The experimental set-up is similar to that shown in Figure 14 except that the source is rotated horizontally by $90^{\circ}$ so that the base of the source container is parallel to the flat surface of the detector. The 60 keV count rate is observed across the base of the AE4043/1 in two dimensions (i.e. by rotating the source about its axis $90^{\circ}$ and re-measuring) and the AE4043/5 serves as a control case to observe the expected behaviour for a source with uniformly-distributed activity. The resulting profile for the 5g source is shown in Figure 18 and demonstrates a symmetrical powder distribution. The profile is a dome shape since as the collimator is moved across the base of the capsule the visible chord length (y) increases as a function of the apothem (x) (or distance moved across the source) until the diameter length (R/2) is reached at the central position, and then decreases symmetrically using the equation below:

$$y = 2\sqrt{R^2 - x^2}$$ **Eqn. 11**

This equation has been normalised to the measured curve and plotted in Figure 18 to demonstrate the expected behaviour or the spatial profile. The two curves are equal when allowing for statistical fluctuations and so the AE4043/5 source may be assumed to be symmetrical with uniform $PuO_2$ powder distribution across the base of the capsule.
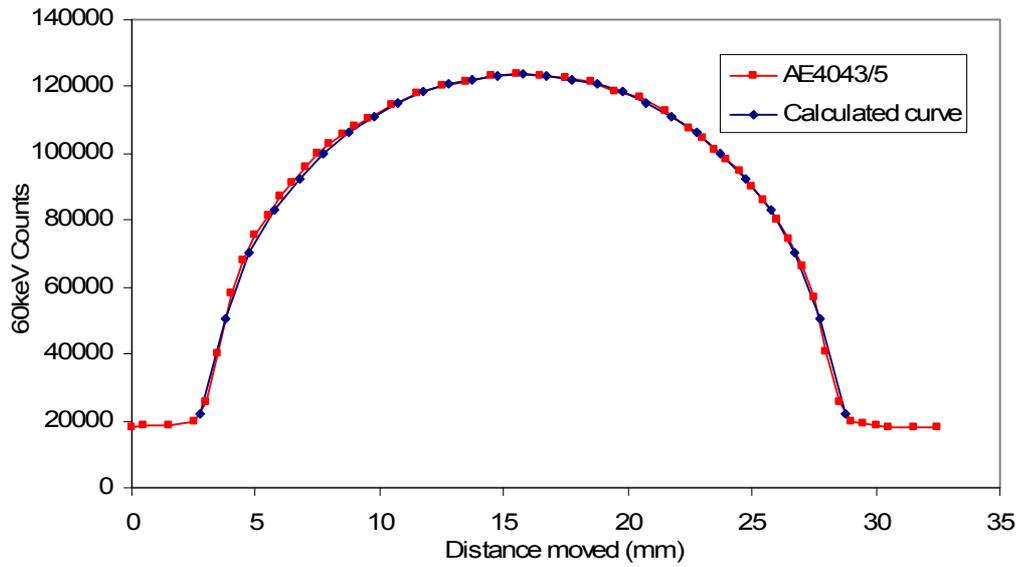
**Figure 18: The 60keV profile of AE4043/5 across the base demonstrating uniform PuO$_2$ powder distribution.**
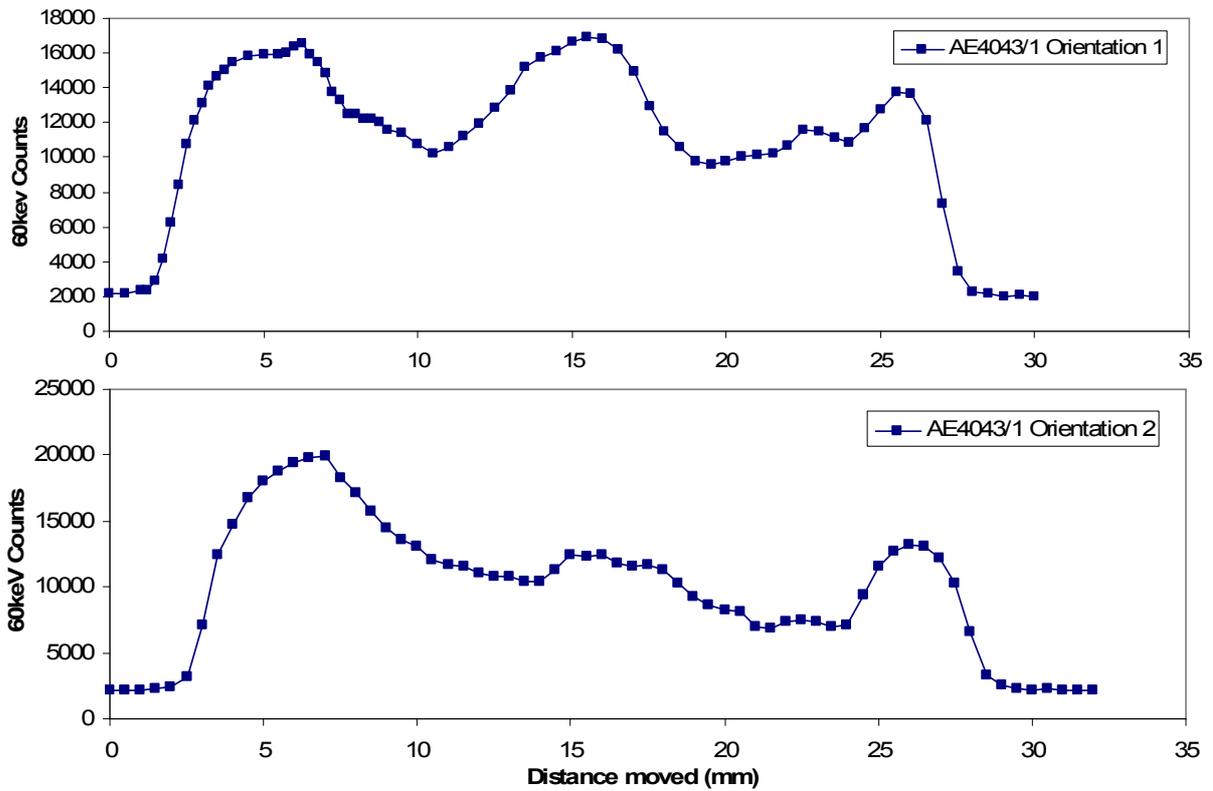


**Figure 19: The AE4043/1 source 60 keV profile across the base of the source in 2 different orientations.**

The profile for the AE4043/1 source is shown in Figure 19 for two different orientations with the source rotated about its axis by 90°. The number of counts for the two orientations is different in the centre since the source was not at a consistent distance from the detector and collimator; however the base of the source was set parallel to the collimator and detector face in each situation. The spatial profiles show that the activity is neither symmetrical nor uniform across the base of the capsule. The active material appears to reside mostly in the rim area around the outer edge of the inner capsule, with a possibly a small amount of active material remaining in the inner section.
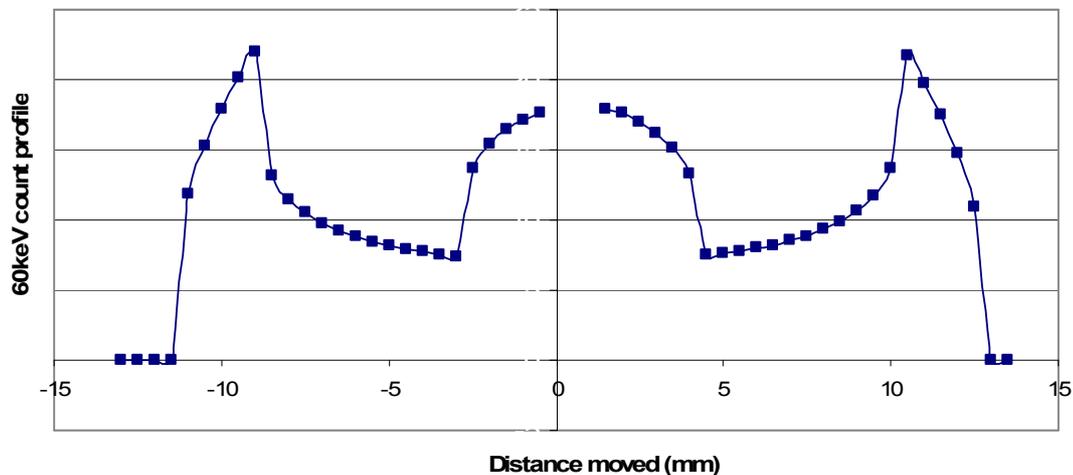


**Figure 20: Expected 60keV spatial profile for a uniformly thick source consisting of active powder in a 2.5mm thick ring around the outside plus a 4mm radius circle in the centre.**

Figure 20 demonstrates an example of the calculated spatial profile for a source consisting of a 2.5mm thick ring of active powder around the outside of the cap plus a 4mm radius circle of powder in the centre (where all powder has an equal fill height). The measured profiles are far less symmetric and the powder appears to be more randomly distributed across the central section, indicating that the $PuO_2$ powder may be mobile below the cap within the capsule. To test this, the AE4043/1 source has been measured in the same orientation a further two times after the source has been tapped gently on the left (Figure 21: Measurement 1) and the right (Figure 21: Measurement 2) i.e. at 90° either side of the measured orientation.
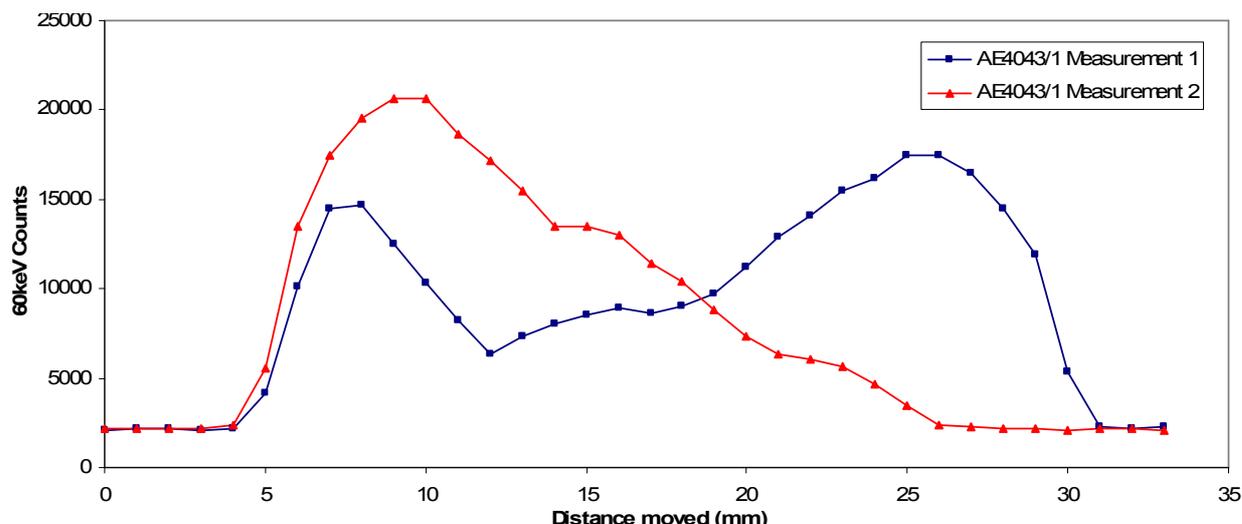
**Figure 21: AE4043/1 counts across the base of the source after gently tapping the capsule on either side.**

Figure 21 shows a clear difference between the two measurements. In each case the powder appears to have moved towards the lower side whilst tapped. The second "tapping" has caused the powder that once resided around the outer ring to slip to the opposite side. Consequently, due the unpredictability of this source it shall be omitted from future modelling and measurements.

### 3.3.4  AE4043 Modelling

Selected AE4043/nn sources (omitting sources AE4043/1, 9 and 10) have been modelled using the point source model to support the density and fill height measurement results in the previous section, and to assist in validating the point source model.

**Table 5: AE source Pu and PuO$_2$ content and calculated fill heights assuming a density of 2.19 g.cm$^{-3}$.**

| Source ID | PuO$_2$ mass (g) | Pu mass (g) | Fill height (mm) |
|-----------|------------------|-------------|------------------|
| AE4043/2  | 0.565            | 0.494       | 0.53             |
| AE4043/3  | 1.128            | 0.986       | 1.05             |
| AE4043/4  | 2.261            | 1.977       | 2.10             |
| AE4043/5  | 5.650            | 4.941       | 5.26             |
| AE4043/6  | 8.479            | 7.414       | 7.89             |
| AE4043/7  | 11.298           | 9.879       | 10.51            |
| AE4043/8  | 22.597           | 19.758      | 21.02            |

The $PuO_2$ density is assumed to be 2.19 g/cm$^3$ (as determined in section 3.3.2), and the material is uniformly distributed (excepting sources AE4043/1, 9 and 10 - see section 3.3.3). From these assumptions the thickness of the $PuO_2$ powder may be calculated as being in the range 0.1 mm to 26.3 mm (see Table 5).
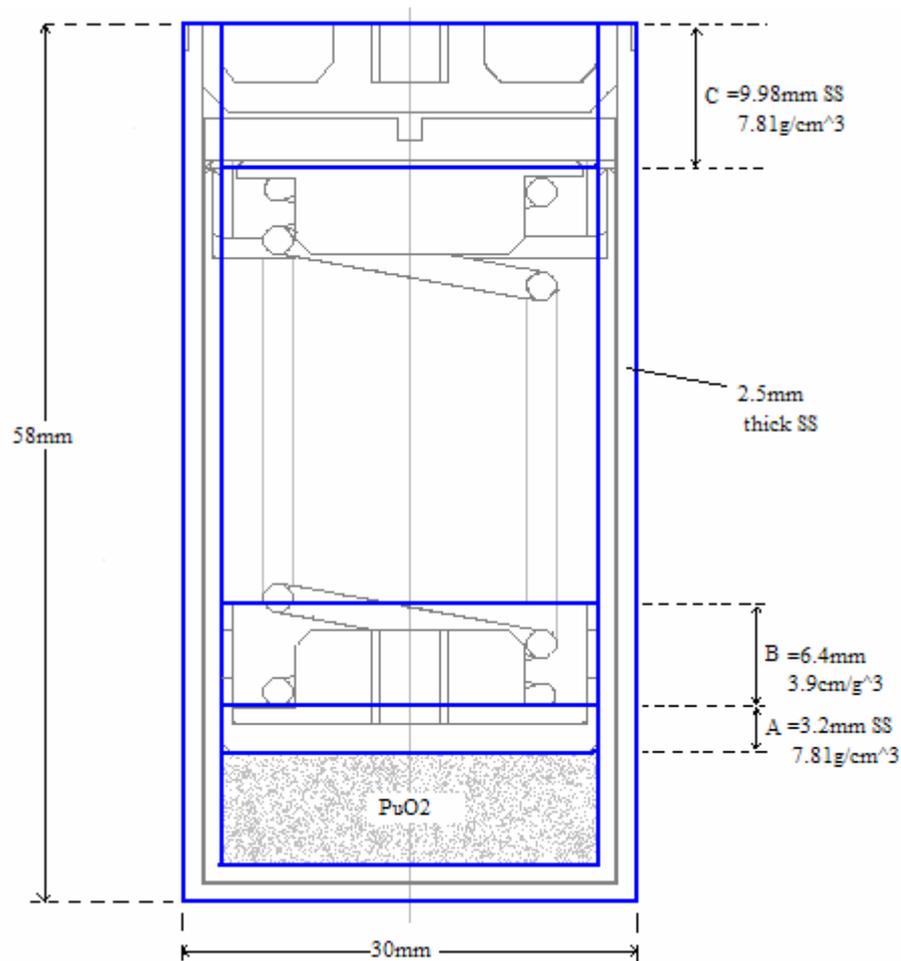


**Figure 22: AE4043/nn source showing blue lines for the modelled set-up.**

The stainless steel (SS) is modelled using the Genie 2000 ISOCS MuEditor program as:

- C: 0.08%
- Cr: 19.0%
- Fe: 71.92%
- Ni: 9.0%

with a density of 7.81 g.cm$^{-3}$. The AE4043/nn source is modelled as shown by the blue lines in Figure 22. Areas A and C and the outer encapsulation are modelled as solid SS. Area B has been modelled as SS with half the normal density, 3.905 g.cm$^{-3}$. Due to the manufacture process of the sources all Pu powder should reside within the area below the cap in the inner capsule, and the powder should be distributed symmetrically within this area. The sources have been modelled with this distribution, with the fill heights stated in Table 5.

The detector has been modelled as a 7 cm diameter, 2.1 cm thick uncollimated detector at 40cm from the source, to mirror the experimental set-up. The ratio of attenuated to unattenuated counts have been recorded for the 129 keV and 414 keV lines for the 7 selected sources.

Preliminary results show that for both lines the modelled results are larger than the measured results taken from the AE4043/nn Preliminary Source Measurements (section 3.3.1). However, there are a number of factors which could bias the measured and modelled results. For example the measured results depend on the accuracy of techniques such as the efficiency and deadtime corrections, and nuclide library parameters such as the branching ratio of the lines. If these are not accurate then the modelled and measured results will differ. The modelled results also may be affected by encapsulation assumptions, the estimated average density or the value of the attenuation coefficient ($\mu$) used. These preliminary results use a value of $\mu$ as set by Genie ISOCS (see section 2.2) which neglects coherent scattering. The modelling has been repeated with $\mu$s from the XCOM database [15] both with and without coherent scattering (see Figure 23).

For all sets of results the plots "dip" for the 5 g source. This may be due to an anomaly in the measured dataset. Also the smaller sources appear to have a lower measured to modelled ratio; this may be a consequence of a non-uniform density across the set of sources.
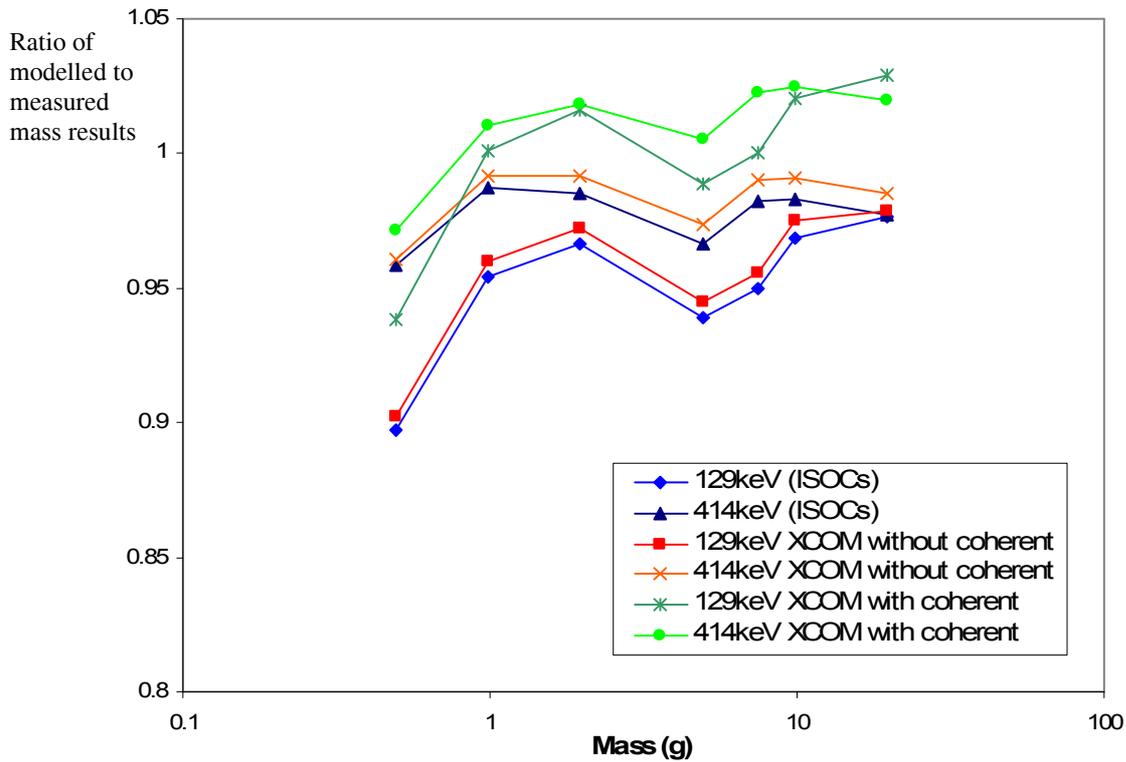
**Figure 23: Graph showing the measured (from Preliminary Source Measurement data, see section 3.3.1) to modelled mass ratio for selected AE4043/nn sources for the 129 keV and 414 keV lines for different μs.**

The results show that the XCOM μ without coherent scattering, although improving the measured to modelled ratio compared to that for the original Genie ISOCs μ, still produces modelled results which are too large, whereas, on average the XCOM μ with coherent scattering produces modelled results that are slightly too small. This is since if the μ includes coherent scattering the attenuation coefficient (and collision cross-section) is larger and so the apparent mass calculated by the model will be smaller. Physically the apparent μ (the μ that should be used in the model to produce the result that you would obtain with all the scattering in the real sample) may lie somewhere between the two values since the attenuation coefficients do not take account for situations where the gamma ray is initially not directed towards the detector but is coherently scattered towards it. It would be possible to determine the true $\mu$ by modelling the geometrical set-up of the experiment, including surrounding objects and equipment, using complex models such as MCNP, however this has not been performed since the benefit of the results would not be significant for the purposes of this thesis.

The XCOM $\mu$ with coherent scattering will be used since the individual 129 keV and 414 keV apparent mass results are nearest to the measured results out of the studied $\mu$ types.

## 3.4 Fleissner Method Analysis

### 3.4.1 The Two-Line Method

The behaviour of bare Pu cylinders (i.e. not encapsulated within stainless steel) of diameter equal to height have been calculated with the point source model using the basic two-line (129 keV and 414 keV) Fleissner method for three different densities: pure Pu at $\rho = 19.8$ g.cm$^{-3}$, PuO$_2$ at $\rho = 1.856$ g.cm$^{-3}$ and PuF$_3$ at $\rho = 7.1$ g.cm$^{-3}$, over the mass range 0.1 mg to 200 g. In the model it is assumed that the cylinder is viewed in the far field by a detector located along a mid-plane diameter.

The parameters for the bare Pu cylinders are inputted and the total (uniform source) counts rates are determined. The calculation is then repeated with the density in the attenuation function set to zero. The ratio of these two results gives the self-attenuation factor (SAF$_i$ of the i'th energy). The apparent mass ($M_i$ of the i'th energy) is then calculated as:

$$M_i = SAF_i M_{TIn}$$ 

**Eqn. 12**

where M$_{TIn}$ is the inputted true mass of the cylinder. The simplified Fleissner equation:

$$M_i = M^o e^{-\beta/E_i}$$

**Eqn. 13**

may be rearranged using the 129 keV and 414 keV lines to show that the model parameter, β, may be given by:

$$\beta = \frac{\ln\left(\dfrac{M_{129}}{M_{414}}\right)}{\left(\dfrac{1}{414} - \dfrac{1}{129}\right)}$$

**Eqn. 14**

and hence:

$$M^o = M_{129}.e^{\frac{\beta}{129}} = M_{414}.e^{\frac{\beta}{414}}$$

**Eqn. 15**

where M$^o$ is the Fleissner method corrected mass. The over-correction (the ratio of the corrected mass to the true mass for the basic Fleissner method) is displayed on Figure 24.
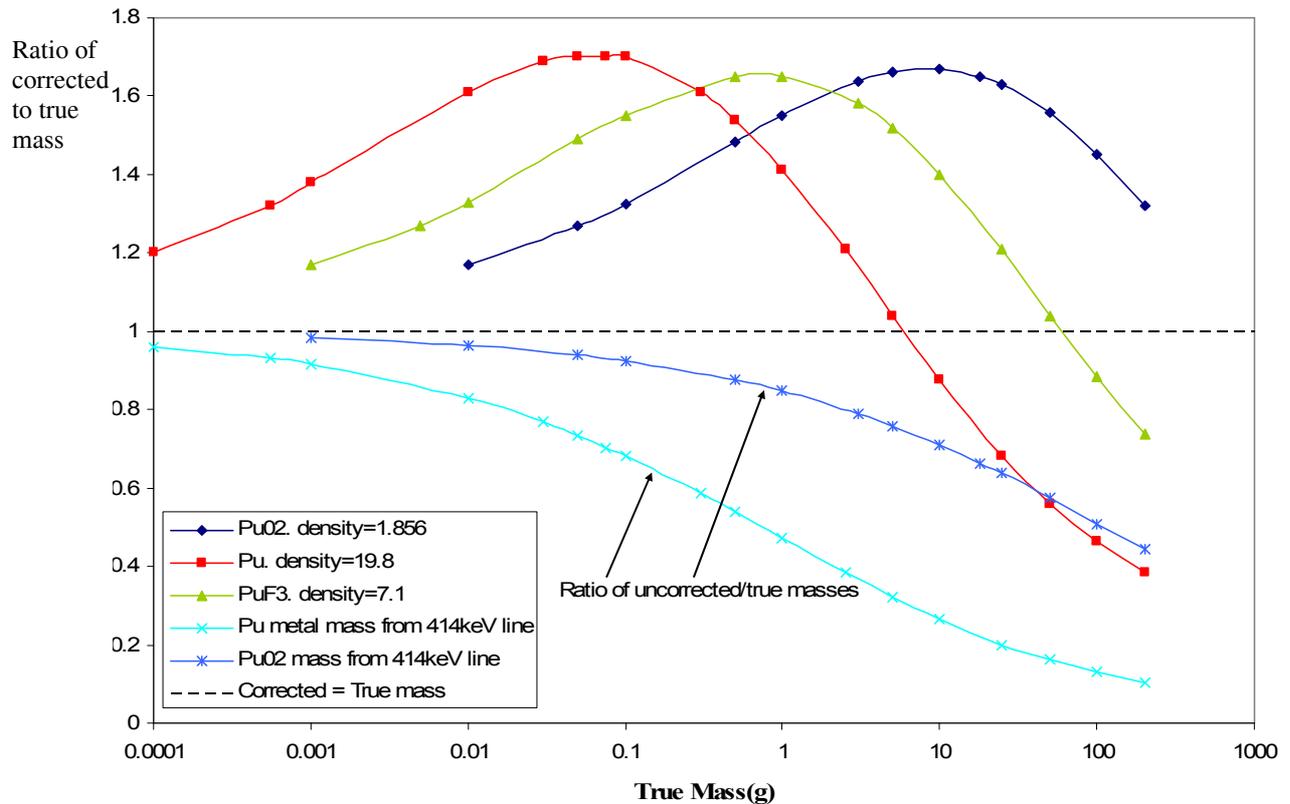
**Figure 24: The basic Fleissner SAC mass versus True mass for Pu Metal, PuO₂ and PuF₃ cylinders.**

The graph shows that the default Fleissner method not only over-corrects by a factor of 1.5 at intermediate masses, but also severely under-corrects at higher masses for Pu metal lumps. For example, a 100 g Pu metal lump would appear as only 50 g, a 50% under-determination. In many routine waste assay situations this is not a serious concern because the maximum single lump size is expected to be far smaller than this. For example, in fabrication facilities the waste is restricted to items such as fine oxide powder, grindings and pellet chips. Similarly in a glove box clean-out exercise visual inspection, screening and packing records are often available to confirm maximum lump size. However, historical waste from weapons production facilities may pose particular concern since records may be incomplete.

The graph also shows curves that would be obtained from the 414 keV line with no SAC correction. These curves indicate that for a range of masses (particularly below 100 mg for Pu

known to be in the form of oxide) it might be better to offer no correction at all rather than to use the Fleissner 2-line approach.

## 3.4.2 The Three-Line Method

The three-line Fleissner method has been calculated for bare Pu cylinders of diameter equal to height inside a stainless steel (1.6 mm thick) drum using the 129 keV, 375 keV and 414 keV lines of $^{239}$Pu. The point source model has been used in the same manner as for the two-line Fleissner method to determine the apparent mass of the three lines (129 keV, 375 keV and 414 keV). The full Fleissner equation has been rearranged as:

$$f(M_0, \alpha, \beta) = M^0 - M_i \left( 1 + \alpha \left( e^{-\beta/E_i} - 1 \right) \right)^{-1} = 0 \qquad \textbf{Eqn. 16}$$

to determine values for $\alpha$ (constrained to be $\leq 1$), $\beta$ and hence $M_0$ using a numerical technique. If it is assumed that the data is well behaved and a solution exists we may suppose that:

$$f(M^0 + \delta M^0, \alpha + \delta\alpha, \beta + \delta\beta) = \varepsilon_i \qquad \textbf{Eqn. 17}$$

then a solution must be found where:

$$\delta \left( \sum_i \varepsilon_i^2 \right) = 0 \qquad \textbf{Eqn. 18}$$

This has been performed by incrementing each parameter $M^0$, $\alpha$ and $\beta$ in turn and finding the minimum value of $\sum_i \varepsilon_i^2$. The corresponding $M^0$, $\alpha$ or $\beta$ is then set as an input parameter and the process iterated until $\sqrt{\sum_i \varepsilon_i^2}$ reaches a value less than 5% of the value of $M^0$.

During this process it was found that the determined parameters would not settle where $\alpha$ was less than 1 since the absorption in the modelled lump is entirely due to the self absorption within the sample and thus the method reduces to the 2-line Fleissner method, as studied in the previous section.

A graph showing $\alpha e^{-\frac{\beta}{E_i}} + (1-\alpha)$ and $e^{-\mu\rho x}$ for an arbitrary thickness, x, has been plotted as a function of energy in Figure 25. The plotted α-constrained $\alpha e^{-\frac{\beta}{E_i}} + (1-\alpha)$ has used an α of 0.9 and β of 200. Although it may fit the $e^{-\mu\rho x}$ curve at 414 and 375 keV it can not fit the curve at 129 keV. If the value of α is unconstrained it offers the best fit to the $e^{-\mu\rho x}$ curve at the three energies with α ~ 1.013 and β ~ 120.
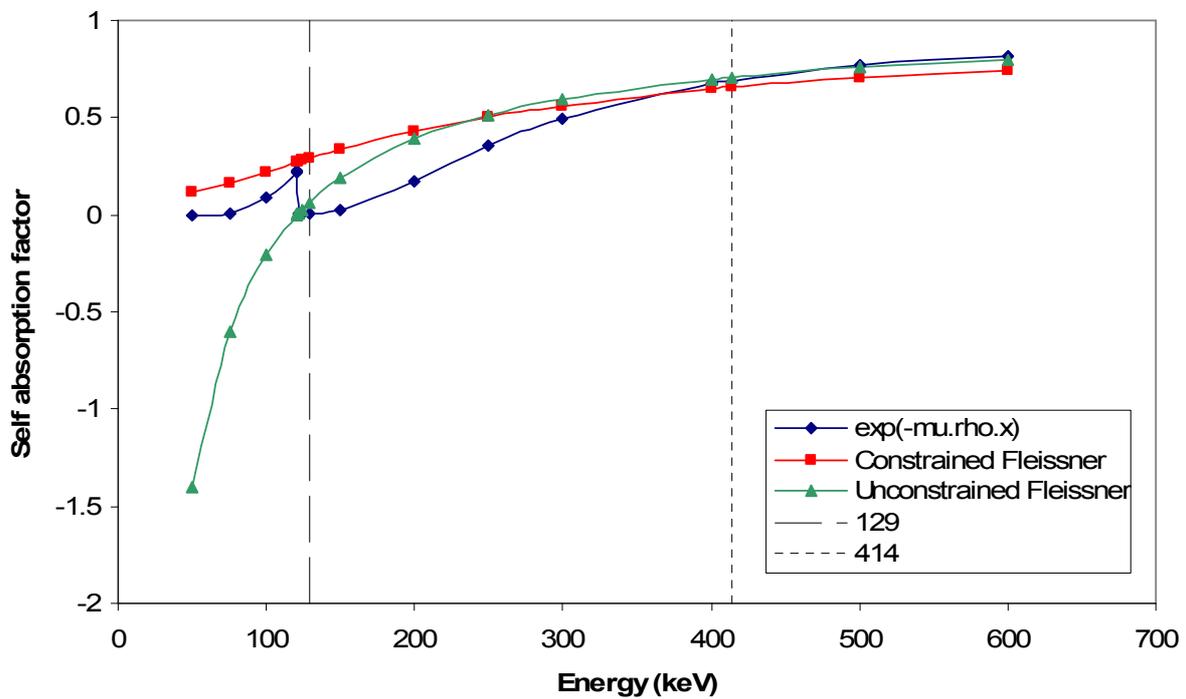


**Figure 25: A graph comparing $\alpha e^{-\frac{\beta}{E_i}} + (1-\alpha)$ with constrained and unconstrained α as a function of energy compared to $e^{-\mu\rho x}$.**

Since it has been found that the attenuation curve (at 129 keV and 414 keV) may best be fitted with an unconstrained value of α, the corrected mass has been determined using the 3-line Fleissner equation with this method. Using the unconstrained parameters the value of β was found to remain close to 1.01, whereas α increases steeply until approximately 5 g and then converges to 121.3 (for Pu lumps) and 120.1 (for $PuO_2$ and $PuF_3$ lumps), as shown in Figure 26. This value of α

is far from unity and indicates that the assumption that made by the 2-line method is a poor approximation. However, in physical reality $\alpha = 1$ should be correct since all the Pu is subject to self-absorption.

The ratio of the corrected mass to the true mass for the modelled data is illustrated in Figure 27. The 3-line method is shown to perform much better than the 2-line approximation for smaller masses (below 1g) but begins to severely under-correct as the mass increases, particularly for the Pu metal lumps.
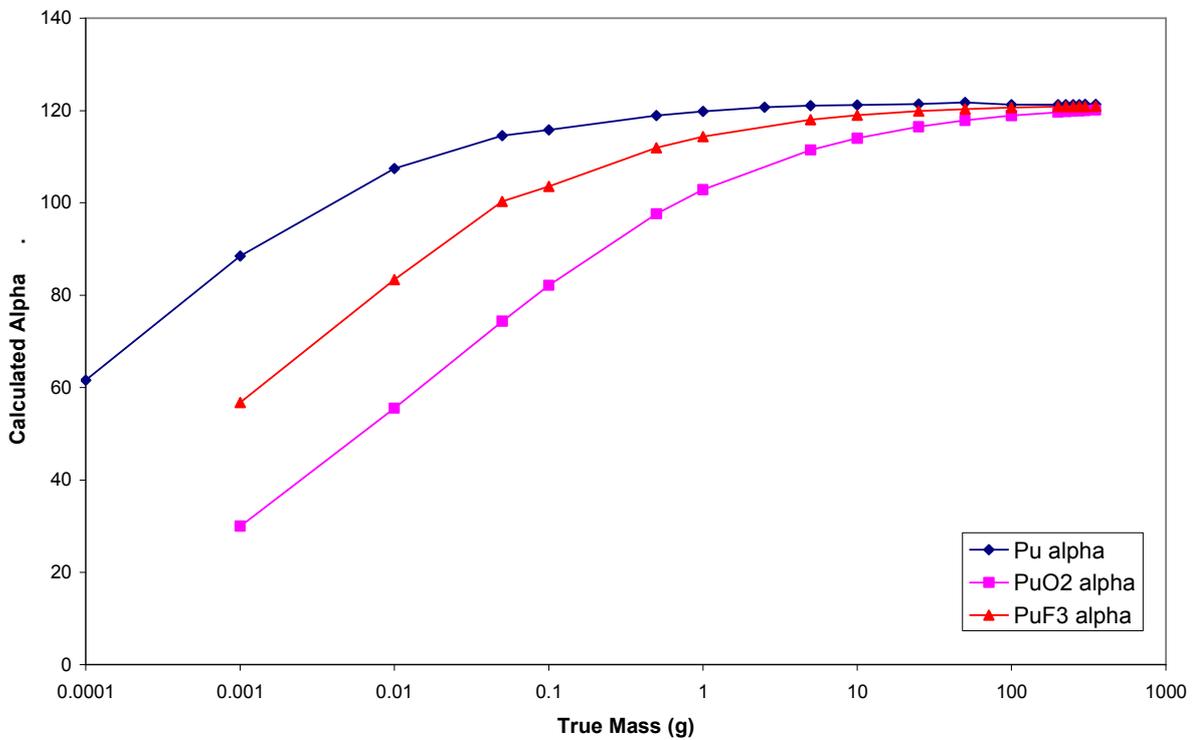


**Figure 26: The calculated alpha parameter versus true mass of the lump using the 3-line Fleissner method.**
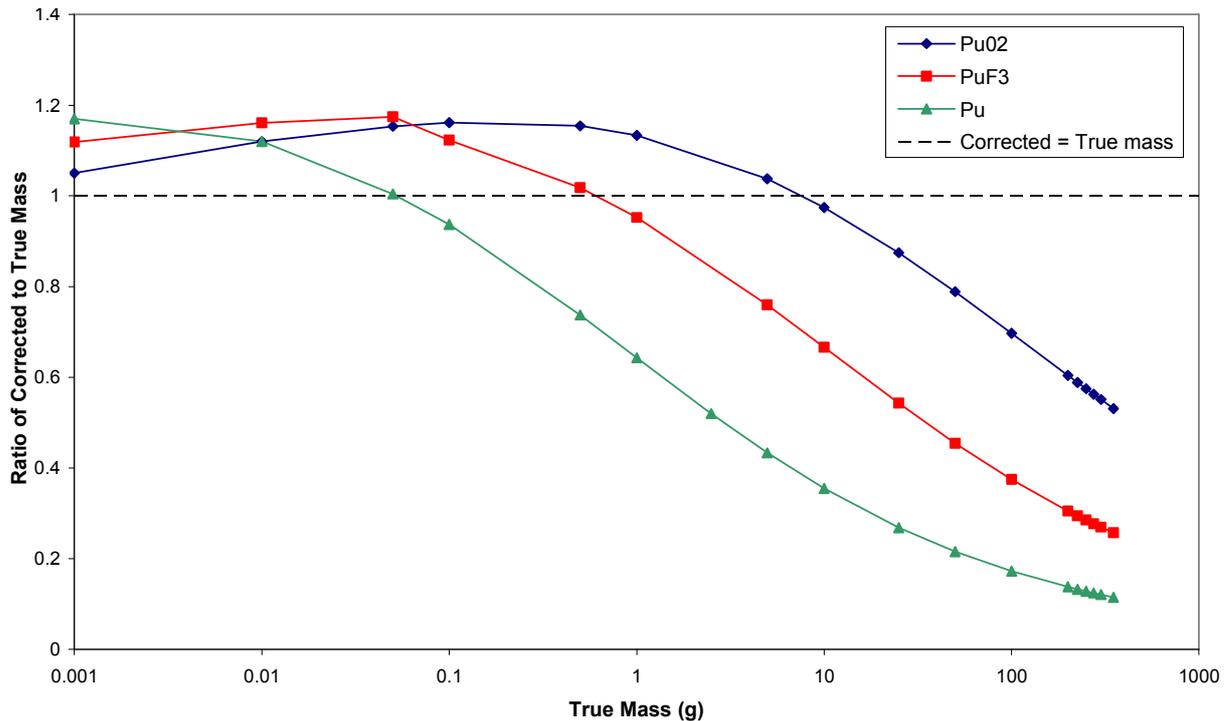
**Figure 27: The ratio of corrected to true masses for Pu, PuO$_2$ and PuF$_3$ versus true mass for the 3-line Fleissner method.**

## 3.5   General Self-Absorption Analysis

The analysis of the uncorrected behaviour of self-absorption for cylinders has been extended to a number of other rotating geometries over the range 1 mg to 350 g. These are listed below:

- Cylinders with diameter equal to height (as shown above)

- Square faced plates with a fixed depth of $1.0 \times 10^{-3}$ m and the square side ranging from $2.0 \times 10^{-4}$ m to 433 mm

- Rods with a fixed length of 0.1 m, with diameters ranging from $2.5 \times 10^{-5}$ m to $4.9 \times 10^{-2}$ m

- Cubes of side length ranging $3.0 \times 10^{-4}$ m to $5.7 \times 10^{-2}$ m

- Plates of fixed square face length $3.0 \times 10^{-3}$ m with heights ranging from $5.0 \times 10^{-7}$ m to 8.4 m

- Plates of fixed square face length $3.0 \times 10^{-2}$ m with heights ranging from $2.0 \times 10^{-7}$ m to 0.2 m

- Plates of fixed square face length 0.1 m with heights ranging from $2.0 \times 10^{-7}$ m to $1.9 \times 10^{-2}$ m

- Zero attenuation geometry (129 keV mass = 414 keV mass = true mass)

Figure 28 shows $M_2$ (the apparent mass of the 414 keV line) plotted against $M_1$ (the apparent mass at 129 keV) for a selection of these materials/shapes with lines of constant true mass in the range 0.001-350 g shown in black, creating an interesting and useful 3D surface whose properties may be used to approximate a more accurate mass based upon the measured (observed apparent) masses of the 129 keV and 414 keV lines.

The diagonal line where $M_1$ equals $M_2$ in Figure 28 is the case of no attenuation, where $M_1$, $M_2$ and the true mass are all equal in value. It is physically impossible for a lump to produce a data point in the region below this line, although this may be observed experimentally due to statistical fluctuations. The curve at the furthest distance from the no-attenuation line is the case for Pu cylinders (the most attenuating material and shape considered). Tiny massed lumps of Pu that do not experience attenuation will lie on the no-attenuation line. As their mass increases and the 129 keV and 414 keV lines become more attenuated, the curve migrates towards the highest attenuation curve. As the mass increases further they saturate and the points bunch together on the most attenuating line. For a solid, homogeneous, non-re-entrant body the sphere is the worst possible case, however the Pu cylinder is the closest modelled example and so no data point should reside beyond this curve.

Based on this database of calculated results a new Pu SAC method (a software engine) has been developed to calculate the mass of Pu from the two apparent masses $M_1$ and $M_2$, and has been used to demonstrate the effectiveness of the new self-absorption technique. This method is described in section 3.7.
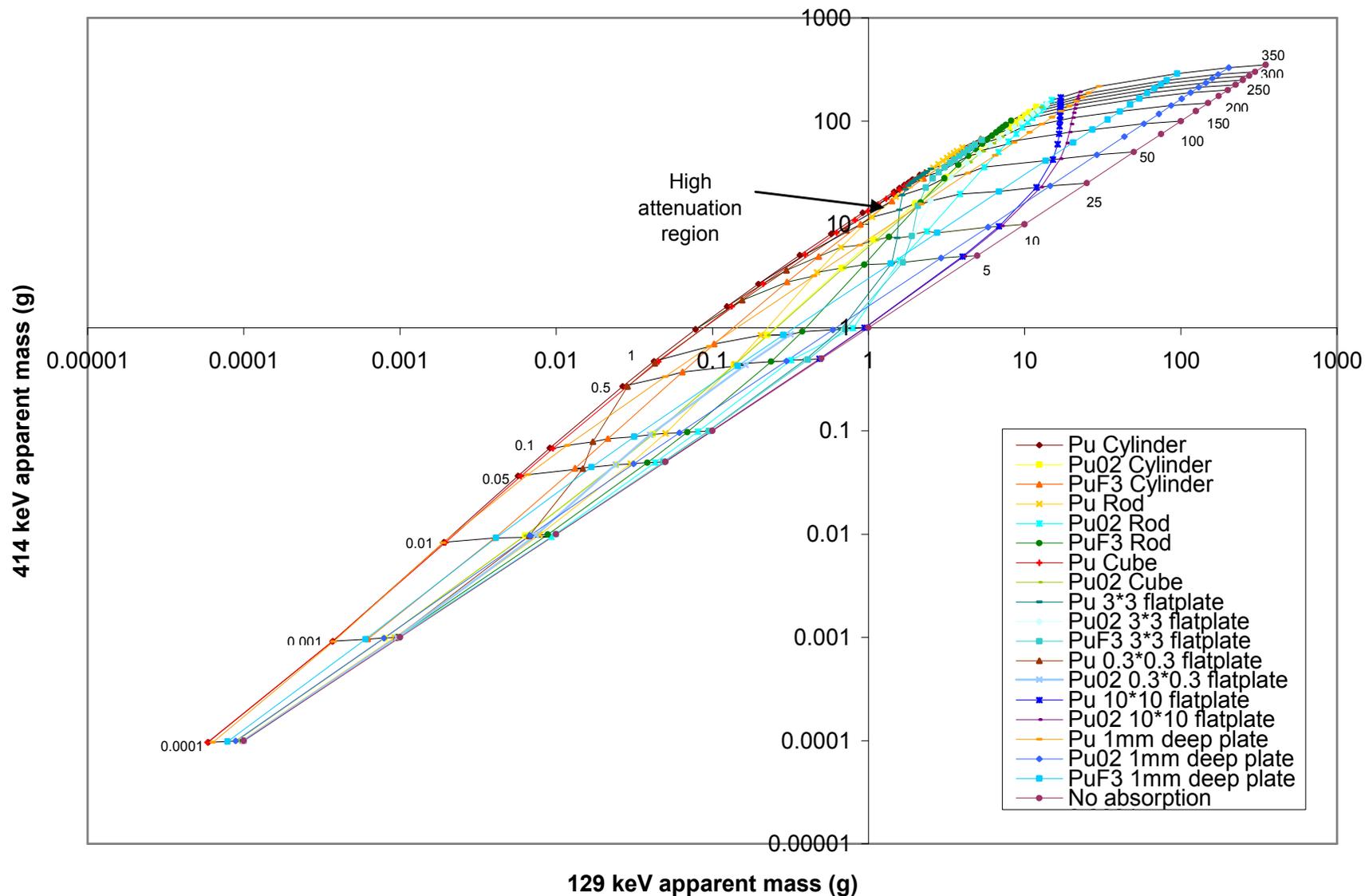
**Figure 28: Apparent Masses of the 414 keV Line vs the 129 keV Line.**

## 3.6   Effects of Integration Intervals in Modelling

During the modelling process it was noted that the number of integration intervals used by the point source model has an effect on the resulting counts detected. The model divides the specified lump into a number of voxels, determined by the user-defined number of integration intervals in the relevant dimensions. These are radial, polar and height integration intervals for cylindrical lumps, and lateral, depth, height and rotation integration intervals for cuboidal lumps. The model sets the gamma-ray production in each voxel using the volume of the voxel and computes the probability of the gamma-rays reaching the detector without scattering or absorption.

A study has been performed to observe the effect of the number of integration intervals used by the point source model using a 5 g un-encapsulated cylindrical Pu lump (with diameter equal to height). Each interval dimension (radial, polar, and height, as demonstrated in Figure 29) is varied in turn from 1 to 100, with the remaining interval values set to 100.
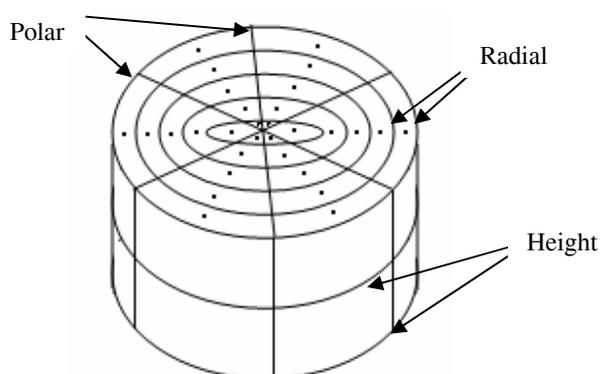


**Figure 29: Radial, polar and height integration intervals for a cylinder.**

A graph of the apparent mass versus the number of radial integration intervals for the 129 keV line is shown in Figure 30. If the number of intervals is too small and the number of gamma-rays escaping the material decreases exponentially with distance from the edge of the lump, since the absorption is calculated from the centre of the voxel in which the μ is assumed to be constant, the

region of least absorption nearest the edge of the lump is neglected. This causes an underestimation of the apparent mass for too few radial intervals.
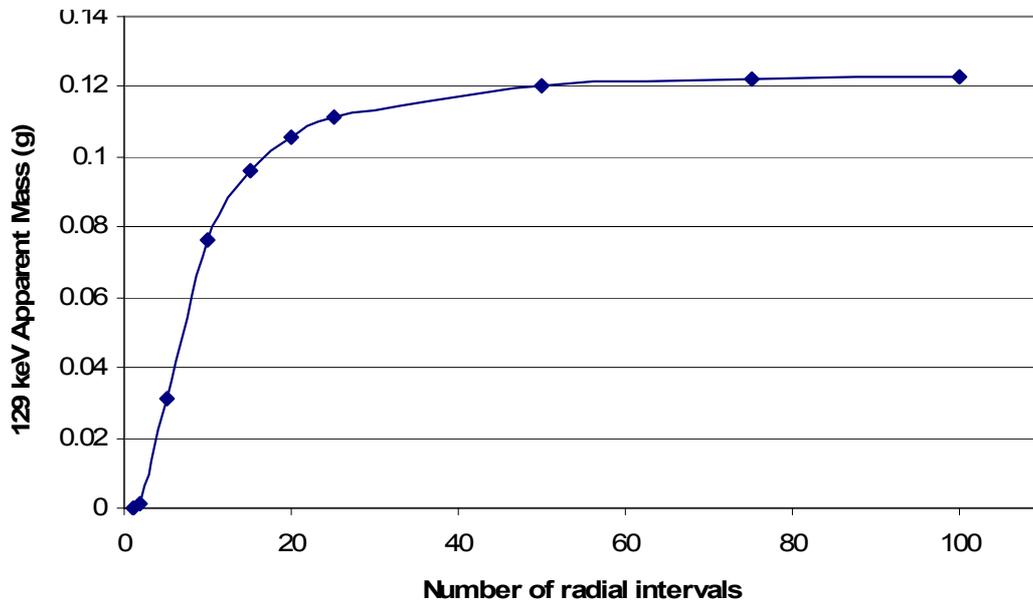


**Figure 30: The apparent mass of the 129 keV line for a 5g Pu cylinder as the number of radial intervals is varied.**

The number of height and polar intervals do not affect the result as strongly as the radial intervals. These show a slightly fluctuating effect below 10 intervals, and then reach a constant value since for this example each height and polar segment are adequately estimated by this number of intervals. Cylindrical lumps with different masses (modelled for 0.001 g and 20 g lumps) follow a similar pattern as the number of intervals is varied, except that the variation with radial intervals settles more quickly for smaller masses since each voxel is smaller.

During the point source data modelling process, the number of integration intervals was set as large as possible with, for the largest lump, the distance from the centre of the outermost voxel to the edge of the lump set to be much less than $1/\mu\rho$. For example, for the 5g cylinder at 129 keV with a diameter of 0.68cm and a density of 19.8 $g/cm^3$, the number of radial intervals should be

greater than $\dfrac{\mu\rho \times diam}{2} \approx 25$. However, whilst determining the number of intervals for a particular lump the modelling time and CPU usage was also a factor which needed to be taken into account. For example, a cylinder with integration intervals of 500-500-500 with two detectors at 99% CPU usage took 21 minutes to complete.

The number of integration intervals used in the model for each set of lump types used for the Pu SAC algorithm has been based upon the largest lump, varying the number of intervals in each dimension so that the counts per second calculated did not vary by more 1%.

## 3.7    A New Pu SAC Method

In order to use the modelled data to obtain a SAC mass from the two apparent masses, for each material and shape combination modelled in section 0, a cubic spline method has been used to plot curves for the true mass ($M_T$) versus $M_2$, and $M_1$ (129 keV line) versus $M_2$ (414 keV line), to obtain the self-absorption corrected mass and $M_1$ as functions of $M_2$.

Using these splines, for every $M_2$ we may take a slice of the surface with varying true mass and $M_1$ and observe a range of ($M_1$, $M_T$) pairs which are plotted against one another (see Figure 32). By using the measured value of $M_1$, and treating the locus between successive points as a straight line, the SAC mass may be found. If the $M_2$ co-ordinate lies outside the 3D surface, a least squares fit is used with the nearest 4 points.

A software engine has been developed using Borland Delphi$^{TM}$ as a stand-alone Pu Self Absorption Correction engine.

### 3.7.1    Engine description

The Pu SAC engine was designed to perform as part of a complete assay system; however its main function has been separated so that it can be used for manually inputted values.

The engine requires four values to be inputted. These are the total Pu apparent masses for the 129 keV and 414 keV lines and their uncertainties. If the known masses are for $^{239}$Pu then the values must be scaled using the correct $^{239}$Pu isotopic value to account for the absorption of the other Pu isotopes, since the model is designed to perform on pure Pu apparent masses.

Due to counting statistics for cases of near-zero attenuation, the 129 keV mass may appear to be slightly greater than the 414 keV line mass. In this case the program will set the two lines' masses to be equal to the 414 keV line mass and will assign no attenuation.

The program tests the limits of the data to ensure there are enough points to perform the calculation correctly. Since the individual materials' curves are fitted only to the maximum point

used in the development stage, the 3D shape is undefined beyond these points (which differ between materials). There must be at least 4 points in order for the program to process the least squares fit, therefore the maximum inputted value of the 414 keV line mass is 216.84 g. Beyond, or equal to this limit the program will set the result to be 216.84 g and the errors become meaningless. However this limit is not an inherent limitation of the general approach just described. It is rather a pragmatic limit set, at this time, by the amount of modelling work undertaken as part of this study to define the 3D surface.

Similarly, there is a minimum limit below which the curve is undefined, which is 0.000097g. Since at very low masses the attenuation is negligible, if the 414 keV line mass is below this value the program will accept the inputted 414 keV mass. In practice the lower limit plays little role since the correction is negligible and the signal will ultimately fall below the detection limits.

The program then uses a cubic spline method based upon that used in J. Wood's "Computational Methods in Reactor Shielding" [51] to obtain curves for $M_1$ and $M_T$ versus $M_2$. The inputted 414 keV mass ($M_2$) is used along with the splines to calculate co-ordinates for a plot of the 129 keV line mass versus true mass i.e. to calculate the co-ordinates of points of a cross-section of the 3D shape for a specific 414 keV line mass. Additionally there is the case of zero-attenuation, where the true mass and 129 keV mass are both equal to $M_2$.

The next stage of the program uses a series of loops to rearrange the data so that the 129 keV masses ($M_1$) for each material and their corresponding true masses are in ascending order, using a bubble (or exchange) sorting method [52]. The basic process for this section is to look at each $M_1$ in turn and test to see if it is greater than the previous, and if so, to move the appropriate array components to place the data in ascending order. The zeroes are filtered to the beginning of the array.

Once the data are correctly ordered the self-absorption corrected mass must be found for the inputted 129 keV line mass from the series of $M_2, M_T$ pairs. An example of this relationship for an $M_2$ of 5 g is shown in Figure 31.
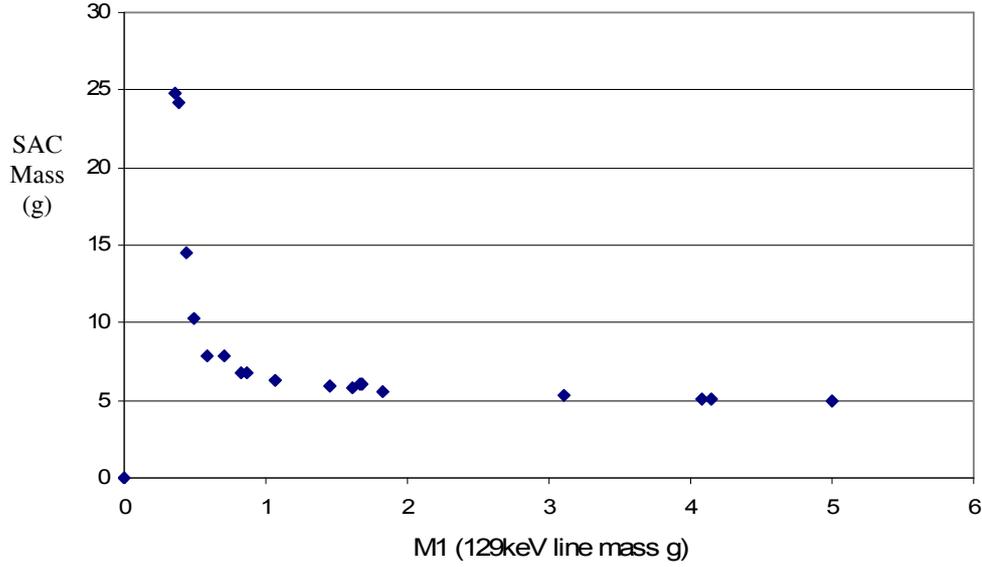
**Figure 31: An example of $M_1$, $M_T$ pairs calculated by the new SAC algorithm for $M_2 = 5g$.**

For the given 129 keV line (1.25 g in this example) the SAC mass must be found. This is done by assuming that the curve joining each two adjacent points is a straight line. We must first therefore, find between which two points the inputted $M_1$ lies. The SAC mass is then found using the equation of a straight line:

$$SACMass = \frac{M1In.(M_T[n+1] - M_T[n])}{(M_1[n+1] - M_1[n])} + M_T[n] - \frac{M_1[n](M_T[n+1] - M_T[n])}{(M_1[n+1] - M_1[n])} \quad \textbf{Eqn. 19}$$

where *M1In* is the inputted 129 keV line mass, $M_1[n]$ is the array of 129 keV masses for individual materials found from a cross-section of the 3D surface, $M_T[n]$ is the array of true masses for individual materials found from a cross-section of the 3D surface, and [n] and [n+1] are the array components between which the inputted 129 keV mass lies.

If the inputted 129 keV line mass is greater than the largest $M_1$ on the graph, then a least squares fit is used on the last 4 points, and the line extended to determine the value of the SAC mass. The equation for the least squares fit is shown below.

$$SACMass = M1In \times \frac{\left(4 \times \sum M_1 M_T - \sum M_1 \sum M_T\right)}{\left(4 \times \sum M_1^2 - \left(\sum M_1\right)^2\right)} + \frac{\left(\sum M_1^2 \sum M_T - \sum M_1 M_T \sum M_1\right)}{\left(4 \times \sum M_1^2 - \left(\sum M_1\right)^2\right)} \quad \textbf{Eqn. 20}$$

The uncertainties (one sigma) on the corrected mass arising from the uncertainties in the measured apparent masses, based on the assumption that a single lump is present, have been implemented within the engine using the following equation:

$$\sigma_{M_T}{}^2 = \left( \frac{\delta M_T}{\delta_1} . \Delta M_1 \right)^2 + \left( \frac{\delta M_T}{\delta_2} . \Delta M_2 \right)^2 \qquad \textbf{Eqn. 21}$$

where $\delta_1 = 0.001 \times M_1$, $\delta_2 = 0.001 \times M_2$ and $\Delta M_n$ are the inputted uncertainty in the 129 keV or 414 keV masses. Partial differentials are found by propagating small changes in $M_1$ and $M_2$ through the calculation process. This equation follows from a standard formula for calculating the standard deviation of summed variables [53], assuming that the variables are uncorrelated and have Gaussian distributions:

$$\sigma_f{}^2 = \sum_i \left( \frac{\partial f}{\partial x_i} \right)^2 \sigma_{x_i}{}^2 \qquad \textbf{Eqn. 22}$$

where f is a function of $x_i$.


There are small additional uncertainties introduced by the spline fits and interpolation fitting techniques, however, these uncertainties are negligible (for all practical purposes) compared to the uncertainties from the counting statistics etc. and are therefore ignored in the uncertainty determination process at this stage. This issue is discussed in section 3.8.2.

## 3.8    Effects of Data Fitting Techniques

The first generation Pu SAC algorithm made use of a number of fitting techniques which could be replaced or improved. These are:

- straight line fits between the points on the $M_1$:$M_T$ pairs

- least squares fits beyond the modelled 3D surface

- polynomial or spline fits to the modelled data

These fitting mechanisms are studied in brief in the following sections.

### 3.8.1  $M_T$:$M_1$ Pair Fitting and Fitting Beyond the 3D Surface

In the Pu SAC algorithm, the $M_T$:$M_1$ pair fitting has been performed on the basis that the curve between two adjacent points may be approximated to a straight line. This assumption performs well in most cases where there are numerous points or the gradient is small. However, there may be cases where the data points do not behave predictably due to other fitting techniques used earlier in the modelling process (for example see section 3.8.2) and a cluster may move so that a straight line fit between adjacent points is no longer a good estimation, hence other types for fits may be used to best fit the data.

When a scenario is encountered where the data point would lie beyond the 3D surface, a straight line fit between the nearest four points is used to extrapolate out to the required $M_1$. This method performs well for larger $M_1$ values where there are a large number of data points, however it may introduce significant errors in the lower $M_1$ region, particularly for high mass samples. An example of such a scenario is shown in Figure 32. Due to the clusters of data points and uncertainties that could be introduced from inaccurate modelled data fitting, particularly for higher mass extrapolation, it may be more beneficial to use a curve which represents the trend of the whole set of $M_T$:$M_1$ pairs.
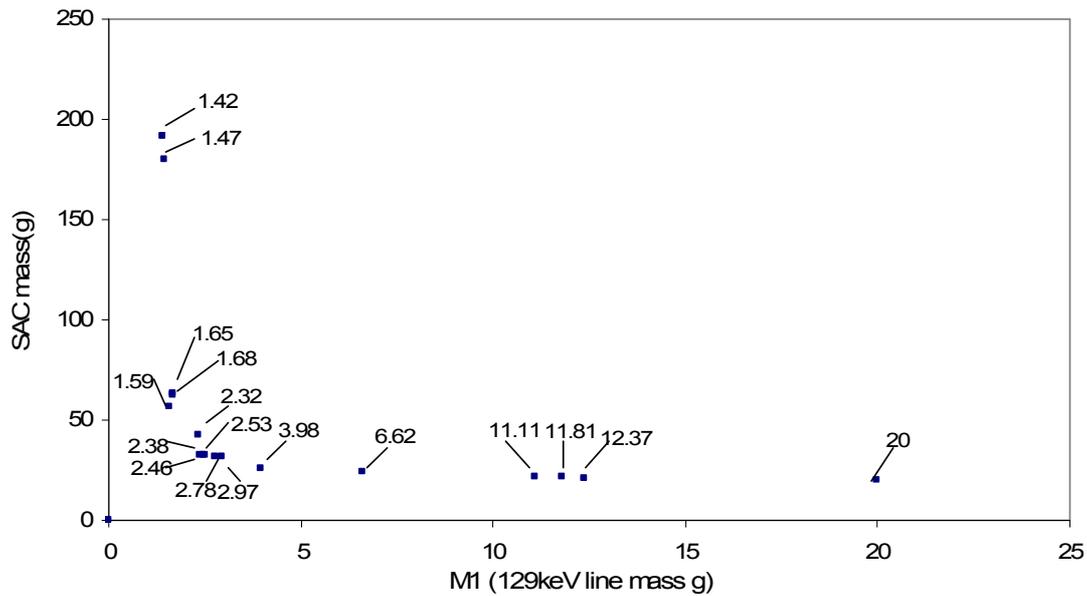
**Figure 32: An example of $M_T$:$M_1$ pairs for $M_2$=20g.**

An attempt to find a correlation between the coefficients of curve fit equations for $M_T$:$M_1$ pairs by plotting the curves for a number of inputted $M_2$ masses and observing the curve coefficients has been made. This could allow the $M_T$:$M_1$ curve coefficients to be calculated within the program algorithm so that no straight line (or other curve) estimations need to be performed by the program. However, the results of preliminary analyses show that the coefficients behave unpredictably and so this would not be possible. Therefore, the algorithm may need to perform an *ad hoc* curve fit.

A number of different methods have been compared in a study to determine the best $M_T$:$M_1$ curve fit technique both within and just outside the 3D surface. These are:

    (1)    a cubic spline method, using the final spline to extend beyond the 3D curve

    (2)    a straight line fit between adjacent points within the 3D surface and a least squares fit between the 4 end points outside the surface (used in the original Pu SAC algorithm)

    (3)    an exponential fit to the nearest 4 data points to the required $M_1$

    (4)    an exponential fit to the nearest 6 data points

    (5)    a power law fit to the nearest 4 data points

These 5 methods have been applied for 10 different examples across the range of masses using data modelled for the 1.5 cm cylinder ($\rho$=10 g.ml$^{-3}$), 1cm plate ($\rho$=12 g.ml$^{-3}$) and 2.5 cm plate ($\rho$=2 g.ml$^{-3}$). The ratio of calculated to true mass has been compared across the dataset to observe the average ratio and the standard deviation of the data. The results are displayed in Table 6.

**Table 6: Results of $M_T$:$M_1$ pair fits using the five investigated methods.**

| Method | cubic spline[1] | straight line[2] | four-point exponential[3] | six-point exponential[4] | four-point power law[5] |
|---|---|---|---|---|---|
| Average ratio | 0.14 | 1.17 | 1.17 | 1.10 | 1.16 |
| Standard Deviation | 2.52 | 0.19 | 0.31 | 0.24 | 0.30 |

The cubic spline method shows a large spread in results since the fluctuation in position of data points does not behave similarly to cubic equations locally within the constraints (the curve and first derivative must be continuous) and so the algorithm produces widely varying results. The remaining four methods are not constrained in such a way and act as best fit approximations. Each of these methods performs similarly well over the range of data, however the straight line fit produces the smallest spread of results.

Outside the 3D surface each method may suffer since the curves are extrapolated out to the required $M_1$, highlighting any inconsistencies between fitting methods and the true curve shape. Ideally each $M_T$:$M_1$ dataset could be fit to a single curve type for the whole range of lump sizes, however this is not the case since the curves vary too much across the mass range and are not well conditioned. Also since the modelled 3D surface should cover almost all lump shape and density possibilities from the most to least attenuating, any instances of data beyond the 3D surface should be due to counting statistics, matrix corrections, or other small uncertainties and corrections in the inputted 129 keV and 414 keV apparent masses, resulting in minimal deviations from the 3D surface. Consequently a straight line extrapolation from the nearest 4 points should provide a good estimation of the true mass without increasing the complexity of the algorithm. If, however, the Pu SAC method were to be used in a user-driven (as opposed to a fully automated) analysis of the data, a more accurate result could be obtained by fitting the $M_1$:$M_T$ dataset to an appropriate curve.

### 3.8.2 Modelled Data Fitting

The first generation Pu SAC algorithm used $6^{th}$ order log polynomial curves to fit the modelled data in order for the curves to be reproduced in the Delphi program. This fitting technique had originally been used since the trend lines were able to sufficiently fit the data over the mass range with the tools provided (Borland$^{TM}$ Delphi and Microsoft$^{TM}$ Excel) for the purpose of demonstrating the feasibility of the technique. However, other types of curves have been shown to fit the data more accurately, and are consequently used in the resulting engine, as demonstrated in the following sections.


### 3.8.2.1 Polynomial Fits

The original Pu SAC algorithm that was developed used $6^{th}$ order log polynomials to fit the modelled data instead of the cubic splines method currently used. The values of $M_1$ and $M_T$ at each inputted mass have been compared to the original modelled data to illustrate the accuracy of these $6^{th}$ order log polynomial curves. Although the majority of the curves show errors of less than 1%, some curves such as the rods and flat plates which are more difficult to fit, show errors of up to 11% for $M_T$ and the rods up to 22% for $M_1$. Note that the 0.3x0.3cm Pu flat plate and the Pu and PuF$_3$ 3x3cm flat plates were omitted from the first generation algorithm since their curves fits using this method were not accurate and introduced additional uncertainties.

It was observed that the curves do not fit the data well over the entire range and so the data were been split into two sets for the lower (0.0001 g-50 g) and higher (50 g-350 g) masses to allow the curves to be fitted more easily. Each half has been fitted to obtain equations for $M_T(M_2)$ and $M_1(M_2)$ and the errors have been determined.

An alternative method to improve the fits would be to use a different order of polynomial. The $6^{th}$ order log polynomial, which fits the majority of the data relatively accurately, could be increased to a higher order log polynomial, for example a $10^{th}$ order log polynomial. This has been performed using Oakdale Engineering's Datafit$^{TM}$ program [54].

The 3x3 cm Pu flat plate and 10 cm $PuO_2$ rods have been selected to demonstrate different fitting techniques since these curves represent the largest errors for $M_T$ and $M_1$ respectively.

**Table 7: Summary of errors for sample modelled data fits.**

| Method | 3x3 cm Pu flat plate | | | | 10 cm $PuO_2$ rod | | | |
|---|---|---|---|---|---|---|---|---|
| | Avg $M_T$ error % | Max $M_T$ error % | Avg $M_1$ error % | Max $M_1$ error % | Avg $M_T$ error % | Max $M_T$ error % | Avg $M_1$ error % | Max $M_1$ error % |
| $6^{th}$ order log polynomial | 4.12 | 11.20 | 0.67 | 2.93 | 0.40 | 2.09 | 3.88 | 22.10 |
| Dual $6^{th}$ order log polynomials | 0.17 | 0.82 | 0.21 | 2.93 | 0.32 | 1.99 | 2.39 | 16.77 |
| $10^{th}$ order log polynomial | 1.55 | 3.97 | 0.52 | 1.24 | 0.24 | 1.23 | 2.90 | 13.59 |
| Dual $10^{th}$ order log polynomials | 0.15 | 0.82 | 0.06 | 0.32 | 0.20 | 0.97 | 2.23 | 10.41 |

The results for the original and different fit techniques described above are summarised in Table 7 in the first three rows. The effect of splitting the curve in half evidently improves the data fit to some extent. It may be possible to split the data sets into numerous curve fits to reduce the fitting errors further, however this would increase the complexity of the program algorithm.

Each technique reduces the errors in the fitted data, however the dual fit is better for the 3x3 Pu flat plate whereas the $10^{th}$ order log polynomial produces the better fit for the 10 cm $PuO_2$ rod. These two methods have been combined so that the data are fitted with two higher order log polynomials. $10^{th}$ order polynomials were not always possible due to the there not being enough data points to fit in each half, and so the largest order polynomial is used in each case. The results are listed in the last row of Table 7, showing an improvement from the original $6^{th}$ order polynomial fits.

Although the above polynomial fitting methods reduce the errors at each point, it is possible to use an alternative fitting technique so that this error becomes zero, such as a cubic spline fitting method. This alternative shall now be considered.

## 3.8.2.2 Cubic Spline Fits

A cubic spline interpolation uses a continuous, smooth piecewise curve between the data points using separate third-order polynomial fits for each section. One condition of the function is that it will interpolate all entered data points so there will be no error from the original data, unlike the polynomial fitting method. The cubic spline method fits the data points but in between there will still be an interpolation error. This has been tested below.

A program has been written in Delphi[TM] to create a cubic spline fit for n data points and evaluate the y-value of any given x-co-ordinate within the range of inputted x-co-ordinates. This program has been based upon a method used in J. Wood's "Computational Methods in Reactor Shielding" [51]. The spline algorithm has been implemented within the Pu SAC program, replacing the polynomial fit method, and tested using the following three lump types over the mass range 0.0001 g-350 g:

- 1.5 cm high cylinder with a Pu density of 10 $g.cm^{-3}$
- 1 cm high plate with a Pu density of 12 $g.cm^{-3}$
- 2.5 cm high plate with a $PuO_2$ density of 2 $g.cm^{-3}$

The spline technique demonstrates an overall improvement from the polynomial methods in the intermediate and high-mass regions. The results are illustrated in Figure 34.

## 3.9 Modelled Results

The developed Pu SAC method (using cubic spline fitting) has been compared to the basic 2-line and 3-line (unconstrained) Fleissner SAC methods in Figure 33 by inputting the original modelled data (from which the algorithm was created) for a mass range of 1 mg to 250 g, the upper value of which can be considered to be an extreme range for a single lump in most waste assay scenarios. The new engine for this data provides a SAC mass which is much closer to the true mass than the Fleissner techniques, excepting the final 350 g points where the ratio of corrected to true mass is significantly low/high.
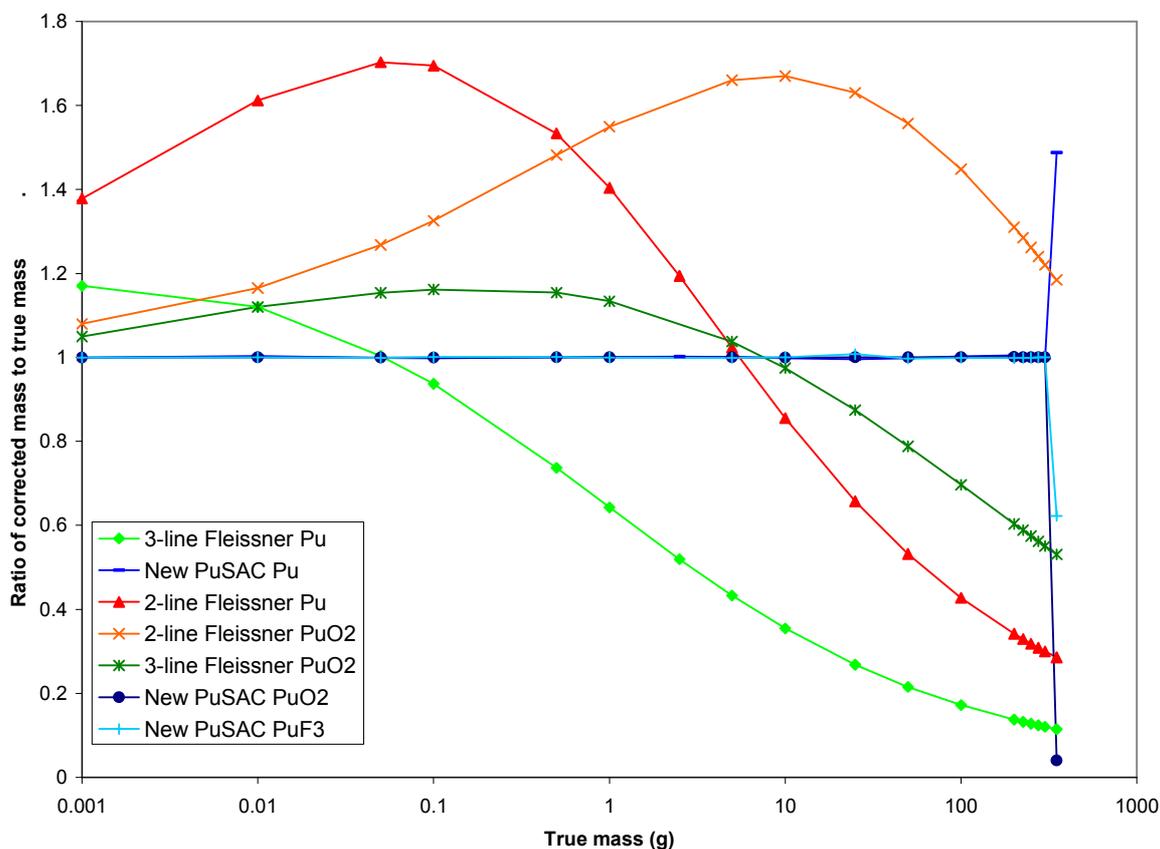


**Figure 33: Comparison between the Fleissner SAC method and the new SAC algorithm results.**

At 350 g the lump has become highly attenuating. In fact, the modelled data produces a point on the $M_1$:$M_T$ graph that is beyond the most attenuated modelled point i.e. a co-ordinate outside the

limits of the 3D surface. Consequently the algorithm uses a linear least squares fit of the nearest (most attenuated) four modelled points and extrapolates to the inputted $M_1$. The fitting technique has been investigated in more detail in Section 3.8.1.

The above comparison is unrealistic because it re-uses the data that originally created the numerical model resulting in 'incestuously' over-optimistic results, where each $M_2$ will lie exactly at a modelled point, and will create a set of $M_1$:$M_T$ pairs that all lie exactly on or very close to modelled data points. Consequently the effects of using $6^{th}$ order log polynomials as trend lines and using the straight line fit between $M_1$:$M_T$ pairs is not tested sufficiently.

Consequently, the algorithm has also been tested with modelled data from three new lump types that were not used as input for the curves in the new algorithm. These are:

- 1.5cm high cylinder with a Pu density of 10 g.cm$^{-3}$
- 1cm high plate with a Pu density of 12 g.cm$^{-3}$
- 2.5cm high cylinder with a PuO$_2$ density of 2 g.cm$^{-3}$

The lumps have been modelled with a mass range of 0.1 mg to 350 g and are compared to the basic 2-line Fleissner method, along with the $6^{th}$ order log polynomial result, as described in section 3.8.2.1 (see Figure 34).
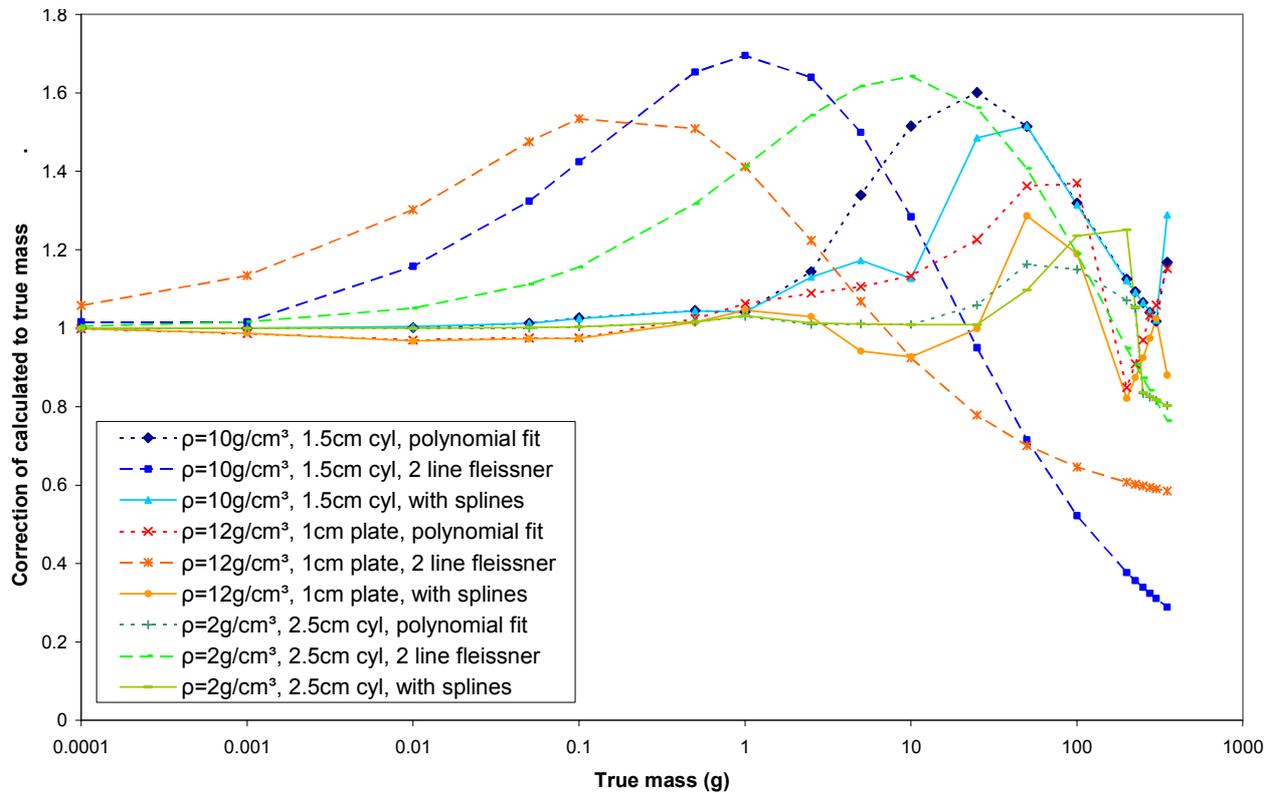
**Figure 34: Graph showing the calculated to true mass ratio comparison using the polynomial and spline Pu SAC, and the 2-line Fleissner methods for new modelled lumps.**

Figure 34 shows that the spline method fits equally as well as the 6th order log polynomial method at the lower (up to 1 g) and higher (above 100 g) mass regions, but performs better than the polynomial method in the intermediate region (between 1 and 50-100 g). The spline method has shown an improvement to the first generation (polynomial fit) Pu SAC algorithm in the intermediate region, however the lack of improvement in the higher mass region is due to the modelled data points themselves rather than their fitting technique. The high mass data used in Figure 34 are for greatly attenuating lumps that are located within the clustered region of the $(M_1:M_2:M_T)$ 3D surface. Within this region the lumps begin to saturate (only the surface of the lump is detected- the apparent mass is proportional to the projected area) and the surface effects of the sample (which vary with the shape of the lump) dominate. Consequently the 3D surface appears less well behaved since the points to not lie on smooth constant true mass curves and the Pu SAC algorithm becomes limited (see section 3.10).

The new PuSAC engine with splines demonstrates much improved results (i.e. the ratio of corrected to true is closer to unity) than the 2-line Fleissner method for lumps up to 5 g, but larger lumps drift up to a ratio = 1.3 line whereas the Fleissner method begins to underestimate. On comparison of the data and Figure 28, the Pu SAC algorithm produces less correct results in the regions of high attenuation, where the data points appear to be denser. This region of the graph (the most attenuating region) will suffer from worse errors than the less attenuating side of the 3D surface since the lines of constant $M_T$ are much more compact and the $M_1$:$M_T$ graph becomes very steep, hence a small change in any of the input parameters will result in a large change in calculated $M_T$.

It can be appreciated that at low masses the counting precision may be limiting but that the corrections are relatively small. As noted above the 414keV apparent mass may be an adequate default value for the true mass. At high masses on the other hand the lump may be close to saturation, meaning that only the surface regions are viewed and that a large fraction of the mass plays little part in the measurement. In this case the statistical accuracy may appear to be much better, but by the same token the demands on the data to distinguish different massed bodies based on small fractional changes in size is also increased.

The UK ILW/LLW Pu limit for a 60 kg gross weight drum (~40 kg net weight) is in the range of 50-90 mg depending on the isotopics and the new SAC technique is seen to work accurately without over-reporting in this range which will significantly improve sentencing. The fluctuations at higher masses are discussed more fully in section 3.10.

## 3.10 PuSAC Limitations, the Number of Modelled Points & the High Attenuation Region

The number of lumps and densities used for the algorithm has been limited purely by the capabilities of the point source model and CPU time. The original Pu SAC algorithm has been modelled using 7 different shapes and up to 3 densities, resulting in 19 separate lump/density combinations. Also, a number of these lumps were subject to limitations caused by the minimum input lump dimensions in the point source model and the maximum size of the lump dimensions in terms of its view from the modelled detector. Consequently some shapes do not have modelled data points across the whole range of masses; although the available lump data have proved satisfactory to demonstrate the Pu SAC method.

The number of data points could be increased by introducing intermediate densities or different shaped lumps if required. This would improve the final true mass result by increasing the number of data points available to perform the $M_1:M_T$ curve interpolation and extrapolation. In the low attenuation region an increase in the number of points would have less of an effect since the results follow a well-conditioned shallow curve, where a small change in $M_1$ creates a relatively small change in $M_T$. However in the more attenuating region a larger number of data points would be more beneficial since the data are more erratic.

Where the apparent $M_1$ lies outside the 3D surface the extrapolated true mass could also be improved. An example is shown in Figure 35 for an $M_2$ of 3 g. The red points are the original modelled data used for the Pu SAC analysis in the previous sections. The blue points are the three additional lump types modelled to test the Pu SAC algorithm. The two lines (dotted and dashed) show the projected straight line fits between the end 4 points that would be used for an extrapolation with and without the additional lump data. For an $M_1$ just 0.1 g outside the 3D surface in this case the additional data would change the resulting $M_T$ by 1.5 g.
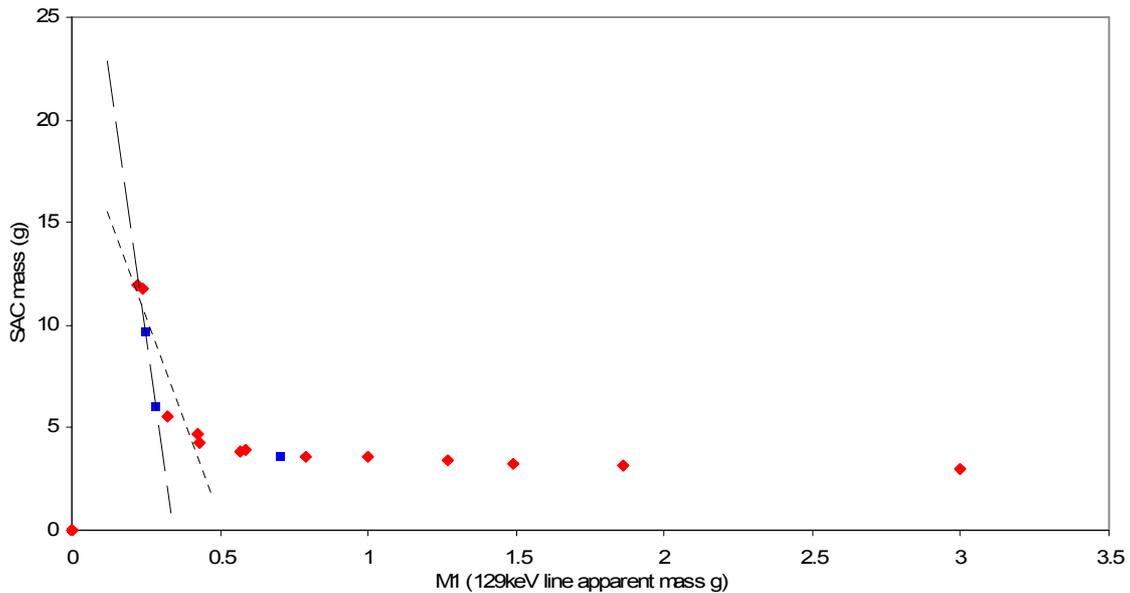
**Figure 35: $M_1$:$M_T$ curve for $M_2$=3g with additional data to demonstrate the effect of the number of modelled data points.**

One disadvantage of greatly increasing the number of modelled points is that if the points were to cluster very close together in the high attenuation region the straight line fit for extrapolation could become a representation of the four data points locally, rather than providing a suitable approximation for high attenuation end of the curve. In this case the least squares fit should be calculated from a larger number of data points.

### 3.10.1 Material and Shape Dependence

As previously stated, in the high mass area the data seem less well behaved. This may be because as the lumps saturate they behave differently for different shapes and material types. A simple study has been performed to test this using non-rotating cubes and cuboidal flat plates (with side length ratios x, 10x and 15x, with the 10x dimension leading away from the detector). Using a far field approximation the two apparent 129 keV and 414 keV masses for both shapes have been determined by integration over the sample. This has been performed using the SAF as the ratio of the number of gamma rays detected with an absorber to the number detected without an absorber present i.e. for a cuboidal lump viewed in the far field perpendicular to the surface:

$$SAF = \frac{N_{withAbs}}{N_{\mu=0}} = \frac{\int\limits_{0}^{x} A\upsilon e^{-\rho\mu x}dx}{A\upsilon x}$$

$$= \frac{\left(1 - e^{-\mu\rho x}\right)}{\mu\rho x}$$

<div align="right">**Eqn. 23**</div>

where $\upsilon$ is the specific activity of the sample, N is the number of gamma rays detected, $\rho$ is the density of the sample, $\mu$ is the attenuation coefficient and A is the area of the face of the shape normal to the observer. This has been performed for a range of densities for the three materials: Pu, $PuO_2$ and $PuF_3$. The results have shown that a 3D surface containing data for one lump shape but all material types suffers from the same effects in the high attenuation region. However, if data are modelled for a single shape and material type for a large range of densities the results follow well conditioned curves in all regions of the 3D surface.

The data for Pu cubes for a range of densities (0.5-19.8 $g/cm^3$) and masses (0.0001-350 g) have been calculated and used as the basis of a test Pu SAC algorithm using cubic spline $M_1:M_2$ and $M_T,M_2$ fits and straight line interpolation between adjacent points on the $M_1:M_T$ curve.

A range of masses between inputted data points for Pu cubes have been input into this test algorithm. The results for Pu cubes for a density of 5 $g/cm^3$ (used as input for the model) performs very well with corrected to true mass ratios between 1.005 and 0.999. A density of 12 $g/cm^3$ also performs well with a slowly increasing ratio until a maximum of 1.16 at higher masses. The largest tested true mass was 333 g which gave the minimum ratio of 0.84 since the data were outside the surface.

$PuO_2$ cubes were also tested using the Pu cube $M_1:M_T:M_2$ data. The results were that the SAC masses were always less than the true masses, with deviations increasing with true mass until ratios of 0.662 for 5 $g/cm^3$ and 0.409 for 12 $g/cm^3$. This is because the apparent 129 keV and 414 keV masses were for $PuO_2$ (rather than Pu metal as the model expects). The $PuO_2$ has a lower mass attenuation coefficient $\mu$ and is less attenuating; consequently the apparent masses for the 129 keV line are relatively higher, causing a lower true mass than would be determined from an algorithm designed for the correct material type.

From this study it can be seen that the Pu self-absorption correction may be improved if more information is known about the Pu being assayed e.g. its composition and shape; however this is not readily available in nuclear waste assay. The correction may be refined however if limited information is available. For example, if the material is one of only a few possible types, an engine could be created with the appropriate data and a result obtained for each material type, using the difference in results to obtain an improved uncertainty calculation.

## 3.11 Extension to Multiple Lumps using Modelled Data

Due to the high degree of non-linearity observed in the model, the combination of the apparent masses from a series of smaller lumps was expected to produce a smaller self attenuation factor than that expected for a single large lump of equal true mass. Therefore the model was expected to underestimate the total Pu in the combined-lump sample.

The apparent 129 keV and 414 keV masses for a number of material/shape combinations were summed and used as input for the algorithm to see how it would behave for multiple lumps. These combinations include several lumps of the same material and shape, plus random mixed numbers and types of lumps selected from the range of masses, shapes and material types studied in the Pu SAC algorithm development, plus a series of newly modelled data sets for 1.5 cm high cylinders with a Pu density of 10 g.cm$^{-3}$ and 2.5 cm high cylinders with a PuO$_2$ density of 2 g.cm$^{-3}$. The results are presented in Figure 36 in a plot of the corrected to true mass ratio versus the apparent 414 keV mass of the lump combination.
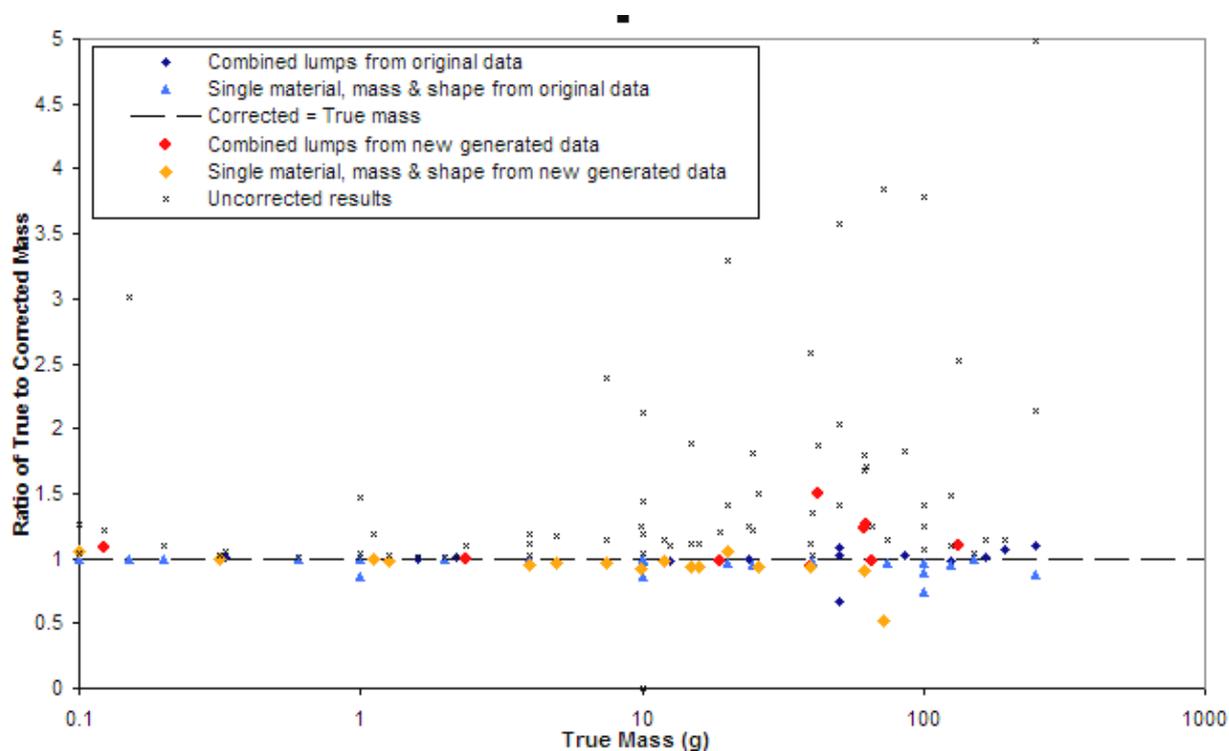


**Figure 36: Plot of the ratio of true to corrected mass versus the total true mass for random combinations of lumps collated from independently-treated single lump modelled data.**

The uncorrected 414 keV apparent masses are also plotted as a comparison. The results do not produce perfect ratios of one, as expected, because as the individual lumps are combined their total 129 keV apparent mass will be higher than that of a single lump of equivalent mass, whereas the 414 keV apparent mass will remain relatively similar. Consequently the corrected mass of the combination of lumps is underestimated, demonstrated by approximately 80% of the Pu SAC corrected data points in Figure 36. The remaining corrected masses lie above the line where the ratio equals one. This is due to fluctuations in the data points in the high attenuation region of the $M_1$:$M_2$:$M_T$ plot.

It should be noted that these lump combinations have been performed by summing the apparent masses of individual lumps, assuming that all lumps are independent and the gamma rays from each lump are not attenuated by any other lump on their path to the detector. However this may not be the case in real waste drums and the resulting apparent mass may be attenuated more than for the examples shown above.

As shown, the method appears to work well for multiple lumps of various compositions. All of the modelled results are within 50% of the corrected equal to true mass line, with 64.3% of the modelled results achieving values within 5% of the true mass. These observations could be developed with a more detailed study to implement a contribution to the Total Measurement Uncertainty (TMU) of the sample from the Pu self-absorption in the case of multiple lumps. For example, if a 1 sigma uncertainty is required by the user (68% of the results should lie within the area if a Gaussian distribution is used, for example), this equates to a 6% uncertainty if the uncertainty is assumed to be constant across the mass range.

It may also be observed that the variation from the corrected equal to true mass line appears to increase with increasing true mass and so the TMU contribution from multiple lumps could be refined to be a function of the apparent mass with a more in-depth study.

## 3.12 Comparison to other Pu SAC techniques for Modelled Data

The new Pu SAC method has been compared to uncorrected results and the 2-line Fleissner method in section 3.9. This section extends the comparison to other Pu SAC techniques, such as the 3-line Fleissner method with unconstrained parameters and infinite energy extrapolation method using both linear and $2^{nd}$ order polynomial fits for three lump types:

- Set 1: 1.5 cm high cylinder with a Pu density of 10 g.cm$^{-3}$
- Set 2: 1 cm high plate with a Pu density of 12 g.cm$^{-3}$
- Set 3: 2.5 cm high cylinder with a PuO$_2$ density of 2 g.cm$^{-3}$

The results are displayed in Figure 37 along with the uncorrected 414 keV line apparent mass.
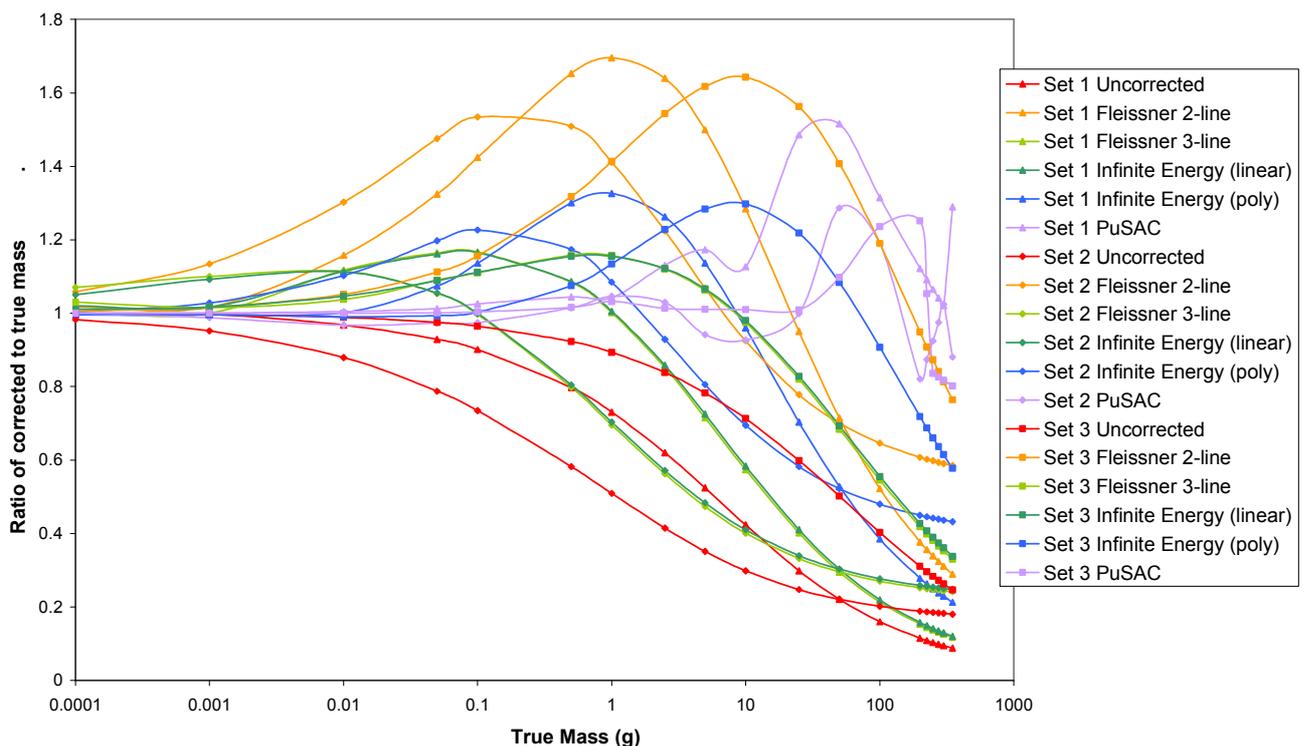


**Figure 37: A graph showing the ratio of modelled corrected to true mass for three new lump shapes and materials using the 2-line Fleissner and unconstrained 3-line Fleissner methods, the Pu SAC method plus the Infinite Energy method using linear and polynomial fits.**

As noted previously, the Fleissner methods overestimate at intermediate masses and underestimate at higher masses. The linear Infinite Energy Extrapolation methods follow the same curve as the 3-line Fleissner method, whereas the $2^{nd}$ order polynomial fit to the Infinite Energy Extrapolation method follows a similar pattern to the 2-line Fleissner method but to a lesser extent, offering an improved performance at intermediate masses (with a maximum over-correction of 1.2) but a similar under-correction at higher masses. For the selection of lumps studied above the Pu SAC method shows a clear improvement compared to the other methods across the whole mass range despite the fluctuations at the higher masses (as discussed in section 3.10).

## 3.13  Comparison to other Pu SAC techniques for Measured Data

The new Pu SAC method has been compared to the other Pu SAC techniques, such as the 3-line Fleissner method with unconstrained parameters and infinite energy extrapolation method using both linear and $2^{nd}$ order polynomial fits for the AE4043/nn sources measured on the bench in two different orientations. The experiment was set-up using single 70mm diameter by 20mm thick BEGe3820 detector, as described in section 3.3.1. The sources have been measured twice for two different orientations with the source positioned upright (two sets of measurements) and laid horizontally inside the Pb shield, resulting in 4 measurements for each source, as shown in Figure 11.

The raw apparent mass results of these measurements could not be used as a fair representation of the SAC methods since the sources are encapsulated within 2.5 mm of stainless steel. Therefore a correction factor has been introduced to account for the encapsulation. This correction factor has been calculated by modelling the sources in the two orientations for each required energy, and using the ratio of the countrate observed with and without the encapsulation. The XCOM μ with coherent scattering has been used in the ratio calculation, as discussed in section 3.3.4. Due to the limitation of the model the horizontal orientation sources have been modelled as cuboidal sources, of equal mass and surface area perpendicular to the detector as the source itself, contained inside a 2.5 mm stainless steel encapsulation. The upright orientation correction factor has been modelled using the set-up described in section 3.3.4.

The measured results after taking account of the encapsulation are displayed in Figure 38 along with approximate uncertainties and polynomial trend lines for the datasets.
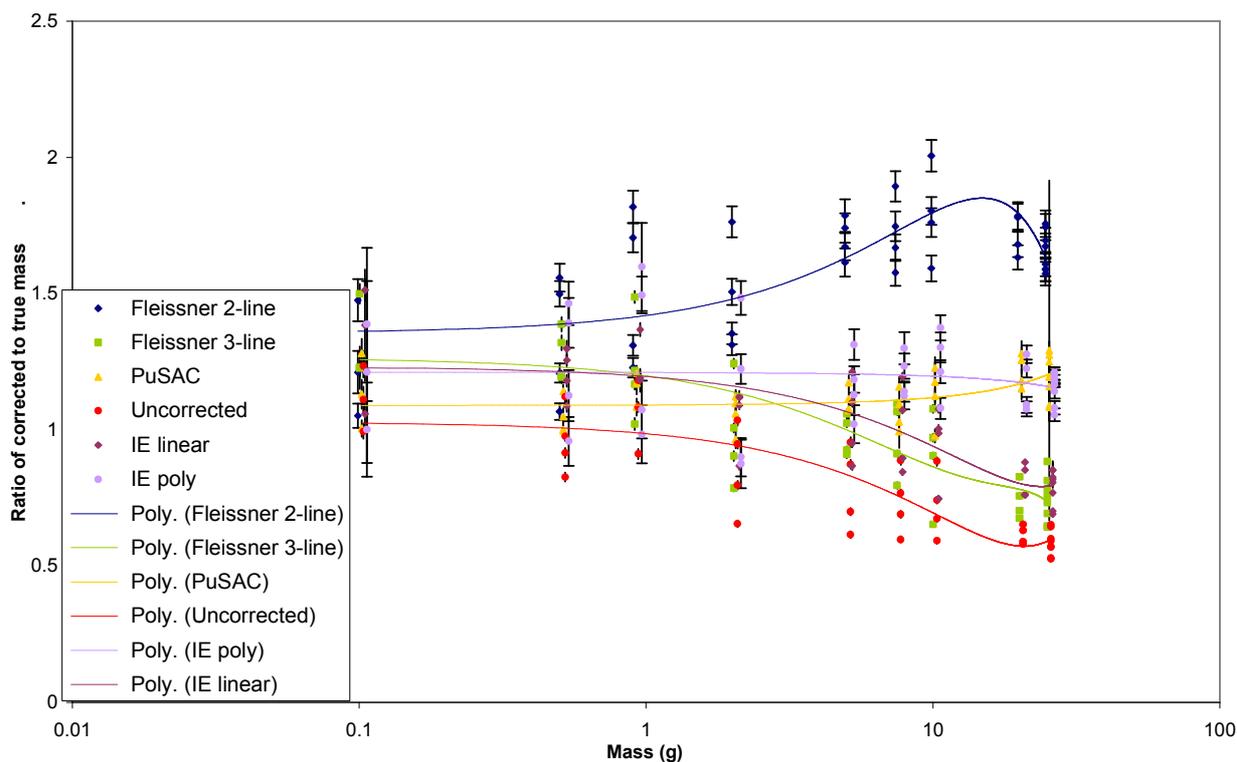
**Figure 38: A graph showing the ratio of modelled corrected to true mass the AE4043/nn sources measured in 2 orientations using the 2-line Fleissner and unconstrained 3-line Fleissner methods, the Pu SAC method plus the Infinite Energy method using linear and polynomial fits.**

The graph shows the general trend of the corrected Pu mass results in relation to the true unencapsulated mass of the sample. The 2-line Fleissner method has been found to be the least satisfactory across the range of masses, increasing to a maximum of 100% overcorrection at higher masses. The 3-line Fleissner and infinite energy extrapolation with a line fit both overcorrect slightly up to a mass of around 5 g then begin to underestimate the true mass.

The infinite energy extrapolation method with a 2nd order polynomial fit and the new Pu SAC technique both perform very well, with a slight overcorrection across the range of masses, but greatly improving the result compared to the uncorrected 414 keV apparent mass. The results from these two methods are displayed separately in Figure 39.
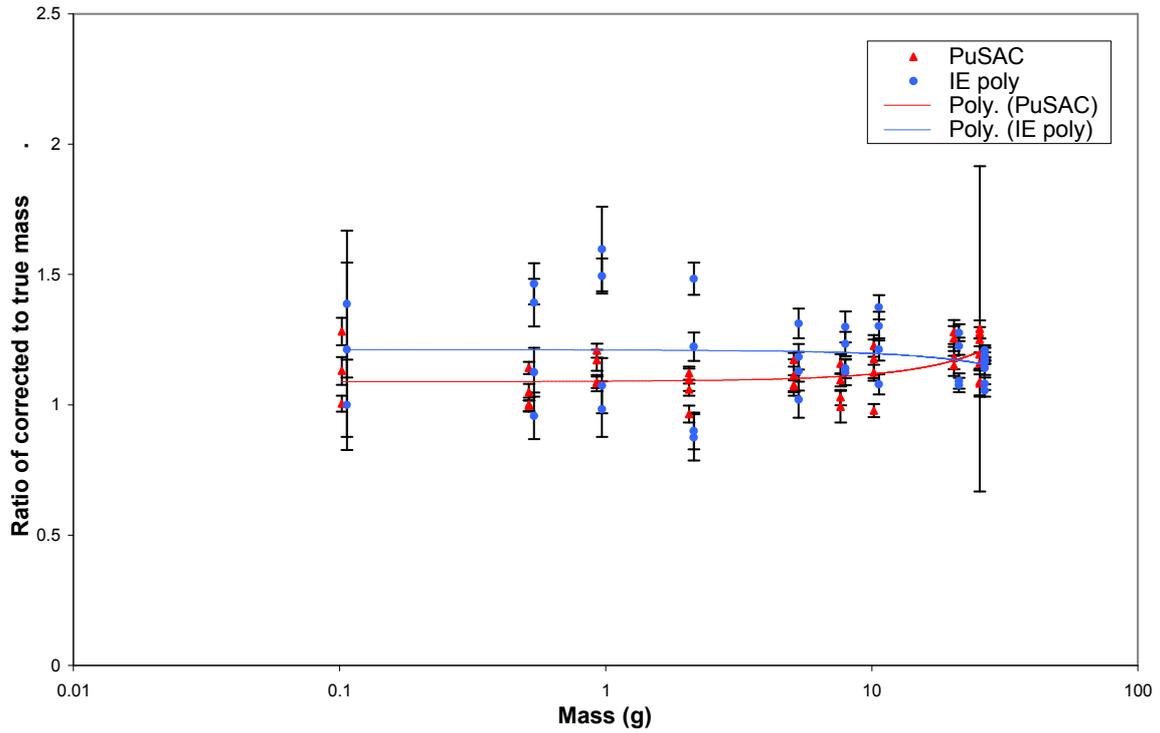
**Figure 39: A graph showing the corrected to true mass ratio for the measured AE4043/nn sources for the new Pu SAC and infinite energy extrapolation the 2$^{nd}$ order polynomial fit methods.**

Figure 39 shows that on closer inspection the infinite energy method, although demonstrating a good average result, varies to a maximum overcorrection of 1.6, whereas the new Pu SAC technique shows much less variation. The large uncertainty for the new Pu SAC AE4043/10 source result is due to the distribution of modelled data points in the high mass region of the $M_1$:$M_2$:$M_T$ surface causing a small change in input apparent masses to result in a large change in SAC corrected mass.

# 4 URANIUM SELF ABSORPTION

## 4.1 Introduction

Although a significant amount of work has been performed on self-absorption of fissile materials (see Section 3.1), in particular for Pu, a standard correction technique for U SAC has not yet been developed. Recent work by Croft et al. [41] and Hansen [55] emphasise the interest in this problem and suggest that methods of U SAC are currently being investigated e.g. by comparing the closely-spaced X-ray lines from thorium and uranium. If the sample may be identified as being between the extremes of 'dilute' or infinitely thick ([56], [57]) then it may be possible to apply a simplified correction. Methods have been proposed for 'infinitely thick' samples where the enrichment is known [56] using the 186 keV and 98.4 keV X-ray from fluorescence activity. However the required spectral region is complex and the peaks can be difficult to resolve. Alternatively, a pre-determined self-absorption factor (SAF) may be applied in order to obtain a compensated assay value if all the material is assumed to be in a single lump. If the material is found to be 'dilute' from observations of the differential absorption for low energy $^{235}$U lines peak ratios (demonstrated by Rackham *et al.* [57]) the SAF could be removed to avoid over-estimation of U. This method has only been demonstrated for small ideal waste packets and the 143 keV, 163 keV and 205 keV lines may suffer from interference if Pu is also present in the sample.

Another possible method is to use the Infinite Energy Extrapolation (IEE) method [44], or a variation of it. The apparent assay mass is plotted against the reciprocal of the energy, say, and extrapolated to non absorbing conditions. This is taken as 'infinite energy' on the basis that generally in the energy range of interest mass attenuation coefficients are falling rapidly with energy. This approach has been successful for Pu since $^{239}$Pu emits a number of lines of known abundance and which are reasonably well spaced in energy. This may be adapted to use the 143.8 keV, 163.3 keV, 185.7 keV and 205.3 keV lines from $^{235}$U, however these lines are comparatively close together and do not offer as much differential absorption (sensitivity to lump size) as experienced by the 129 keV and 414 keV lines from $^{239}$Pu. Also, if Pu is present in the drum three of the lines would experience interference from Pu peaks (at 143.4 keV, 144.2 keV, 146.1 keV, 161.5 keV, 203.6 keV). The IEE method has been used as a comparison to the developed U SAC method in section 4.6.

An alternative to estimating and applying a SAC from the measurement data to be applied to the particular assay could be to simply introduce an additional uncertainty component [43], a "lump" parameter for example, that may be incorporated into the Total Measurement Uncertainty (TMU) associated with the measurement to account for the case where all the U in an item is concentrated into a single spherical (worst case) lump, depending on what may be known about the origin of the item. In so doing the assay value can be bounded in a way that may satisfy certain safety and transport criteria, but as a quantification approach it does not represent the best estimate (see section 5.4).

This chapter attempts to extend the numerical method for plutonium self-absorption described in Section 3.7 to apply to the case of uranium where the enrichment is known or at least falls into classes or bands. If only a limited number of possible enrichment types may be present within a waste stream and only one type is present in any given drum, then it has been demonstrated that the uncorrected characteristic lines may be used to determine which enrichment is present. This is possible if the source of the waste is known (e.g. from records or knowledge of the facility) sufficiently well, however in principle the enrichment could be any value. Once the enrichment has been established the two-line SAC method developed for $^{239}$Pu may be applied using the 186 keV and 1001 keV lines, as explained below.

A program has been created in Delphi$^{TM}$ to test a new U SAC method based upon the assumption that a waste stream contains only three possible enrichment categories (see section 4.3). It has then been extended to perform with any known enrichment (section 4.5), which must be known either from details of the waste stream's origin or using relative isotopic spectral analysis codes such as employed in FRAM ([58], [59], [60]) or MGAU [61].

## 4.2   U Self-Absorption Analysis

### 4.2.1  Uranium lines

Two main lines are used to measure uranium: the 186 keV line from $^{235}$U and the 1001 keV line from $^{238}$U (produced from the decay of $^{234}$Pa$_m$ as a second daughter of $^{238}$U if in equilibrium,

which should always be the case for waste measurements). Although there are other $^{235}$U lines available to measure U (143.8 keV, 163.3 keV and 205.3 kev), the 186 keV line is the most prominent of the set close to the U K-edge (115.6 keV) and offers good differential absorption.

## 4.2.2 Enrichment Categories

It shall be assumed for test purposes that there are only three possible enrichment categories within waste drums. Although this assumption is not correct the analysis, modelling and correction may be performed for any U enrichment value, and three commonly-used enrichments have been chosen as a demonstration of the way enrichments can be estimated from apparent enrichments and consequently a U SAC performed. The three chosen enrichment types for the purpose of the investigation are:

- Depleted uranium (DU)             0.5% $^{235}$U
- Intermediate enrichment uranium (IEU)     40% $^{235}$U
- High enrichment uranium (HEU)         93% $^{235}$U

It is also assumed that each drum may only contain one enrichment type at a time.

## 4.2.3 Enrichment Determination

The apparent enrichment may be calculated as:

$$Enrich(\%) = \frac{m_{U235}(g)}{m_{U235} + m_{U238}(g)} \times 100 \qquad \textbf{Eqn. 24}$$

where $m_{U235}$ is the apparent mass of $^{235}$U from the 186 keV line and $m_{U238}$ is the apparent mass of $^{238}$U from the 1001 keV line. Due to self-absorption the apparent masses will always be less than the true mass and the less energetic line will always be affected more. Consequently the apparent enrichment should be less than the true enrichment (although this may not be the case due to low statistics) where self absorption is significant, and the apparent enrichment may be used to select an enrichment category, provided the regions on the apparent 186 keV mass versus apparent 1001 keV mass surface (see Figure 40) do not overlap for the different enrichments.

In practise the enrichment may be any value. If the enrichment may be determined via programs such as MGAU or FRAM then this value may be used as the true enrichment for the U SAC program.

## 4.2.4 U Lump Modelling

The self-absorption curves for U metal (of density 18.7 g.cm$^{-3}$) have been modelled to determine the SAF and hence apparent masses at the 186 keV and 1001 keV lines for the three possible enrichment types: DU, IEU and HEU. The uncorrected self-absorption behaviour of bare U lumps of various dimensions have been calculated using the point source model (see section 3.2), over the mass range of 0.1 mg to 350 g.

The apparent masses are determined by using the self-attenuation factor and known enrichment category so that:

$$M_{186} = k_{235}.SAF_{186}.M_T \quad \text{and} \quad M_{1001} = k_{238}.SAF_{1001}.M_T \qquad \textbf{Eqns. 25\&26}$$

where $M_{186}$ is the apparent mass at the 186 keV line energy, $M_{1001}$ is the apparent mass at the 1001 keV line energy, $SAF_{186}$ is the self attenuation factor at 186 keV, $SAF_{1001}$ is the self attenuation factor at 1001 keV, $M_T$ is the true mass of the modelled sample, $k_{235}$ is the fraction of $^{235}$U within the U sample, and $k_{238}$ is the fraction of $^{238}$U within the U sample.

The behaviour of the self-absorption has been calculated for the following geometries:

- Cylinders with diameter equal to height, with dimensions ranging from $2.0 \times 10^{-4}$ m to $2.9 \times 10^{-2}$ m
- Square-faced plates with a fixed depth of 1 mm, with heights ranging from $7.0 \times 10^{-5}$ m to $1.6 \times 10^{-3}$ m
- Rods with a fixed length of 0.1 m, with diameters ranging from $8.3 \times 10^{-6}$ m to $1.5 \times 10^{-2}$ m
- Cubes of side length ranging from $2.0 \times 10^{-4}$ m to $2.7 \times 10^{-2}$ m
- Plates of fixed square face length $3.0 \times 10^{-3}$ m, with heights ranging from $6.0 \times 10^{-7}$ m to $5.9 \times 10^{-3}$ m
- Plates of fixed square face length $3 \times 10^{-2}$ m, with heights ranging from $6.0 \times 10^{-7}$ m to $2.1 \times 10^{-2}$ m

- Plates of fixed square face length 0.1 m, with heights ranging from 5.0 $\times 10^{-7}$ m to 1.9$\times 10^{-3}$ m

- Plates of fixed square face length 7 $\times 10^{-2}$ m, with heights ranging from 5.0 $\times 10^{-7}$ m to 3.8$\times 10^{-3}$ m

- 6 cm high cylinders, with diameters ranging from 1.1 $\times 10^{-5}$ m to 2.0 $\times 10^{-2}$ m

- 1 cm high cylinders, with diameters ranging from 2.6 $\times 10^{-5}$ m to 4.9 $\times 10^{-2}$ m

- Square faced plates with a fixed depth of 1 mm, with heights ranging from 4.0 $\times 10^{-5}$ m to 7.9 $\times 10^{-2}$ m

- Zero attenuation geometry (186 keV mass = 1001 keV mass = true mass)

Figure 40 shows the relationship of apparent masses at 186 keV ($M_1$) and 1001 keV ($M_2$) and the true U mass ($M_T$) for the selection of shapes for three enrichment types, in the same way that the relationship is shown for Pu in Figure 28. The DU, IEU and HEU sets are labelled and although the 3D surfaces for the latter pair are very close together they do not overlap. This may not be the case for other sets of enrichment types however.

Each set of curves follows a similar pattern to the Pu curves as the U becomes more self-absorbing. The more horizontal black curves are a selection of constant true-mass lines. The diagonal lines (for which $M_2 = kM_1$) are the cases of no attenuation where $M_1$ divided by the [235]U enrichment is equal to $M_2$ divided by the [238]U enrichment. Very small mass lumps will lie on or close to the no absorption lines, and as the lump size increases and the shapes become more attenuated (for the 186 keV line), the curves migrate towards the opposite upper edge of the surface. As the mass and lump size increase further they saturate and the points on the curve bunch closer together. No points should lie outside the respective surfaces for the relevant enrichment type.

Since the point kernel has been used to model the behaviour of U lumps the number of integration intervals was found to have an effect on the resulting counts detected, as discussed for Pu in section 3.6. To ensure that this effect is negated, the number of integration intervals used in the model for each set of lump types used for the U SAC algorithm has been based upon the largest

lump, varying the number of intervals in each dimension so that the counts per second calculated did not vary by more than 1%.
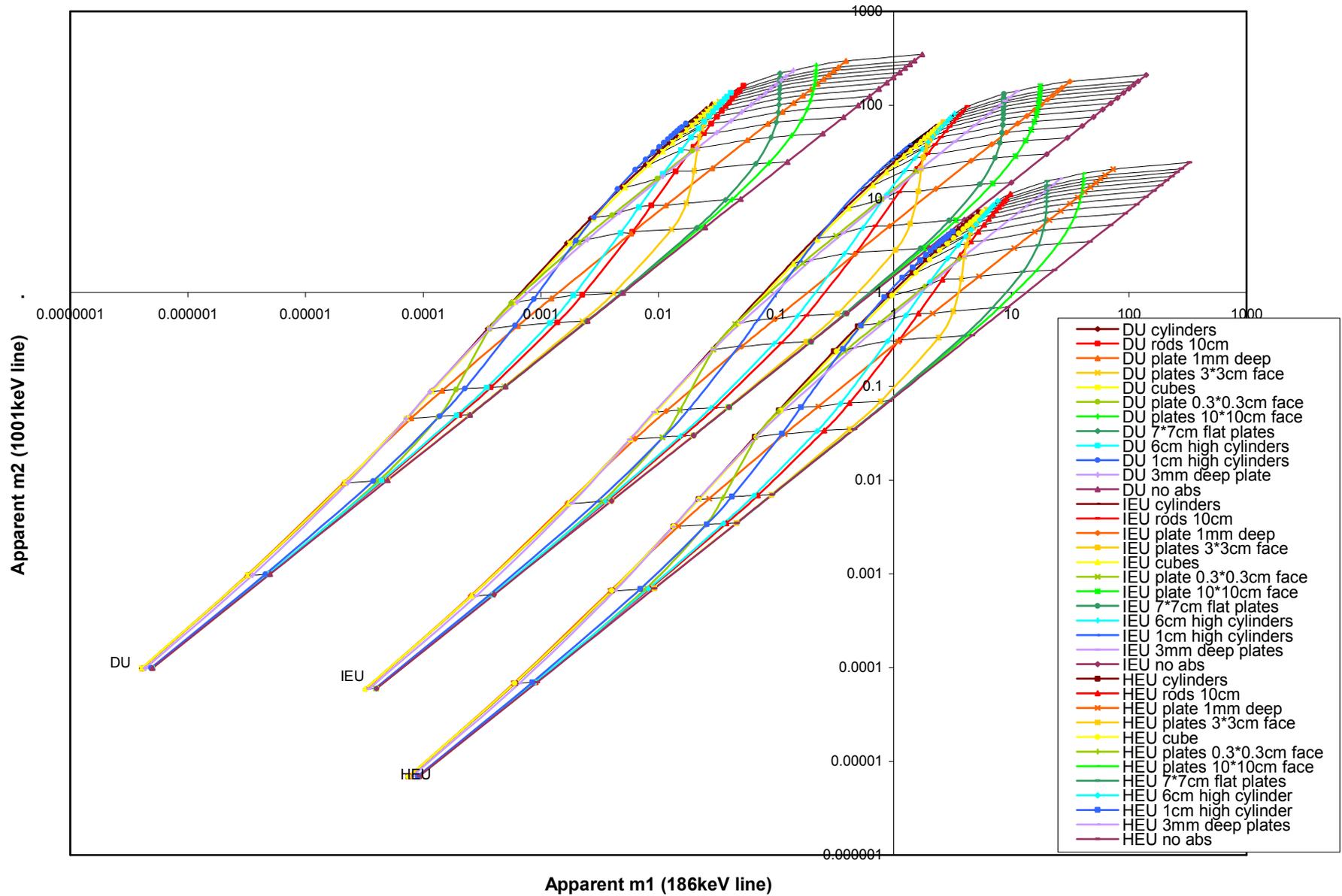
**Figure 40: Uranium self-absorption for three specified enrichment categories.**

The chart axes are labelled **Apparent m2 (1001keV line)** (vertical) and **Apparent m1 (186keV line)** (horizontal).

Legend:
- DU cylinders
- DU rods 10cm
- DU plate 1mm deep
- DU plates 3*3cm face
- DU cubes
- DU plate 0.3*0.3cm face
- DU plates 10*10cm face
- DU 7*7cm flat plates
- DU 6cm high cylinders
- DU 1cm high cylinders
- DU 3mm deep plate
- DU no abs
- IEU cylinders
- IEU rods 10cm
- IEU plate 1mm deep
- IEU plates 3*3cm face
- IEU cubes
- IEU plate 0.3*0.3cm face
- IEU plate 10*10cm face
- IEU 7*7cm flat plates
- IEU 6cm high cylinders
- IEU 1cm high cylinders
- IEU 3mm deep plates
- IEU no abs
- HEU cylinders
- HEU rods 10cm
- HEU plate 1mm deep
- HEU plates 3*3cm face
- HEU cube
- HEU plates 0.3*0.3cm face
- HEU plates 10*10cm face
- HEU 7*7cm flat plates
- HEU 6cm high cylinder
- HEU 1cm high cylinder
- HEU 3mm deep plates
- HEU no abs

## 4.3    A New U SAC Algorithm

A U self-absorption correction method has been developed based upon the modelled results to determine an enrichment category from the three types specified in section 4.2.2 and consequently calculate the total U mass from the two apparent masses at 186 keV and 1001 keV.

A Borland$^{TM}$ Delphi program has then been created to calculate the enrichment based upon the inputted apparent masses. Using this enrichment category the program will scale the $M_1$ (apparent mass from the 186 keV line), $M_2$ (apparent mass from the 1001 keV line) and $M_T$ (the true mass) values accordingly and determine cubic spline fits for each enrichment and shape combination, plotting curves for $M_T$ versus $M_2$, and $M_1$ versus $M_2$ to obtain the self-absorption corrected mass and $M_1$ as functions of $M_2$.

Using the calculated cubic spline fits and the measured 1001 keV line apparent mass ($M_2$), we may take a slice of the 3D surface with varying true mass and $M_1$ and plot the ($M_1$, $M_T$) pairs calculated (as per Figure 31). If the locus between successive points may be approximated as a straight line the SAC U mass may be determined from the measured 186 keV line apparent mass ($M_1$).

The fitting methods used for this U Delphi program (spline fits, straight line fits between adjacent pairs and least squares extrapolation to points beyond the 3D surface) are the same as those for the Pu SAC program, since the programs have used the same modelling methodology and will experience the same effects. See section 3.8.

### 4.3.1  Engine Description

The U SAC engine requires four values to be inputted: the $^{235}$U and $^{238}$U apparent masses ($m_{U235}$ and $m_{U238}$) from the 186 keV and 1001 keV lines respectively and their uncertainties. An estimate of the enrichment is made from the inputted masses, neglecting other U isotope contributions using Equation 24.

This apparent enrichment is then tested to determine the category to be used for the analysis, using the boundaries below:

Enrichment < 0.5 is DU

0.5 < Enrichment < 40 is IEU

Enrichment > 40 is HEU

Based upon this decision the modelled data for total U is scaled using the appropriate enrichment to obtain the 186 keV and 1001 keV apparent masses. Note that the boundaries should be set to 1% and 45% (rather than 0.5% and 40%) in practise to allow for counting statistics.

As for the Pu SAC engine the data limits are tested to ensure there are enough points to perform the calculation correctly i.e. there must be at least 4 points in order for the program to process the least squares fit, therefore the maximum and minimum inputted values of the 1001 keV line mass:

- Upper limit = 161.53 g
- Lower limit = $9.985 \times 10^{-5}$ g.

In practice the lower limit plays little role since the correction is negligible and the signal will ultimately fall below the detection limits.

The program then uses a cubic spline method based upon that used in J. Wood's "Computational Methods in Reactor Shielding" [51] to obtain curves for $M_1$ and $M_T$ versus $M_2$. The inputted 1001 keV mass ($M_2$) is used along with the splines to calculate co-ordinates for a plot of the 186 keV line mass versus true mass i.e. to calculate the co-ordinates of points of a cross-section of the 3D shape for a specific 1001 keV line mass. Additionally there is the case of zero-attenuation, where the true mass and 186 keV mass are both equal to $M_2$.

The data points for the 186 keV masses ($M_1$) for each material and their corresponding true masses are arranged in ascending order using a bubble sorting method [52]. The self-absorption corrected mass may then be found for the inputted 186 keV line mass from the series of ($M_1$,$M_T$) pairs by assuming the locus between the adjacent points between which the inputted $M_1$ lies is a straight line i.e.

$$SACMass = \frac{M1In.(M_T[n+1] - M_T[n])}{(M_1[n+1] - M_1[n])} + M_T[n] - \frac{M_1[n](M_T[n+1] - M_T[n])}{(M_1[n+1] - M_1[n])} \quad \textbf{Eqn. 27}$$

where M1In is the inputted 186 keV line mass, $M_1[n]$ is the array of 186 keV masses for individual materials found from a cross-section of the 3D surface, $M_T[n]$ is the array of true masses for individual materials found from a cross-section of the 3D surface, and [n] and [n+1] are the array components between which the inputted 186 keV mass lies.

If the inputted 186 keV line mass is beyond the limits of the graph a least squares fit is used on the end 4 points, and the line extended to extrapolate the SAC U mass.

The (one sigma) uncertainties on the corrected mass arising from the uncertainties in the measured apparent masses, based on the assumption that a single lump is present, have been implemented within the engine using the following equation:

$$\sigma_{M_T}{}^2 = \left(\frac{\delta M_T}{\delta_1}.\Delta M_1\right)^2 + \left(\frac{\delta M_T}{\delta_2}.\Delta M_2\right)^2 \quad \textbf{Eqn. 28}$$

where $\delta_1 = 0.001 \times M_1$, $\delta_2 = 0.001 \times M_2$ and $\Delta M_n$ are the inputted uncertainty in the 186 keV or 1001 keV masses.

It should also be noted that there are additional uncertainties introduced by the curve fitting techniques; However, these uncertainties are negligible (for all practical purposes) compared to the uncertainties from the counting statistics etc and are therefore ignored in the uncertainty determination process.

## 4.4 Modelled Results

The USAC algorithm has been tested with modelled data for three new lump types with a mass range of 0.1 mg to 350 g. These lumps are:

- 1.5 cm high cylinder
- 2 mm fixed depth flat plate
- 4 cm high cylinder

It is necessary to 'test' the method against modelled results for shapes etc that are not included in the base data set or 'incestuously' over-optimistic results may be obtained. The modelled data for each set have been converted for DU, IEU and HEU and run through the U SAC engine. In each case the engine identified the enrichment type correctly. The results are shown in Figure 41 below.
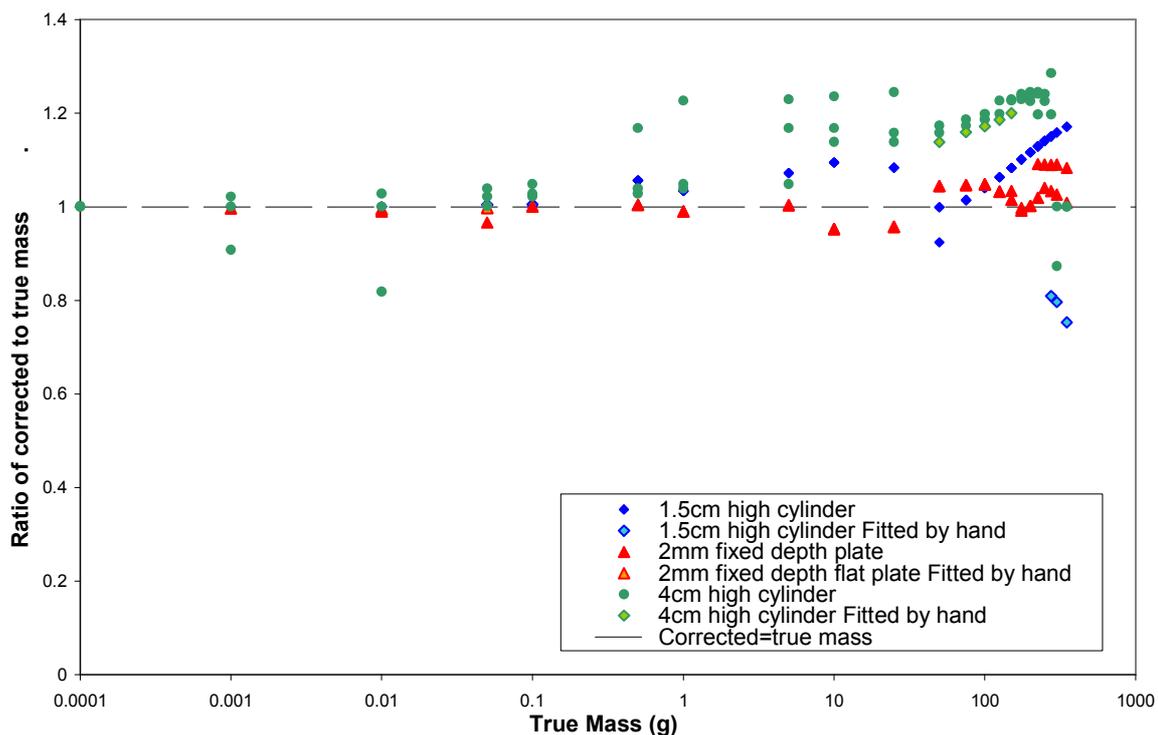


**Figure 41: Graph showing the calculated to true mass ratio using the developed U SAC method for the three enrichment types.**

The U SAC corrected ratios are compared to the uncorrected 1001 keV apparent masses for each new lump type. The results are within approximately 25% of the true mass.

For each new lump type modelled, there are cases where the engine begins to underestimate the true mass result since the data points fall just outside both the 3D surface and the linear least squares extrapolation method is used to determine the true mass. Since the data points in the high attenuation region where this occurs are clustered the least squares extrapolation does not offer a good fit to the whole curve. For severe cases a more accurate result has been obtained by fitting the curve manually outside the U SAC engine to fit the whole curve and extrapolate to these values of $M_1$ and $M_2$. This manual intervention could be avoided by incorporating a more advanced fitting program into the U SAC program.

Other anomalous points have occurred where the modelled data for the 1001 keV apparent mass is outside the range of the U SAC program. As a default either the 1001 keV apparent mass is used for the cases where the input data are below the low bound, or the upper limit used if the 1001 keV apparent mass is above the upper threshold. These points have occurred more for the U SAC method than for the Pu SAC method since only 11 sets of lump shape combinations have been modelled for the U SAC program, whereas the Pu SAC engine had 18 sets of data (because different material densities were also used), and so these data points could be removed or their occurrence reduced with further modelling.

Overall the U SAC engine appears to work well. The results for the 2 mm deep plates all fall within 10% of the true mass across the range of masses. The results for the 4 cm high cylinders have been found to overcorrect at higher masses, and the results for the 1.5 cm high cylinders begin to overestimate with increasing mass above 100 g. These observations may be explained on closer inspection of the new data on the 3D surface, as shown in Figure 42.
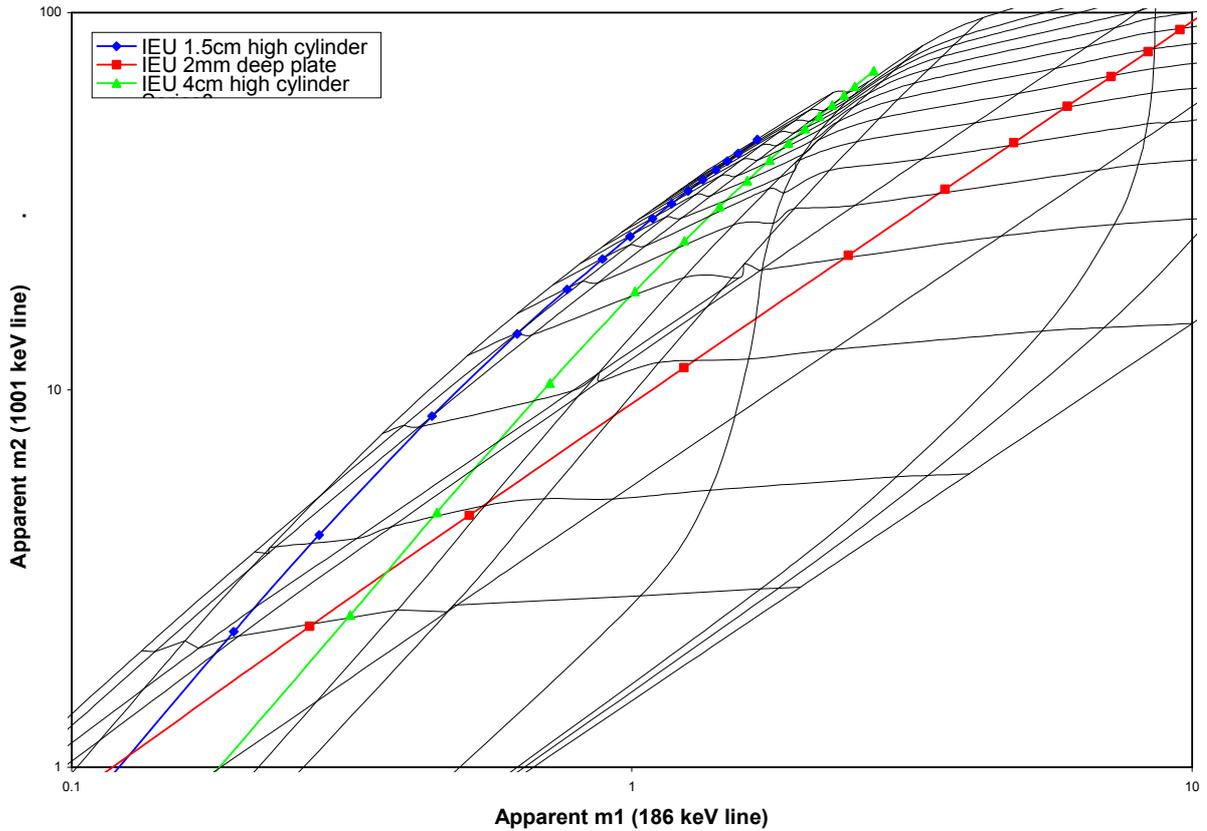
**Figure 42: Magnified section of the apparent M2 versus apparent M1 mass curve for DU including the new test data.**

In Figure 42 the block grid is the original data that are used in the numerical U SAC model. The 4 cm high cylinder data points all lie slightly above the grid line that represents the locus of points for that true mass, and so the cross section of the 3D surface occurs at an $M_2$ that is above the real true mass for that lump, leading to an overcorrection in the final result. Above 5 g the majority of the 4cm high cylinder results are overestimating the true mass; this is where the lump curves begin to enter the higher attenuation region of the 3D surface and so lump shape effects begin to dominate. The 4 cm high cylinder curve lies between the cube and 3x3 cm faced plate curves which behave quite differently in the high attenuation region. This effect could be reduced with further modelling of intermediate attenuating lumps.

## 4.5 Extension to Non-Discrete Enrichments and the Associated Uncertainty

The Delphi program created in section 4.3 has been extended to be applicable for any possible enrichment. The enrichment must be stated by the user prior to its execution and so must be determined independently. Since the program uses one database of initial $M_1, M_2, M_T$ co-ordinates and scales the results according to the correct isotopics prior to the cubic spline calculations, the U SAC mass results for a given lump for different enrichments are the same, and therefore the engine may be used for any known-enrichment lumps. The Delphi$^{TM}$ U SAC program has been tested using the three new lump types used in section 4.4 with enrichments of 0.3%, 30%, 55% and 95% and has been found to work correctly. Exceptions to this observation occur at the extremes of the data where there are too few data points on the $M_T, M_1$ curve to use the least squares approximation.

Where the enrichment has been determined from the spectral data and cannot be categorised into a discrete enrichment type, as demonstrated in the modelled results for section 4.4, there will be an additional uncertainty associated with the $^{235}U$ and $^{238}U$ isotopic estimations. For these cases the uncertainty in the total U SAC mass has been determined from the standard method for combining uncertainties from multiple independent variables by:

$$\sigma_{M_T}^{~2} = \left( \frac{\partial M_T}{\partial M_1} . \sigma M_1 \right)^2 + \left( \frac{\partial M_T}{\partial M_2} . \sigma M_2 \right)^2 + \left( \frac{\partial M_T}{\partial En_{235}} . \sigma En_{235} \right)^2 + \left( \frac{\partial M_T}{\partial En_{238}} . \sigma En_{238} \right)^2 \quad \textbf{Eqn. 29}$$

where $En_i$ is the estimated enrichment of the sample for isotope $i$, $\partial M_1 = 0.001 \times M_1$, $\partial M_2 = 0.001 \times M_2$, $\partial En_i = 0.001 \times En_i$, $\partial M_T$ in each case are the changes in $M_T$ when $\sigma M_T$ is mapped through the USAC process, $\sigma En_i$ is the uncertainty in the enrichment for isotope $i$, and $\sigma M_n$ are the inputted uncertainties in the 186 keV or 1001 keV masses at the one standard deviation level providing the total uncertainty in $M_T$ is at one standard deviation..

## 4.6    Measured Results

The U SAC program has been tested using U Zebra plates (sections of fuel fabricated for an experimental reactor) with an enrichment of approximately 93%, stored inside a polythene bag made from 125 μm thick polythene sheet and placed inside another additional polythene bag for safety purposes. The mass and dimensional data for the sources are displayed in Table 8 below. All the plates have a central hole and two notches cut on one edge, except plate 4009 which is half of one of the larger plates (e.g. 4005) and so has a semicircular hole on one edge. Additionally, the polythene bagged-sources 4005-8 have been taped to a cardboard sheet for identification purposes. The source thickness has been estimated based upon the known mass and dimensions of the plates and an estimated density of 18.7 g.cm$^{-3}$.

**Table 8: Uranium zebra plate data including total U masses and plate dimensions.**

| ID | U mass (g) | U-235 mass (g) | Dimensions (mm) |
|----|-----------|----------------|-----------------|
| 4005 | 17.91 | 16.66 | 25 x 25 x 1.5 |
| 4006 | 17.94 | 16.68 | 25 x 25 x 1.5 |
| 4007 | 17.99 | 16.73 | 25 x 25 x 1.5 |
| 4008 | 17.95 | 16.69 | 25 x 25 x 1.5 |
| 4009 | 9.56 | 8.89 | 25 x 13.5 x 1.5 |
| 4010 | 4.21 | 3.91 | 11 x 14.0 x 1.5 |

The exact isotopics of the sources are not known by Destructive Analysis. An NDA2000 analysis using MGA with sources 4005-4009 (81.35 g U) at the centre of a soft matrix in the AQ2 gives MGAU results of:

U-234: 0.632 +/- 0.13%

U-235: 84.13 +/- 8.43%

U-238: 15.24 +/- 8.54%

An average of near 93% enriched samples has been used to estimate the isotopic data for the zebra plates. The data are shown in Table 9.

**Table 9: Zebra plate isotopics assumed from an average of known near 93% enriched sources.**

| Isotope | Weight % | Uncertainty % |
|---------|----------|---------------|
| U-233 | 0.001 | $1.0 \times 10^{-5}$ |
| U-234 | 1.008 | $5.0 \times 10^{-4}$ |
| U-235 | 92.994 | 0.009 |
| U-236 | 0.372 | $1.9 \times 10^{-5}$ |
| U-238 | 5.625 | $5.6 \times 10^{-4}$ |

The sources have been measured on the bench using a 20 mm thick, 70 mm diameter BEGe detector, with a polyethylene end cap, at a distance of 100 mm from the end cap, using the experimental set-up shown in Figure 43.
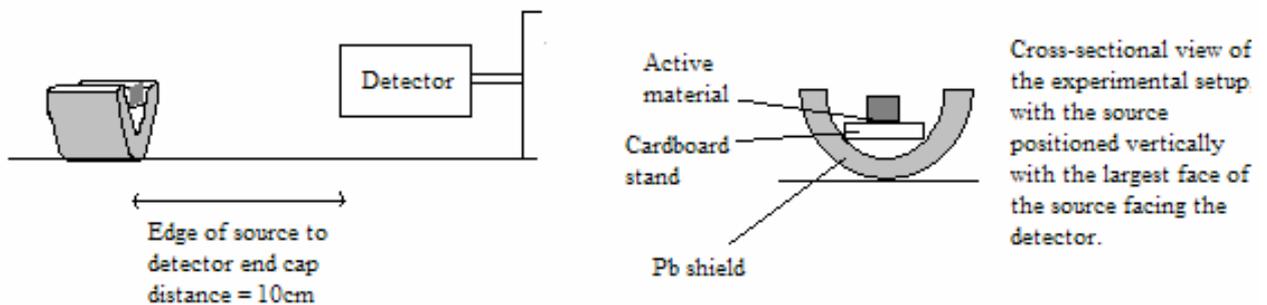


**Figure 43: Sketch showing the source orientation and basic experimental setup for the U Zebra plate measurements.**

The sources have been measured in multiples with the following combinations:

- 4010      mass = 4.21 g
- 4009      mass = 9.56 g
- 4008      mass = 17.95 g
- 4008-9      mass = 27.51 g
- 4007-8      mass = 35.94 g
- 4007-9      mass = 45.5 g
- 4006-8      mass = 53.88 g
- 4006-9      mass = 63.44 g
- 4005-8      mass = 71.79 g
- 4005-9      mass = 81.35 g

Multiple sources have been stacked behind one another, positioned vertically with the largest face of each towards the detector and with the smaller sources in the group closest to the detector. A reference pulser has been used to determine the deadtime correction. The effect of the polythene has been modelled and has been found to be negligible (approximately 0.6% at 1001 keV and 1% at 186 keV) for the purposes of this study. Each source combination was measured for 600s, apart from single sources 4010 and 4009 for which the count time was increased to 1200s and 900s respectively because the 186 keV and 1001 keV peaks could not be identified with smaller count times.

The apparent masses for the 143.8 keV, 163.3 keV, 185.7 keV, 205.3 keV and 1001 keV lines have been determined and used with the U SAC program for non-discrete enrichments for the isotopics listed in Table 9. The data have also been analysed according to the Infinite Energy Extrapolation method with both linear and polynomial fits being applied to carry out the extrapolation to 1/E=0. An example spectrum for the 4005-4009 sources at 10cm from the detector is shown in Figure 44. The results are shown in Figure 45.
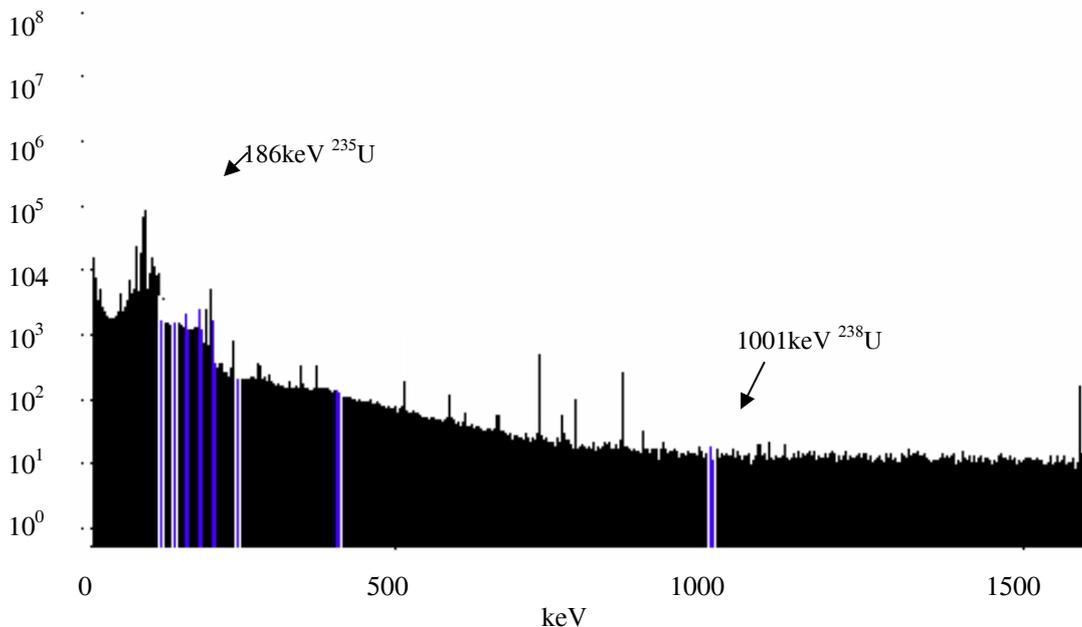


**Figure 44: An example spectrum for the 4005-4009 zebra plates at 10 cm from the detector showing the 186 keV and 1001 keV peak on a log scale.**

103

It should be noted that these sources have been measured statically (non-rotating) with the face of the source approximately parallel to the face of the detector. The developed U SAC program has been designed to work with lumps which present a changing orientation to the detector (as they are moved along with the contents of the drum as it is rotated in front of the detector and also as the drum is viewed from several vertical positions). Hence the apparent masses at all energies are larger than expected for a rotated geometry, with a stronger effect experienced by the lower energy lines. However, the corrected result using the USAC method is more dependent on the change in 1001 keV apparent mass and so the overall effect is the method still performs well.
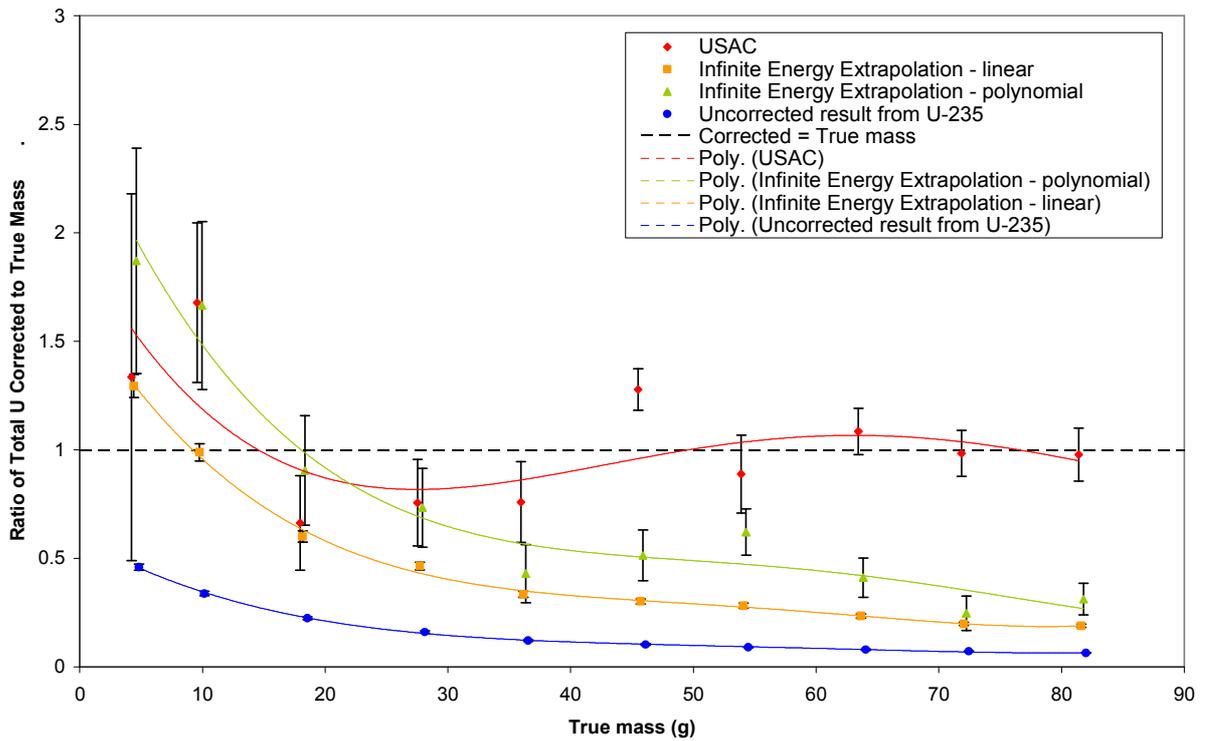


**Figure 45: The ratio of corrected to true mass as a function of true mass for U zebra plate measurements showing U SAC and Infinite Energy Extrapolation correction methods.**

Figure 45 shows the total U results calculated with the developed USAC method, results using an infinite energy extrapolation (IEE) method using the 143.8 keV, 163.3 keV, 185.7 keV and 205.3 keV lines from $^{235}$U, plus the uncorrected result based upon the $^{235}$U apparent mass and isotopics only. The uncorrected results begin at half of the true mass and reduce continuously as the mass increases. Both IEE fitting methods produce results which reduce to below 0.3 of the true mass for higher massed samples. This may be because the line energies used for the fitting methods are small and so there is not a high-energy (less attenuated) line to improve the extrapolation to $1/E = 0$, resulting in a lower U mass from these more attenuated lines.

The U SAC method has been shown to perform very well, with the majority of results within 35% of the true mass, offering a significant improvement compared to the other methods. The deviations from the true mass have most likely occurred mainly due to statistics since HEU produces very few 1001 keV counts. The sources were measured for live times of between 600s and 1200s depending on the mass of the sample, whereas in real assay systems, especially with heavier matrices, the practical counting time may be too short to obtain enough 1001 keV counts for HEU unless the U mass is very large. However, for lower enrichment U samples (with a higher $^{238}$U content) would provide improved statistical accuracy.

One advantage to the USAC method is that it may be used for mixed U and Pu drums without difficulty since it uses only the 186 keV and 1001 keV lines, whereas the IEE methods and the X-ray fluorescence methods both suffer from interference from Pu lines in such cases.

## 4.7 Extension to Multiple Lumps using Modelled Data

The extension to waste packages that contain U in the form of multiple lumps (which may be of different sizes, shapes and materials) has been investigated. In practice it is rare for a waste item to contain only a single piece of fissile material. Due to the high degree of non-linearity observed in the U model, the combination of a series of smaller lumps was expected to produce a smaller SAF than that expected for a single large lump of equal mass and therefore the model was expected to underestimate the total U in a sample. The analysis of multiple lumps has considered the impact on the DU result only but due to the nature of the algorithm the other enrichment results ought to behave similarly.
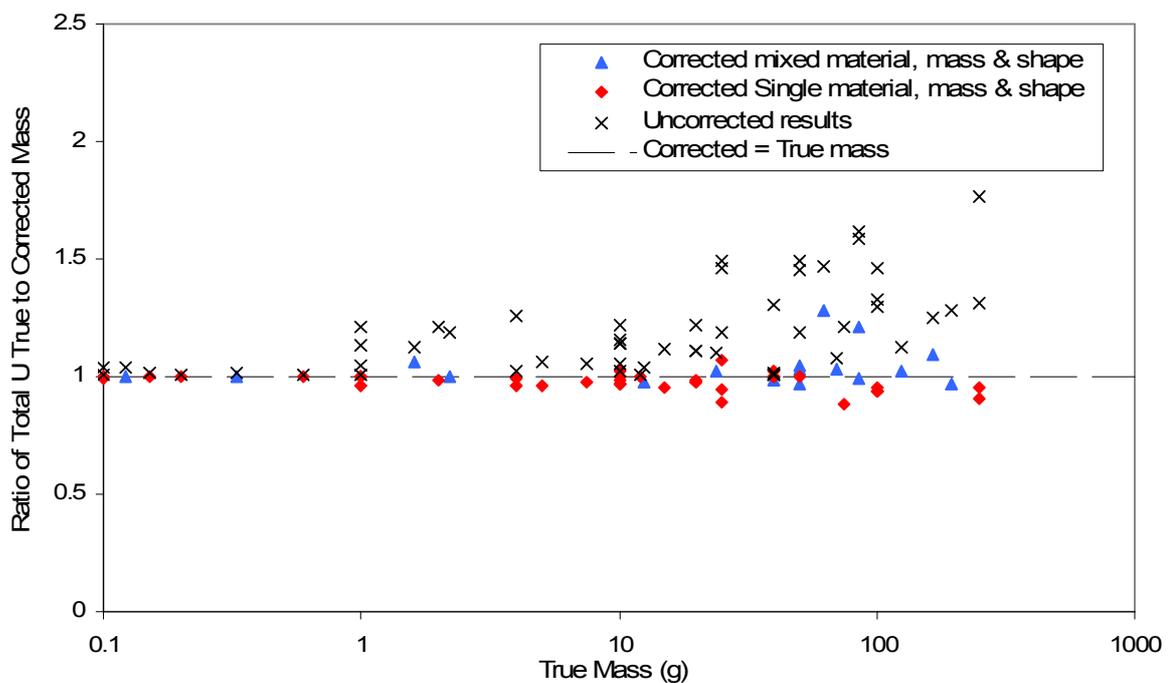


**Figure 46: Plot of the ratio of true to corrected mass versus the total true mass for random combinations of lumps collated from independently-treated single lump modelled data for DU.**

The apparent 186 keV and 1001 keV masses for a number of material/shape combinations were summed and used as input for the algorithm to see how it would behave for multiple lumps. These combinations include several lumps of the same material and shape, plus random mixed numbers

and types of lumps over the range of masses and shapes studied in the USAC algorithm development, plus the series of newly-modelled data sets used for the modelled results. The results are presented in Figure 46.

The uncorrected total U mass (derived form the 186 keV apparent masses and isotopics) are also plotted as a comparison. The results do not produce perfect ratios of one, as expected, because as the individual lumps are combined their total 186 keV apparent mass will be higher than that of a single lump of equivalent mass, whereas the 1001 keV apparent mass will remain relatively similar. Consequently the corrected mass of the combination of lumps is underestimated, demonstrated by approximately 70% of the USAC corrected data points. The remaining corrected masses lie above the ratio equals one. This is line due to fluctuations in the data points in the high attenuation region of the $M_1$:$M_2$:$M_T$ plot.

It should be noted that these lump combinations have been performed by summing the apparent masses of individual lumps, assuming that all lumps are independent and that the gamma rays from each lump are not attenuated by any other lump on their path to the detector. However this may not be the case in real waste drums and the resulting apparent mass may, conceivably at least, be attenuated more than for the examples shown above.

The method appears to work well for multiple lumps of various compositions. All of the modelled results are within 28% of the corrected equal to true mass line, with 79% of the modelled results achieving values within 5% of the true mass. These observations could be developed with a more detailed study to implement a contribution to the TMU of the sample from the U self-absorption in the case of multiple lumps. For example, if a 1-$\sigma$ uncertainty is required by the user (68% of the results should lie within the area if a Gaussian distribution applies, for example), this equates to a 3.5% uncertainty if the uncertainty is assumed to be constant across the mass range.

It may also be observed that the variation from the corrected equal to true mass line appears to increase with increasing true mass and so the TMU contribution from multiple lumps could be refined to be a function of the apparent mass with a more in-depth study.

# 5  REAL DRUM EFFECTS

## 5.1  Introduction

The work in the previous sections has concentrated on the self-absorption effects for lumps of ideal, unencapsulated Pu and U sources at known distances from calibrated detectors. In real waste packages the situation is far from ideal - the contents of the waste package are unknown and this will increase the uncertainty in the assay results. There may be effects and uncertainties that will affect the accuracy in estimating the fissile mass of the waste drum by gamma spectrometry ([7], [62], [63], [64]), for example:

- Uncertainties in nuclear data e.g. branching ratios, specific activities etc.
- Calibration uncertainties
- Background radiation
- Dead time effects
- Gamma source spatial distribution/ the assumption of volume weighted average (VWA) source distribution
- Matrix composition, density and homogeneity
- Gamma source lump size and composition
- Segment overlap for multiple segment or detector systems
- Isotopic estimation uncertainties

The extent of the effect of some of these factors may be estimated from the results of ancillary measurements, such as gamma transmission for matrix density/composition, differential absorption for lump correction and low energy spectral analysis for isotopics. Factors affecting the result that remain unknown need to be taken into account in the total measurement uncertainty (TMU). A similar problem is encountered in the determination of 'less than' values to be quoted where the material is not detected but the effect of these factors should be incorporated. For further reading on MDAs and less-than levels see Lochamy and Currie ([65], [66]).

### 5.1.1 The Total Measurement Uncertainty

Any measurement result is irrelevant without a statement of its associated uncertainty to give realistic bounds between which the true value is believed to lie for a given confidence level. It is often convenient to assume that the probability distribution is symmetrically Gaussian to permit easy representation and combination of errors. However this may not be correct and it may be more appropriate to use asymmetric uncertainties (as demonstrated in section 5.2). The Total Measurement Uncertainty encompasses all uncertainties that are associated with the measurement including statistical errors, correction methods and algorithm uncertainties.

The effects listed above are discussed in more detail in the following sections, followed by a discussion of the best practical method for the combination of uncertainties to be incorporated into the TMU for the waste package. A relative quantitative comparison of the contribution from some of these components is given in Davidson *et al* [64].

The work in this section has been performed as part of a project team at Canberra UK for the SILWAS system. The contribution from the author has involved modelling of the gamma source spatial distribution and matrix effects with the Pu SAC algorithm, plus performing Pu and U measurements on the AQ2 as part of CUK Factory Acceptance Tests. Sections describing the isotopic estimation uncertainties (5.3) and combination of uncertainties (5.6) have been devised by other members of the project team [31] and are included here for completeness and clarity of the methods used in the SILWAS AQ2 measurements for sections 5.7 and 5.8.

## 5.2 Gamma Source Spatial Distribution

The spatial distribution of the active material in the waste package may be homogeneous (volume weighted average (VWA) by which we mean equal volumes of the waste contain equal activity) for some waste types. Soft waste consisting of many articles of clothing, gloves and overalls etc. which are surface contaminated may approximate closely to homogeneity. For other types of waste highly heterogeneous source distributions may be encountered and in the extreme, all the activity may be concentrated at a single 'point', which could be anywhere within the matrix. This seriously impacts the activity measurement where the matrix attenuation is high.

The TMU contribution from a non-uniform source distribution [67] may be calculated from the far-field correction factor using computer-modelled spatial response results. Where a lump correction has been applied, such as by differential absorption, the measurement uncertainties are propagated through the correction algorithms, otherwise a TMU contribution from the lump effect is calculated.

The simplest way to determine the TMU of a result is generally to approximate its distribution to a symmetrical Gaussian curve; however, this approximation is rarely entirely appropriate. Although the number of sources may not be known in waste packages a single-lump distribution assumption serves to accommodate the worst case scenario so that the associated positive and negative TMUs can be ensured to cover the true value. The user may prefer a more conservative assumption, for example 2, 5 or 7 sources. For these cases as the maximum and minimum limits are finite and the Gaussian distribution is infinite, if the distribution is sampled multiple times it will become narrower and become more symmetric. The Single- and Two- lump distribution examples are demonstrated in the following sections.

### 5.3.1 Single Lump Distribution

A point kernel model has been used to generate the frequency versus the count rate dependence for a typical 205 litre drum inside an AQ2 for three different density matrices: $\rho = 0.0$ g.cm$^{-3}$, 0.5 g.cm$^{-3}$ and 1.0 g.cm$^{-3}$ using the 414 keV line from $^{239}$Pu. The model splits the drum into 150x150x150 voxels (150 integration intervals for height, radial and polar) and determined the

count rate with the source placed in each voxel. The distributions of frequency co-ordinates versus countrate are non-Gaussian and also become highly asymmetrical at higher densities as shown in Figure 47.
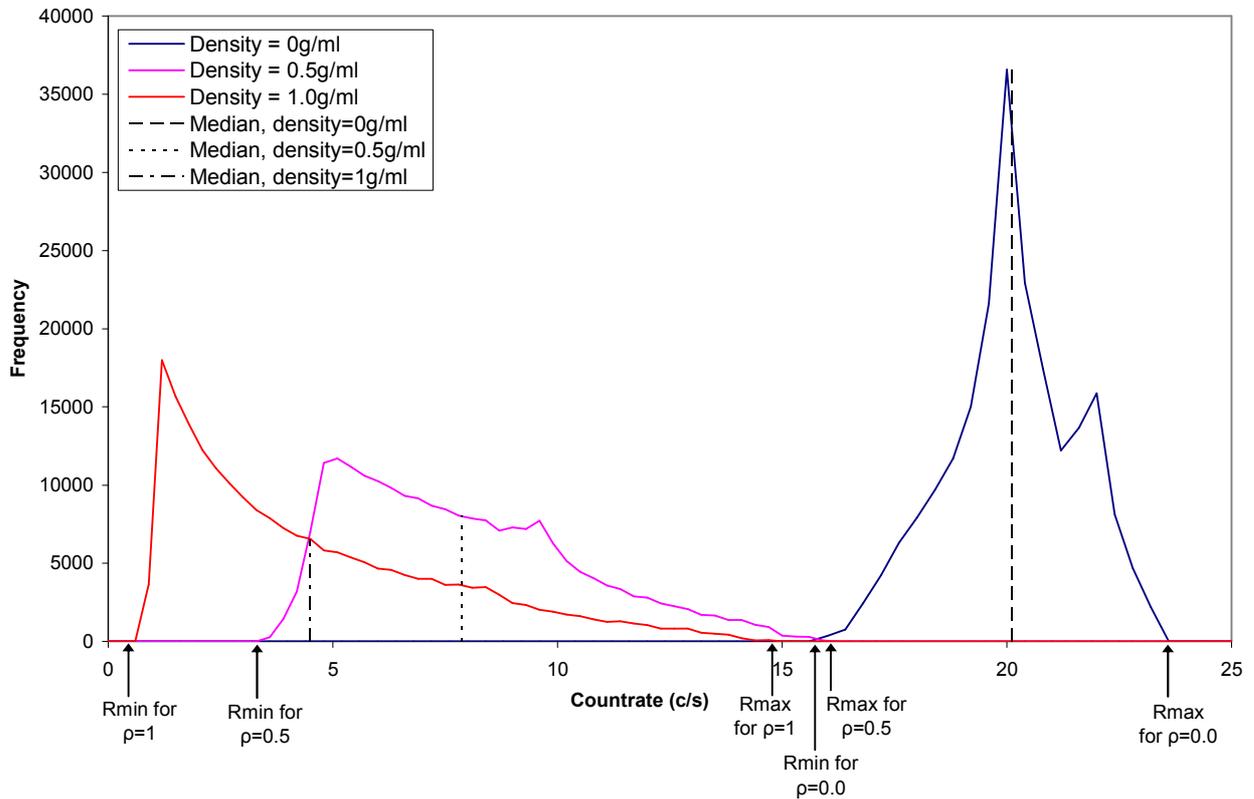


**Figure 47: Frequency versus the count rate for a 205l drum in an AQ2 for three different density matrices: $\rho = 0.0$ g.cm$^{-3}$, 0.5 g.cm$^{-3}$ and 1.0 g.cm$^{-3}$ using the 414 keV line from $^{239}$Pu.**

Figure 48 demonstrates the point source behaviour for the case $\rho = 0.5$ g.cm$^{-3}$ for a standard 205 litre drum in an AQ2 compared with a single Gaussian curve normalised to the area under the graph.
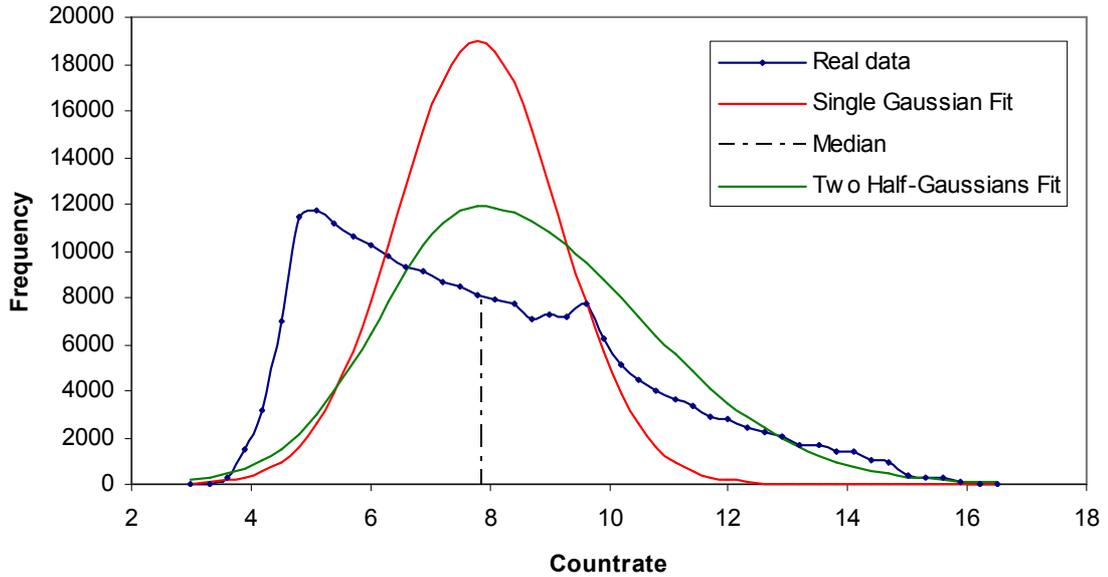
**Figure 48: Response distribution for a 0.5 g.cm$^{-3}$ filled 205 litre drum in an AQ2.**

Figure 48 demonstrates that the high-countrate tail is not encompassed by the single Gaussian curve; hence the whole dataset cannot be accurately represented with a single Gaussian distribution for a point source model. To combat this, each half of the distribution has been approximated to half of a different Gaussian curve about the median point. The maximum and minimum limits of the distribution ($R_{max}$ and $R_{min}$) will be taken to be the 3σ limits. The double Gaussian approximation does not fit the real data exactly; however the tails of the data are now fitted much better than with the single Gaussian fit.

The TMU contribution from a non-uniform source distribution is calculated from the far-field correction factor using computer modelled spatial response results for $R_{min}$ and $R_{max}$ (normalised to the median value). These have been plotted as a function of the attenuation correction factor for a sample of typical drum types to be used with an AQ2. The attenuation correction factor is given by [69]:

$$CF = \frac{-k.\ln T}{1 - T^k}$$  **Eqn. 30**

where k is the geometric correction factor, traditionally set to 0.823 (although it may vary depending on the geometrical set-up of the detectors) and T is the transmission ratio for varying energy and density for various drum types. The transmission ratio may take values between 0 and

1 (exclusive) where T→0 indicates that none of the gamma rays are able to penetrate the matrix, and T→1 indicates that almost all of the gamma rays are able to reach the detector.

$R_{min}$ and $R_{max}$ have been plotted as a function of the attenuation correction factor (CF) for varying energy and density in Figure 49. See 2.5 for details of the listed drum types.
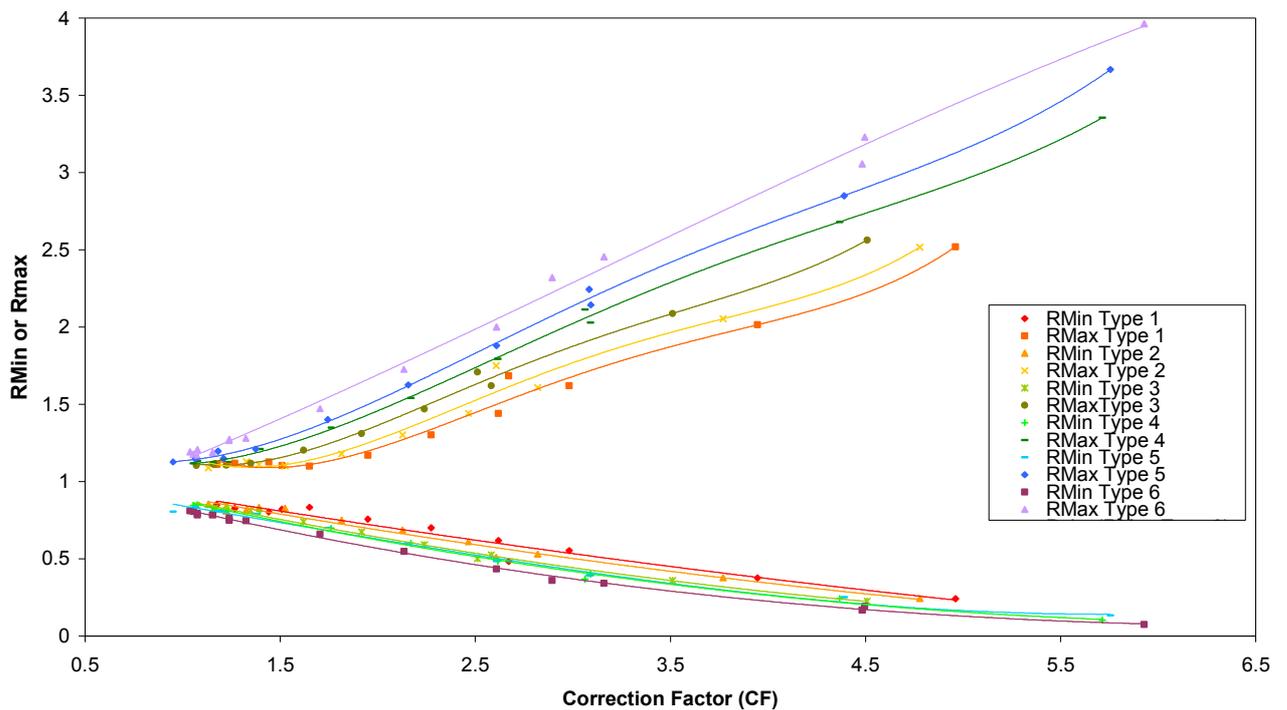


**Figure 49: $R_{min}$ and $R_{max}$ versus the attenuation correction factor CF for a set of typical empty drums inside an AQ2.**

The $R_{min}$ and $R_{max}$ versus CF curves are geometry dependent (i.e. they must be modelled for each instrument and container type) and may be fitted to approximate trend lines which can be parameterised as functions of the matrix correction factor, CF:

$$R_{min} = \sum_{i=0}^{4} R_{min\,i} \cdot (CF)^i \quad \text{and} \quad R_{max} = \sum_{i=0}^{4} R_{max\,i} \cdot (CF)^i \qquad \textbf{Eqns. 31\&32}$$

The 1σ uncertainty to be incorporated into the positive and negative TMUs is then found using the equations below where $A_i$ is the activity of nuclide $j$ (segment $j$):

$$\sigma_{ij}^{-Sp} = \frac{-(1 - R_{max}).A_{ij}}{3R_{max}} \quad \text{and} \quad \sigma_{ij}^{+Sp} = \frac{(1 - R_{min}).A_{ij}}{3R_{min}} \qquad \textbf{Eqns. 33\&34}$$

The method described above assuming a point source spatial distribution has been incorporated into the SILWAS Post Analysis engines as part of the AQ2 TMU analysis (see section 2.5.1.3 and 5.7).

## 5.3.2  Multiple- Lump Distribution

The above study is based upon the assumption that the activity is concentrated into a single point source. The current section explores a multiple-source distribution. For this case the distribution is expected to narrow and become more symmetric due to the central limit theorem [70]. For example, using a simplified TMU component based upon a symmetric distribution:

$$\sigma_{ij}^{Sp} = \frac{R_{max} - R_{min}}{2m\sqrt{n}}.A_{ij} \qquad \textbf{Eqn. 35}$$

where m is the number of standard deviations that the data spread represents e.g. $3\sigma$, and n is the number of sources. Therefore an increase to n lumps offers a $\sqrt{n}$ reduction in the TMU component.

The distribution for n = 2, 3 and 4 has been modelled by sampling the distribution in Figure 47 using a Delphi$^{TM}$ program. The frequency distributions for each n for densities of 0 g.cm$^{-3}$ and 1 g.cm$^{-3}$ have been normalised and plotted comparatively in Figure 50.
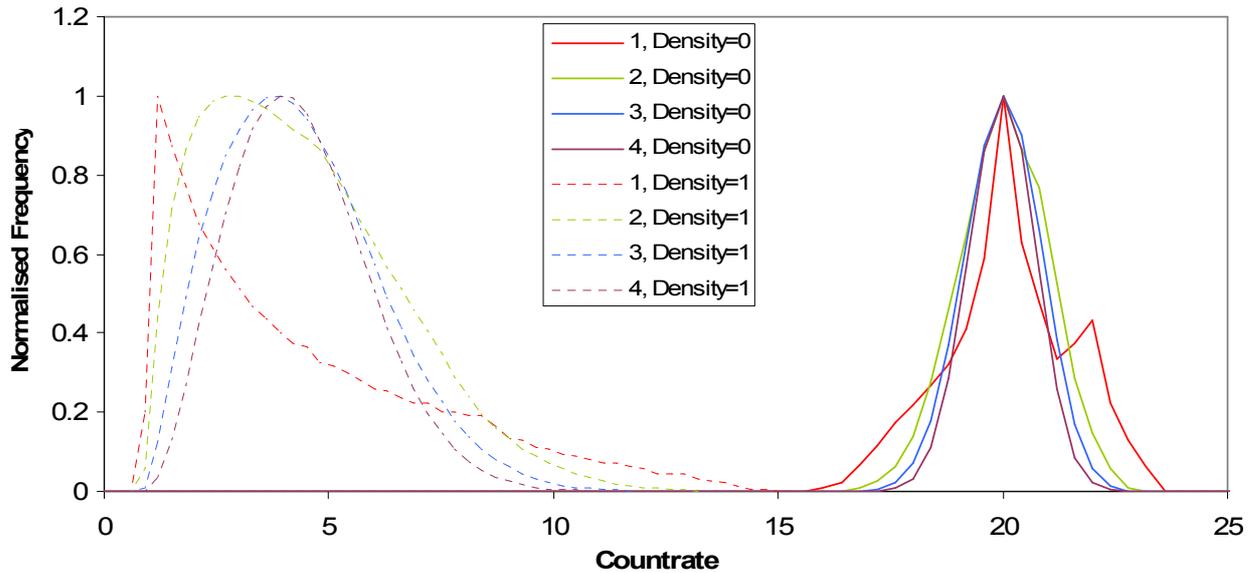
**Figure 50: Response distribution for a 205 litre drum in a typical AQ2 for ρ= 0.0 g.cm$^{-3}$ and 1.0 g.cm$^{-3}$ using the 414 keV line from $^{239}$Pu, showing the relative frequency distribution assuming 1, 2, 3 and 4 sources.**

As the number of source lumps is increased from 1 to 4 the distributions alter to approach a symmetric near-Gaussian distribution. For a higher number of lumps the maxima and minima will remain the same whereas the mean value would shift so that the distribution becomes symmetrical. From the user-selected number of lumps graphs for $R_{min}$ and $R_{max}$ as a function of the attenuation correction factor (CF) for varying energy and density may be created and parameterised, consequently the component to the TMU from the gamma source spatial distribution may be derived using the method in section 5.3.1.

## 5.3 Isotopic Estimation Uncertainties

All isotopes from Pu and U may be difficult to measure directly in reality since some emitted energies (104 keV from $^{240}$Pu) are in complex regions of the spectrum. The relative isotopic composition of Pu and U may be available directly from a declaration supplied by the user or may be determined from gamma spectrometry (e.g. using sophisticated spectrum analysis codes such as MGA ([71], [72]), MGAU [61] and FRAM ([59], [60]) or direct gamma measurement). In any case there will be uncertainty data for each entry which will need to be incorporated with the other errors. These data will be used to determine the activity of those isotopes which do not produce usable gamma-ray lines and hence can not be well-quantified directly using waste assay spectrum analysis. In the further treatment of the uncertainties, calculated for all the isotopes, it is important to recognise that there will be a correlation between the isotopic components for all the isotopes determined by isotope ratio. Therefore, when combining those uncertainties, the uncertainties for the activities for all the isotopes must be added linearly and not in quadrature since they are correlated.

For those nuclides for which the isotope data $(w_i, \sigma_{wi})$ are available:

$$A_i = A_F \frac{w_i}{w_F} \ , \quad A_{Pu} = \sum_{Pu} A_i \ \text{ and } \ \sigma_{A_{Pu}} = \sum_{Pu} \sigma_{A_i} \qquad \textbf{Eqns. 36,37\&38}$$

where $A_i$ and $A_F$ are the activities of the nuclides determined by isotope ratio and the measured fiducial nuclide and $w_i$ and $w_F$ are the respective isotopic fractions. The fiducial nuclides for Pu and U for example would be $^{239}$Pu and $^{235}$U (or $^{238}$U) respectively.

The above treatment is a well established method and assumes the isotopic data are available on a per package basis. However it may be more appropriate to use measured isotopics on a per segment basis for example, for a well-collimated SGS being used for drums containing mixed Pu isotopic sets. In this case the set of weights and uncertainties $(w_i, \sigma_{wi})$ is extended to $(w_{ij}, \sigma_{wij})$ where $j$ is the segment index. The dataset $(A_{ij}, \sigma_{Aij})$ is then generated for all nuclides $i$ (whether measured or isotope ratio) and all segments $j$. At this stage all $\sigma_{Aij}$ are either derived from the analysis of the gamma-ray spectra i.e. there are no spatial or lump uncertainties incorporated at this point. Using the normal method for combining uncorrelated random errors:

$$A_{ij} = A_{Fj} \frac{w_{ij}}{w_{Fj}} \quad \text{and} \quad \sigma_{A_{ij}} = A_{ij} \sqrt{\left[ \left( \frac{\sigma_{w_{ij}}}{w_{ij}} \right)^2 + \left( \frac{\sigma_{w_{Fj}}}{w_{Fj}} \right)^2 + \left( \frac{\sigma_{A_{Fj}}}{A_{Fj}} \right)^2 \right]} \qquad \textbf{Eqns. 39\&40}$$

where the isotopic ratios are declared or obtained from MGA/MGAU using the summed (over all segments) spectrum.

## 5.4　Gamma Source Lump Size and Composition

Where activity is concentrated locally, for example in the form of a lump, there may be high local gamma attenuation that is not taken into account by the gross matrix attenuation correction. A correction for gamma-ray self-absorption may be applied for certain materials e.g. U and Pu as demonstrated through sections 3 and 4, and this correction will introduce an additional source of uncertainty. A self-absorption correction is not likely to be applied if the nuclide is to be quoted as a less-than value.

In this section the Pu self-absorption correction method developed in section 3 has been incorporated and by way of example the lump uncertainty component of the TMU is derived as follows. The Pu SAC engine may be represented by the following transformation:

$$A_{Puj} = \Psi\left(A_{129j}, A_{414j}\right) \qquad \textbf{Eqn. 41}$$

where $A_{nj} = A_{nij}/w_{ij}$ is the apparent Pu activity from line of energy $n$ keV for segment $j$, $A_{nij}$ is the apparent activity of isotope $i$ determined from line of energy $n$ and $w_{ij}$ is the isotope fraction of isotope $i$ (in practice isotope $i$ is $^{239}$Pu). $A_{Puj}$ is defined by $A_{Puj} = A_{ij}/w_{ij}$ where $A_{ij}$ is the corrected $^{239}$Pu activity. $A_{129j}$ and $A_{414j}$ have measurement uncertainties which are propagated through the Pu SAC engine so that:

$$\sigma^2_{A_{Puj}} = \left(\frac{\partial\Psi}{\partial A_{129j}}\right)^2 \sigma^2_{A_{129j}} + \left(\frac{\partial\Psi}{\partial A_{414j}}\right)^2 \sigma^2_{A_{414j}} \qquad \textbf{Eqn. 42}$$

and

$$\sigma_{A_{ij}} = A_{Puj} w_{ij} \sqrt{\left[\left(\frac{\sigma_{w_{ij}}}{w_{ij}}\right)^2 + \left(\frac{\sigma_{A_{Puj}}}{A_{Puj}}\right)^2\right]} \qquad \textbf{Eqn. 43}$$

These ($A_{ij}$, $\sigma_{Aij}$) then replace the uncorrected $A_{ij}$ for $^{239}$Pu. The other Pu isotope activities are then determined using the relative isotopic data. Note that the Pu SAC uncertainty component so far is obtained purely from measurement uncertainties mapped through the software engine algorithm and contains no contribution from intrinsic imperfections in the engine.

There is an additional uncertainty component that may be included which has been derived from observations of the behaviour of the algorithm for multiple Pu lumps. Assuming this contribution

is constant across the mass range, this approximates to a 6% uncertainty in the Pu mass (see section 3.11) and so the uncertainty in $A_{Puj}$ becomes:

$$\sigma^2_{A_{Puj}} = \left(\frac{\partial \Psi}{\partial A_{129j}}\right)^2 \sigma^2_{A_{129j}} + \left(\frac{\partial \Psi}{\partial A_{414j}}\right)^2 \sigma^2_{A_{414j}} + \left(0.06 A_{Puj}\right)^2 \qquad \textbf{Eqn. 44}$$

A similar method has been devised for U lump correction [80] using two lines from different isotopes i.e. $A_{Uj} = X(A_{186j}, A_{1001j})$. It requires that the isotopic ratios are known or that the isotopic ratios are one of a small number of different types.

The methods studied in the previous sections assume that the required line energies have been successfully identified in the spectrum and that the lump correction (Pu or U) has been run. However in the event that the lump correction fails to run, or for the case that the required lines are not available in practice due to noise in the spectrum or absorption within the matrix and so it is not possible to perform a self-absorption correction from the available data, an alternative approach is to introduce a lump component to the uncertainty based upon a worst-case scenario. For example for Pu, the 414 keV line apparent mass may be used on the assumption that all the Pu is situated in a single (or a user-specified number of) spherical metal lump(s) so that an upper bound on the true Pu mass present can be set. An example of this contribution is demonstrated by Figure 51 which displays the $3\sigma$ contribution to the TMU assuming that the Pu is concentrated in 1, 3 and 1000 equal spherical lumps, based upon the total observed 414 keV apparent mass.
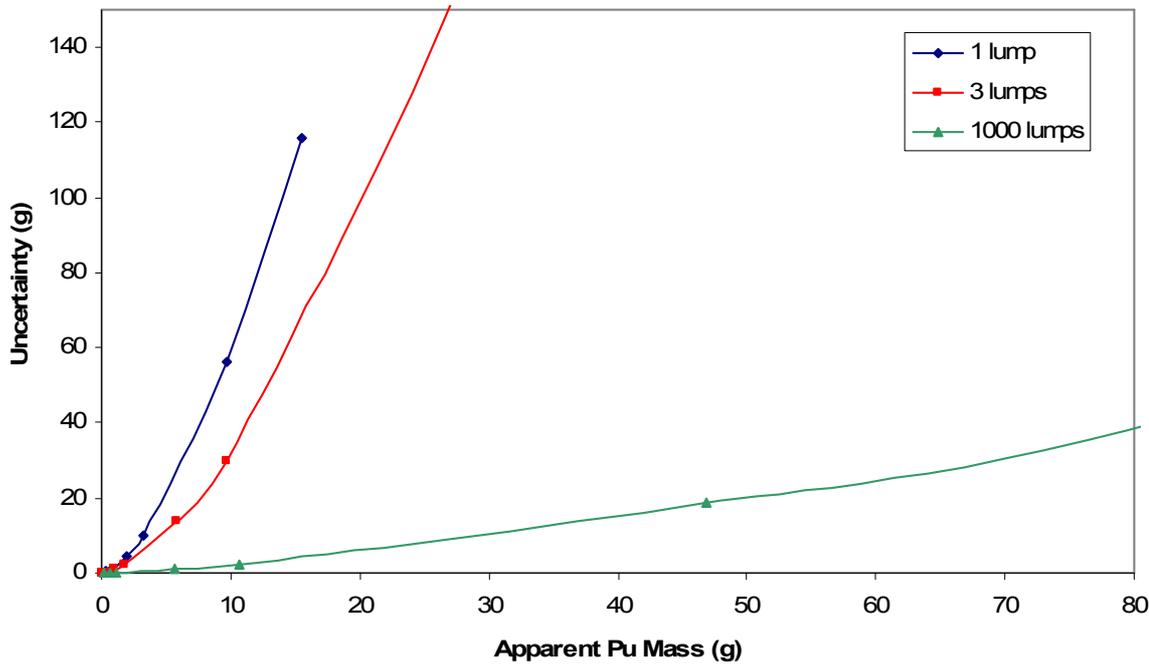
**Figure 51: Graph showing the lump component to the TMU based upon all the activity being concentrated into n spherical lumps.**

This leads to a positive TMU component, $\sigma_{ij}^{+Lump}$ to be incorporated into the final result. For example, if an apparent 414 keV Pu mass of 10 g is measured, then if we assume that there is only one lump present in the drum (somewhat unrealistic) there could be as much as 67.2 g of Pu present and so a 3σ positive TMU contribution of approximately 57.2 g should be introduced (19.0 g at 1σ) where a Pu lump correction cannot be applied. If a more disperse distribution is assumed, e.g. 1000 lumps, then an apparent 414 keV Pu mass of 10 g would require a 3σ positive TMU contribution of approximately 1.82 g (0.6 g at 1σ).

The above methodology reinforces the need for asymmetric TMUs since the positive component may be many times the apparent activity. However the negative component is necessarily zero because self absorption can only lead to an overestimate when no correction has been applied.

## 5.5 Matrix Effects

As gamma rays are emitted from a source they are not only attenuated by the material within the source itself, but are also scattered and absorbed by other materials on their path to the detector, such as the waste drum and its matrix. Matrix density and the effect of matrix composition [73] may be measured by gamma transmission but in practice there are limitations as to the accuracy to which this may be achieved. Mean transmission values at a few discrete heights along the rotating item are all that is normally available. Not all assay systems use transmission sources and may infer a mean density based upon the weight of the drum and fill height information.

Techniques such as the mean density method, differential peak attenuation method or a transmission correction may be used to correct for matrix effects. These are described briefly below ([74], [75]).

**Mean Density Method**

If the fill height of the drum is known approximately (i.e. the height to which the drum is filled with matrix), the average density of the sample material may be determined from the net item weight. A correction may then be applied to the observed masses using the relationship between the matrix attenuation and the matrix density **(**[43]**,** [76]). This method is only applicable if the attenuating materials present in the drum have a similar density and an average attenuation is meaningful.

**Differential Peak Correction**

The differential peak correction uses the fact that different line energies emitted from the same nuclide will experience different amounts of attenuation. An energy-dependent efficiency correction factor may be determined from observing the relative peak intensity of the two lines compared to a calibration, to estimate $\rho t$ ("mass thickness" [43]) for the matrix. The correction factor ($CF_j$) for peak j may then be calculated as:

$$CF_j = e^{-\mu_E \rho . t}$$

<div align="right">**Eqn. 45**</div>

This technique does not require the user to make any assumptions about the uniformity of the matrix; however it has the disadvantage that it depends upon adequate count rates to obtain an accurate correction factor.

**Transmission Correction**

A transmission measurement using a known source, which emits gamma-rays at energies across the range of passive peak energies that are of interest, may be used to measure the matrix attenuation across a number of segments of the drum. The transmission factor at the peak energies may be estimated using the ratio of the net peak areas from the transmission measurement and a transmission calibration made with an empty container. An interpolation technique is used to determine the correction factor (CF) for intermediate energies. The correction factor may be determined, for example, from the Parker formula (Equation 30) [69]. This formula was populated for a uniform cylindrical sample (uniform matrix attenuation and emission) whose distance to the detector is large compared with the dimensions of the detector collimator and the sample itself, but in practice it works quite well using effective values for $k$ [77].

## 5.5.1 Homogeneous Matrix Modelling for a single point source for Pu

The matrix effect has been modelled for single unencapsulated Pu cylinders (diameter = height) inside a typical 1.5 mm thick stainless steel walled drum (density 7.8 g/cm$^3$) with three different types of matrices:

- Soft matrix - polyethylene of density 0.11 g/cm$^3$
- Intermediate matrix - aluminium of density 0.35 g/cm$^3$
- Hard matrix - steel of density 0.7 g/cm$^3$

The detectors have been modelled as two 7 cm diameter by 2.1 cm long uncollimated detectors at 74 cm from the axis of drum rotation, at heights of the top and base of the source. The source has been modelled as a bare cylindrical Pu lump with masses ranging from 0.0001 g to 300 g, at the centre of the drum with 25 cm of homogeneous matrix surrounding it. The results have been normalised to an empty 1.5mm thick steel drum.

The effect of the matrix material is to further attenuate both lines. However the 129 keV line is not as severely attenuated relative to the 414 keV line as it would be for self-absorption in Pu (see Figure 6). Consequently the curves migrate towards a more attenuating region of the $M_1:M_2$ graph, usually outside the 3D surface, as the matrix is altered.

The effect on the Pu SAC corrected masses for these results for attenuation-uncorrected results and with the Parker formula correction have been observed. The results are displayed in Figure 52. Note that for some cases the data are too far beyond the 3D surface for the Pu SAC algorithm to function correctly and so a trend line has been drawn to show the data trend excluding these points.
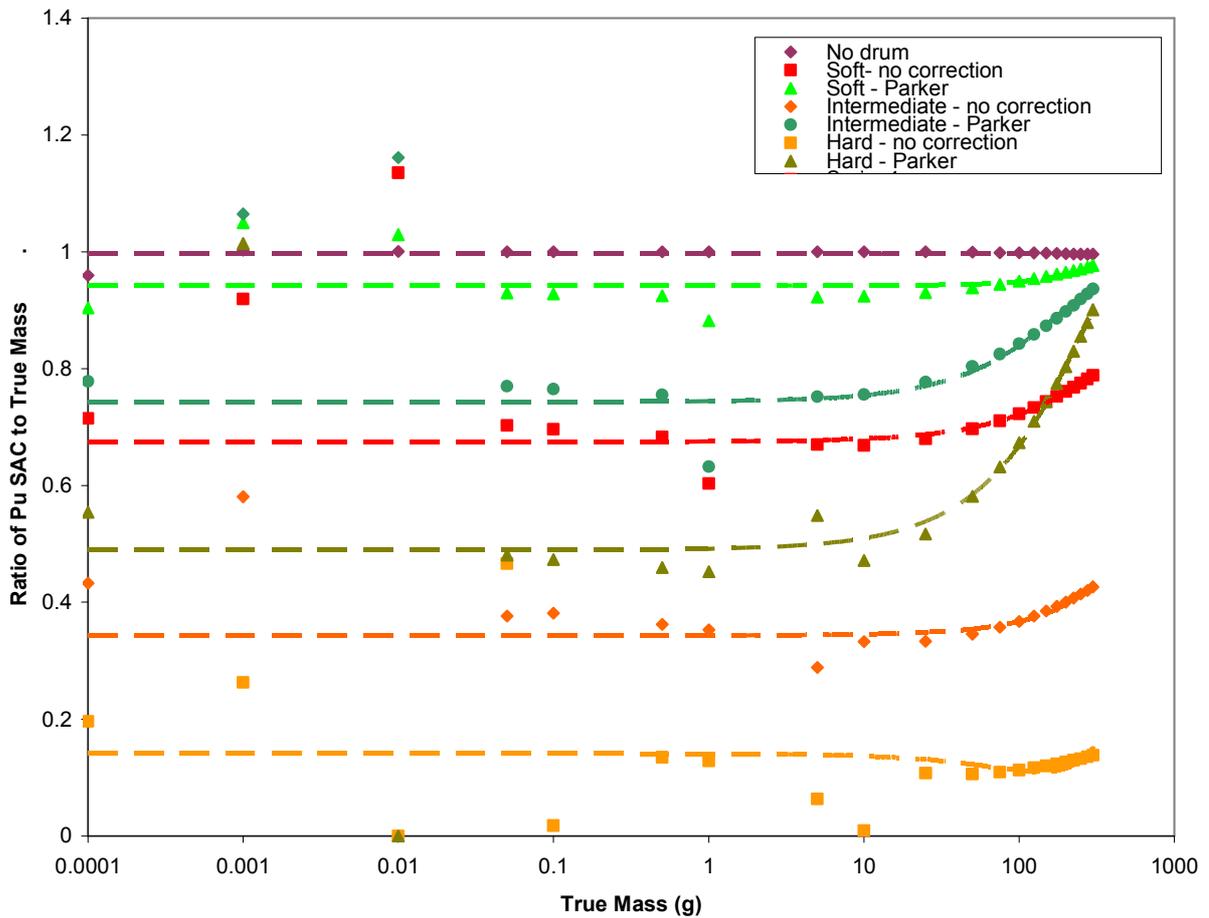


**Figure 52: Graph showing the ratio of Pu SAC to $M_T$ versus $M_T$ for no matrix correction and the Parker formula correction, with data trend lines drawn.**

The results without a matrix correction and with the Parker formula correction all produce under-corrected Pu SAC results, with the matrix-uncorrected results being affected more severely. This is because the measured matrix attenuated apparent masses produce $M_T$:$M_1$ curves that are too small, giving an extrapolation to a reduced true mass. This is demonstrated in Figure 53. The blue line ("With $M_2$ for No Matrix") displays the result that would be obtained without the matrix and drum present i.e. the true $M_T$:$M_1$ curve for the Pu sample inside the drum. The red and green curves show the matrix uncorrected and Parker corrected curve that would be expected with the matrix present. The corresponding dashed lines are the apparent 129 keV ($M_1$) and 414 keV ($M_2$) masses that would be inputted into the Pu SAC algorithm. As shown, the measured $M_1$ with a matrix present are far lower than would be obtained without the matrix and drum present since the measured $M_2$ is also lower (due to the extra attenuation), resulting in a small curve which, when extrapolated to the correct $M_1$ produces a significantly reduced $M_T$.
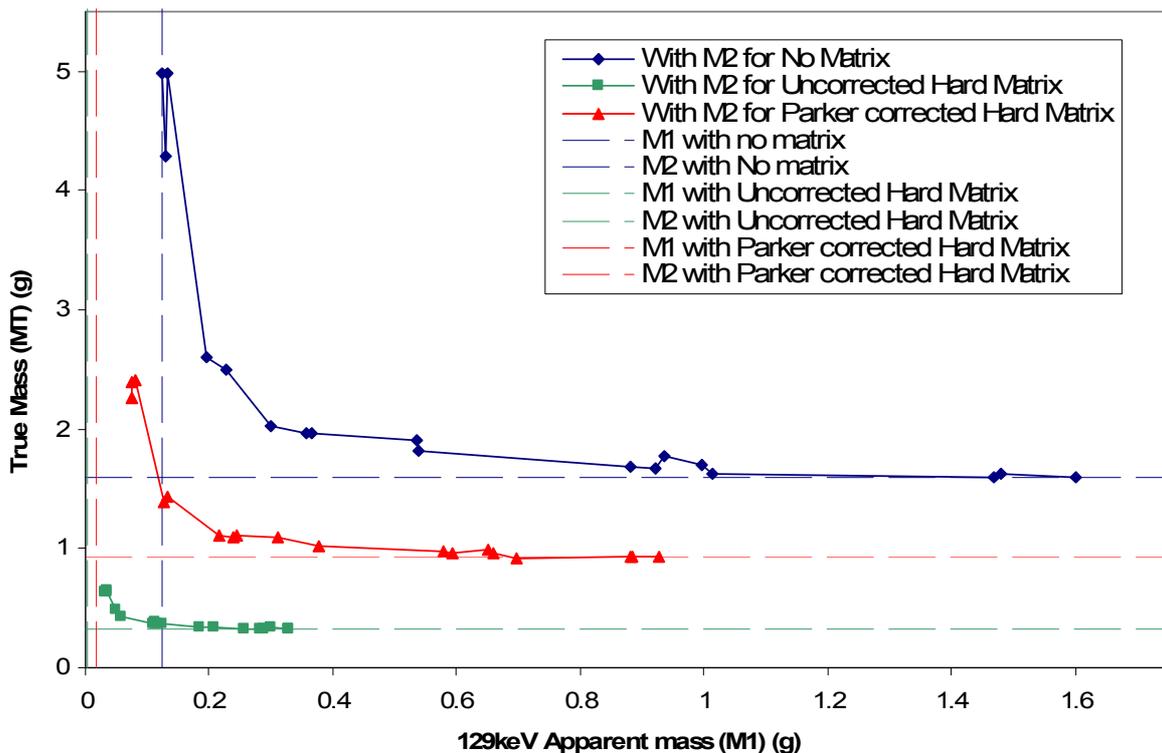


**Figure 53: $M_T$:$M_1$ curve for a 5g Pu cylinder as would be measured with and without a hard matrix in place, and the Parker corrected curve.**

The Parker formula does improve the results; however the matrix effect is still apparent, with the hard matrix producing results as low as 43% of the true mass. The reason for this is because the Parker formula is designed for use with a source uniformly distributed throughout the drum. This assumption may be appropriate for drums with unknown material which may be present in numerous lumps or distributed throughout the drum, however the above example is for one source located at the centre of the drum. In this case a more appropriate correction is to use:

$$CF_j = \frac{1}{\sqrt{T_j}}$$  **Eqn. 46**

This correction factor is derived using the assumption that the radiating sample is a point source, the radiation from which must traverse the attenuating material through the radius of the drum i.e. half the distance traversed by the transmission source.

Using the point source matrix correction factor the result is much improved with the soft, intermediate and hard matrices, giving Pu SAC corrected masses within 0.5% of the results without a matrix and drum (excepting the 0.0001 g sample).

This basic study demonstrates that with a matrix correction method that is suited to the drum set-up that is being assayed, the Pu SAC method performs very well. However, since the contents of waste drums are rarely known an approximation must be made; consequently the selected matrix correction method will introduce additional errors.

Observations of the behaviour of the Pu SAC method following a correction using the Parker formula, have shown that it may be possible to establish a matrix correction uncertainty based upon some assumptions about the waste. If the drum is assumed to contain a matrix (approximately homogeneous) of a maximum density, then average or maximum under-correction produced by the Pu SAC correction could be incorporated into the positive component of the total measurement uncertainty.

The above study has been performed assuming that there is a single source at the centre of the drum. This is an unrealistic scenario since there may be any number of various sized lumps scattered throughout the drum and matrix. Often packing records can confirm that more than one source is likely to be present. It also assumes homogeneous matrices; however this assumption is unrealistic since real waste matrices may contain numerous materials, fill-heights and densities. This has a significant impact on the gamma assay result. One of the effects of an inhomogeneous matrix is to provide streaming paths for gamma rays to escape the matrix. This results in higher apparent activities i.e. the matrix correction is less severe than calculated for the homogeneous case. It may also have the opposite effect where discrete activity is located within locally dense absorbing material.

## 5.6 Uncertainty Combinations from Multiple Detector

This section has been created as part of the SILWAS project team at Canberra UK [31] and is included here for completeness only.

### 5.6.1 Combining TMUs for Totally Segmented Assay

The function of the TMU combination is to compute a set of quantities $(A_i, \sigma_{A_i}^{\pm})$ which are the activities and associated 1-$\sigma$ uncertainties for the nuclides $i$. Thus:

$$A_i = \sum_j A_{ij} \quad \text{and} \quad \sigma_{A_i}^{\pm} = f\left(\sigma_{A_{ij}}, \sigma_{ij}^{\pm Sp}, \sigma_{ij}^{\pm Lump}\right) \qquad \textbf{Eqns. 47\&48}$$

where $\sigma_{ij}^{\pm Sp}$ is the spatial uncertainty, and $\sigma_{A_{ij}}$ is the uncertainty obtained from the gamma-ray spectrum analysis (possibly Pu or U SAC corrected) for nuclide $i$ and segment (or detector) $j$, including statistics, efficiency calibration, transmission correction (matrix), more specifically all uncertainties that will be treated as independent random errors.

If the uncertainty components may be treated as uncorrelated the separate TMU components for each segment can be combined in quadrature as shown:

$$\sigma_{A_{ij}}^{\pm} = \sqrt{\left(\sigma_{A_{ij}}\right)^2 + \left(\sigma_{ij}^{\pm sp}\right)^2 + \left(\sigma_{ij}^{\pm Lump}\right)^2} \qquad \textbf{Eqn. 49}$$

where the signs are either all positive or negative providing two sets of equations for each side of the asymmetric distribution.

The total activity of the package can be obtained by summing the individual activities from each isotope over the segments:

$$\sigma_{A_i}^{\pm} = \sqrt{\sum_j \left(\sigma_{A_{ij}}^{\pm}\right)^2} \qquad \textbf{Eqn. 50}$$

This applies where the segments of the package are completely separate entities. This situation is approximately true in a SGS spectrometer, although there is always a degree of overlap of segments within the viewing angle of the collimator. Therefore, strictly speaking there is a degree of correlation between the $\sigma_{A_{ij}}^{\pm}$ but quadrature summing is still the most appropriate method.

## 5.6.2 Combining TMUs for Uncollimated Segmented Assay

Certain types of instruments, while using multiple detectors to provide physical coverage of the package, may for the sake of maximising sensitivity, have minimal or even no collimation. In this case the treatment provided in section 5.6.1 may be inappropriate because of strong correlations between individual detector responses. An alternative approach is to add the transmission corrected assay results for all the detectors before a self-absorption correction is performed, and to treat the spatial TMUs as totally correlated and add them linearly. Thus:

$$A_{ip} = \sum_{j} A_{ij} \quad \text{and} \quad \sigma_{A_{ip}}^{\pm} = \sqrt{\sum_{j}\left(\sigma_{A_{ij}}\right)^2 + \left(\sum_{j}\sigma_{A_{ij}}^{\pm Sp}\right)^2} \qquad \textbf{Eqn. 51\&52}$$

where the activities $A_{ip}$ and $A_{ij}$ are not yet self-absorption corrected at this stage, whereas they have been corrected in the corresponding equations in section 5.6.1. Also the $\sigma_{A_{ip}}^{\pm}$ does not yet contain the lump component. Note the linear addition of the spatial TMU components before the sum is added in quadrature with the statistical TMUs.

These activities and uncertainties are then fed into the self-absorption correction engines for U and Pu, or if not available, the lump uncertainty is combined as shown:

$$\sigma_{A_i}^{\pm} = \sqrt{\left(\sigma_{A_{ip}}^{\pm}\right)^2 + \left(\sigma_i^{\pm Lump}\right)^2} \qquad \textbf{Eqn. 53}$$

## 5.6.3 Combination of Uncertainties from Isotopes Obtained from Isotope Ratio

Isotope ratio nuclides should have isotopic contributions combined by addition, for example, to obtain the total Pu mass where only $^{239}$Pu has been measured directly and the isotopic ratios are known either by measurement or by declaration, then the total Pu mass ($m_{Pu}$) and uncertainty can be derived as follows:

$$m_{Pu} = \sum_{i}^{Pu}\frac{A_i}{S_i} \quad \text{and} \quad \sigma_{m_{Pu}} = \sum_{i}^{Pu}\frac{\sigma_i}{S_i} \qquad \textbf{Eqns. 54\&55}$$

where $A_i$, $S_i$ and $\sigma_i$ are the activity, specific activity and uncertainty of isotope $i$ respectively. This assumes that the dominant source of uncertainty in the mass of the components is the $^{239}$Pu measured mass.

Where more than one isotope is measured directly, but one of these is the principal fiducial nuclide $F$ which determines the ratioed isotopes $IR$, the uncertainty is derived thus:

$$\left(\sigma_{m_{Pu}}\right)^2 = \left( \sum_i^{Pu(F+IR)} \frac{\sigma_i}{S_i} \right)^2 + \sum_i^{OtherMeasured} \left( \frac{\sigma_i}{S_i} \right)^2 \qquad \textbf{Eqn. 56}$$

The above sections have extended the standard methods of combining uncertainties to include asymmetric uncertainties, spatial, matrix and self-absorption uncertainties, plus uncertainties from collimated or uncollimated assay systems. These methods have been incorporated into the Canberra SILWAS system which is used in the following sections to produce results for measured U and Pu samples within waste matrices.

## 5.7 Pu Measurements in a Simulated Waste Drum

The AQ2 has been used as part of the SILWAS system to analyse results from simulated waste drums. The AQ2 analysis methodology is described briefly in section 2.5 and includes the Pu self-absorption correction, Total Measurement Uncertainties (TMUs) and Minimum Detectable Activity methods described in the previous sections to obtain asymmetric TMUs using a transmission measurement with the Parker formula, MGA and MGAU isotopics analysis codes, a single lump source distribution and the NUDS method described in section 2.5. The Pu SAC method used for the analysis used the $6^{th}$ order log polynomial method (see section 3.8.2.1) due to the availability of the SILWAS for experiments being in the early stages of Pu SAC development.

The algorithms have been tested using the AE4043/nn sources measured at various locations in an empty drum, a soft matrix-filled drum and a hard matrix-filled drum, as part of the SILWAS Factory Acceptance Tests. The artificial soft matrix drum has been created inside a 205l drum (IND10164) from various paper, plastics and soft materials e.g. gloves, plastic wrappers etc. to have a density of approximately 125 g.cm$^{-3}$. The drum also contains a jig made from two plastic layers (as shown in Figure 54) with cardboard tubes to hold the sources. Cardboard strips are used as spacers to place the sources at the required heights within the tubes.



**Figure 54: Axial view of two 205l drums filled with artificial soft and hard matrices.**

The hard matrix has been constructed from various dense materials such as lead blocks, stainless steel tubes and other scrap metal, with an average density of approximately 570 kg.m$^{-3}$. The jig to hold the sources has been constructed from aluminium tubes. Empty aluminium cans are used as spacers to place the sources at the required heights within the tubes.

## 5.7.1 AE4043/5 Pu Spatial Variation Tests

The first set of experiments have been performed to test the Pu SAC and spatial variation component of the TMU by placing AE4043/5 (4.98 g PuO$_2$, 4.94 g Pu) at 16 different positions within an empty 205l drum (IND10164). The selected source positions are made from a combination of the following: height as a fraction of the maximum height (0/3, 1/3, 2/3, 3/3), and radius (0/3, 1/3, 2/3, 3/3). The plastic and cardboard jig shown for the soft matrix in Figure 54 has been used to locate the sources. All of the supporting components were made from cardboard to minimize attenuation.

**Table 10: Spatial variation results for AE4043/5 at 16 positions in an empty 205l drum.**

| Height | Radius | Mass (g) | Uncert. +ive (g) | Uncert. -ive (g) | Residuals* (s.d.) |
|---|---|---|---|---|---|
| 3/3 | 0/3 | 4.235 | 0.449 | 0.313 | 1.57 |
| 3/3 | 1/3 | 4.177 | 0.387 | 0.276 | 1.97 |
| 3/3 | 2/3 | 4.267 | 0.392 | 0.281 | 1.72 |
| 3/3 | 3/3 | 5.545 | 0.798 | 0.716 | -0.84 |
| 2/3 | 0/3 | 3.91 | 0.347 | 0.25 | 2.97 |
| 2/3 | 1/3 | 4.065 | 0.366 | 0.26 | 2.39 |
| 2/3 | 2/3 | 4.204 | 0.376 | 0.286 | 1.96 |
| 2/3 | 3/3 | 4.64 | 0.615 | 0.545 | 0.49 |
| 1/3 | 0/3 | 3.89 | 0.358 | 0.258 | 2.93 |
| 1/3 | 1/3 | 3.871 | 0.35 | 0.253 | 3.05 |
| 1/3 | 2/3 | 3.983 | 0.359 | 0.258 | 2.67 |
| 1/3 | 3/3 | 4.013 | 0.366 | 0.265 | 2.53 |
| 0/3 | 0/3 | 4.226 | 0.604 | 0.53 | 1.18 |
| 0/3 | 1/3 | 4.213 | 0.535 | 0.467 | 1.36 |
| 0/3 | 2/3 | 4.242 | 0.57 | 0.505 | 1.22 |
| 0/3 | 3/3 | 4.86 | 0.625 | 0.547 | 0.13 |

*Residuals are positive unless stated otherwise

The results including asymmetrical positive and negative 1σ TMUs and deviations between the known and measured mass divided by the positive or negative uncertainty as numbers of standard deviations are displayed in Table 10 and Figure 55.
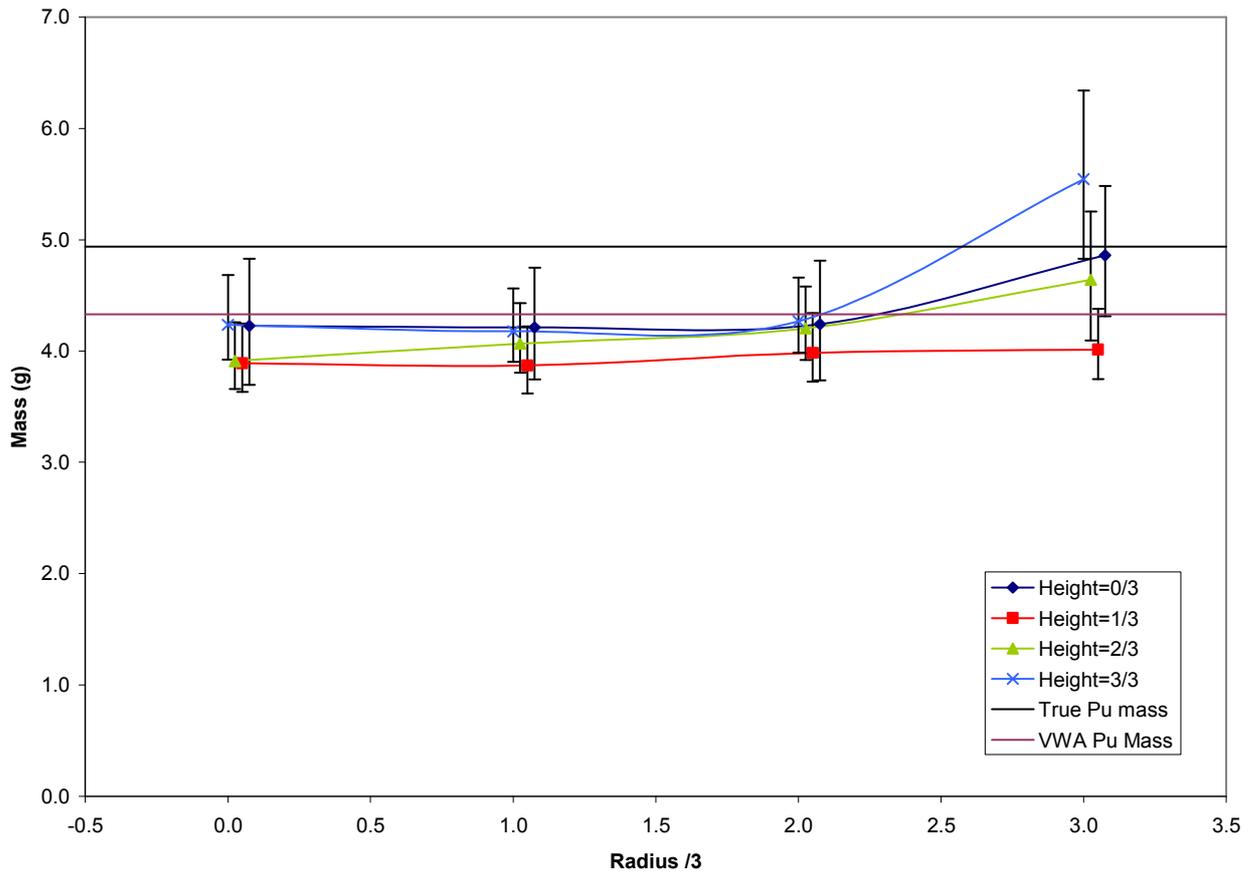


**Figure 55: Spatial variation results for AE4043/5 at 16 positions in an empty 205l drum with staggered radius values for clarity.**

The measured mass is almost always less than the source mass (4.94 g Pu), however when the uncertainties are taken into account only one result is not encompassed by 3 standard deviations. The VWA Pu mass derived by volume weighted summing is 4.331g +0.143g -0.119g, compared to the known mass of 4.94 g.

The discrepancy between the reported mass and true source mass may be due to the attenuation caused by the 2.5 mm thick stainless steel case of the source (see section 3.3). The stainless steel encapsulation is not corrected with the matrix correction because the Pu source is (generally) not in the beam of the transmission source in the test geometries used, reducing the observed activity at all energies. The modelled lumps that have been used in previous sections are for bare Pu, $PuO_2$ sources whereas real bare sources are not available for use. The Pu SAC process will correct the apparent 414 keV mass for self absorption in the $PuO_2$ in the source and largely ignore the encapsulation because the differential absorption between 129 keV and 414 keV for steel is small. Real waste is not generally expected to contain encapsulated lumps.

The 2/3 radius values are close to the VWA value; the centre of the drum shows a reduction of about 5% relative to the 2/3 radius. The high value at height=3/3, radius=3/3 may be due to the close approach made by the source to the top detector because the height of the source in this case is a close match to the detector height.

## 5.7.2 Pu Soft and Hard Matrix Tests

The second set of experiments in the AQ2 involved placing AE4043/1 (0.099 g Pu), AE4043/5 (4.94 g Pu) and AE4043/5-10 (with a total Pu mass of 91.3 g) at mid-height at the centre and edge of 205 litre drums with soft and hard matrices. Similar jigs were used to those described in the previous section. The results including asymmetric $1\sigma$ TMUs and residuals in standard deviations are shown in Table 11.

**Table 11: Results for soft and hard matrix measurements in 205l drums.**

| Case | Matrix | Location | Source AE4043/ | True Mass (g) | Mass (g) | Uncert. +ive (g) | Uncert. -ive (g) | Residuals* (s.d.) |
|------|--------|----------|----------------|---------------|----------|------------------|------------------|-------------------|
| 1 | Soft | Centre | 1 | 0.099 | 0.052 | 0.007 | 0.005 | 6.7 |
| 2 | Hard | Centre | 1 | 0.099 | 0.014 | 0.016 | 0.007 | 5.3 |
| 3 | Soft | Edge | 1 | 0.099 | 0.061 | 0.008 | 0.005 | 4.8 |
| 4 | Hard | Edge | 1 | 0.099 | 0.089 | 0.046 | 0.017 | 0.2 |
| 5 | Soft | Centre | 5 | 4.94 | 4.03 | 0.60 | 0.47 | 1.5 |
| 6 | Hard | Centre | 5 | 4.94 | 2.34 | 1.14 | 0.44 | 2.3 |
| 7 | Soft | Edge | 5 | 4.94 | 4.46 | 0.56 | 0.38 | 0.9 |
| 8 | Hard | Edge | 5 | 4.94 | 5.69 | 3.30 | 1.06 | -0.7 |
| 9 | Soft | Centre | 5-10 | 91.4 | 130.7 | 20.3 | 16.3 | -2.4 |
| 10 | Hard | Centre | 5-10 | 91.4 | 171.3 | 79.6 | 44.3 | -1.8 |
| 11 | Soft | Edge | 5-10 | 91.4 | 102.1 | 12.2 | 7.8 | -1.4 |
| 12 | Hard | Edge | 5-10 | 91.4 | 95.7 | 47.3 | 18.3 | -0.2 |

*Residuals are positive unless stated otherwise

The majority of the reported results are consistent with the known masses. However there are a few exceptions and anomalies, as detailed below.

For the AE4043/1 source, at the centre of a soft matrix the reported Pu mass of 0.052 g +0.007 g -0.005 g is 6.7 standard deviations below the known mass of 0.099g. The expected measured mean value is close to the +3 s.d. level because the source is at the point of lowest response, the centre of the drum i.e. 0.052 g +3x0.007 g = 0.073 g. There is only a small Pu self absorption effect for the AE4043/1 due to its size and shape (see section 3.3.3). However, there is a strong effect from the attenuation from the stainless steel encapsulation. The approximate attenuation due to the curved part of the encapsulation alone is calculated to be 79.0% for detectors 1 and 3 and 82.6% for detector 2. This correction has been applied and the expected mean mass value becomes 0.0897 g. (NB. This does not include attenuation due to the base and piston of the sample.) After taking this effect into account the observed result is reasonably consistent with the expected value. The AE4043/1 source has proven difficult to match modelled and measured data due to mobility of the material in the capsule and so it is difficult to quantify the expected results for this source.

A similar method has been followed for the same source at the centre of a hard matrix (Case 2), which gives a lower result of 0.078 g due to the source being at the worst case location for this dense matrix. The remaining measurements have been analysed by using an approximate

correction factor of 0.80 for the encapsulation. The results are presented in Table 12. The encapsulation factor has been used with the calculated Pu mass, however the 129 keV and 414 keV apparent masses will be affected differently and so strictly the individual line results should be corrected prior to the Pu SAC algorithm execution; however this was not possible due to the complexity of the analysis methods for the AQ2 system.

**Table 12: Encapsulation corrected results for soft and hard matrix measurements in 205 litre drums.**

| Case | Matrix | Location | Source AE4043/ | True Mass (g) | Measured Value including CF (g) | Residuals** (s.d.) |
|------|--------|----------|----------------|---------------|--------------------------------|--------------------|
| 1 | Soft | Centre | 1 | 0.099 | 0.090* | 4.9 |
| 2 | Hard | Centre | 1 | 0.099 | 0.078* | 5.1 |
| 3 | Soft | Edge | 1 | 0.099 | 0.076 | 2.8 |
| 4 | Hard | Edge | 1 | 0.099 | 0.111 | -0.7 |
| 5 | Soft | Centre | 5 | 4.94 | 5.04 | -0.2 |
| 6 | Hard | Centre | 5 | 4.94 | 2.92 | 1.8 |
| 7 | Soft | Edge | 5 | 4.94 | 5.57 | -1.6 |
| 8 | Hard | Edge | 5 | 4.94 | 7.12 | -2.0 |
| 9 | Soft | Centre | 5-10 | 91.4 | 163.4 | -4.4 |
| 10 | Hard | Centre | 5-10 | 91.4 | 214.1 | -2.8 |
| 11 | Soft | Edge | 5-10 | 91.4 | 127.6 | -4.6 |
| 12 | Hard | Edge | 5-10 | 91.4 | 119.6 | -1.5 |

*Using the expected measured mean value of (True mass +3.Uncert)
**Residuals are positive unless stated otherwise

The 3rd and 4th AE4043/1 measurements give a closer match to the results using the measured results and the approximate correction factor, as expected, since the sample was at the edge of the drum i.e. not at the worst case location. The large uncertainty for Case 4 arises mainly from the spatial contribution to cover the possibility that the sample might have been located at the centre of the drum. The large uncertainties for Case 10 is due to a combination of the previous effect and the Pu SAC algorithm assuming the Pu is in a single lump in the high attenuation region.

## 5.8    U Measurements in a Simulated Waste Drum

The USAC method has been tested as part of the AQ2 and SILWAS to show the performance of the algorithm for a limited set of measured U sources. The sources used for these tests are the Zebra plates described in section 4.6. Sources 4012, 4009 and 4005-9 were placed at mid-height in the centre and edge of soft and hard matrix filled 205l drums.

The U mass analysis methodology for the AQ2 in SILWAS is quite complex. The post analysis engines determine the U enrichment from one of three categories. The type of isotopics is listed as 'measured' if either MGAU or USAC has run successfully, otherwise a user defined 'declared' or 'default' set are used. The results for $^{235}$U and $^{238}$U for each segment (detector) are determined separately and are indicated as either G, IR or USAC:

- G = direct gamma assay
- IR = determined from isotope ratio from MGAU
- USAC = derived from the U self-absorption engine calculations

The results are summarised in Table 13. A single lump has been assumed for all tests using the NUDS method. This non-uniformity was created from the beam-like nature of the emission from the Zebra plate as the drum rotates; the distribution shows a characteristic double hump (see Figure 56). For cases where the source is at the edge of the drum, the non-uniformity is dominated by the extreme radius in the drum giving a high response when the source passes detector 2 and very low response when it passes to the opposite side of the chamber. This is reinforced by the high attenuation in the hard matrix (see Figure 57).
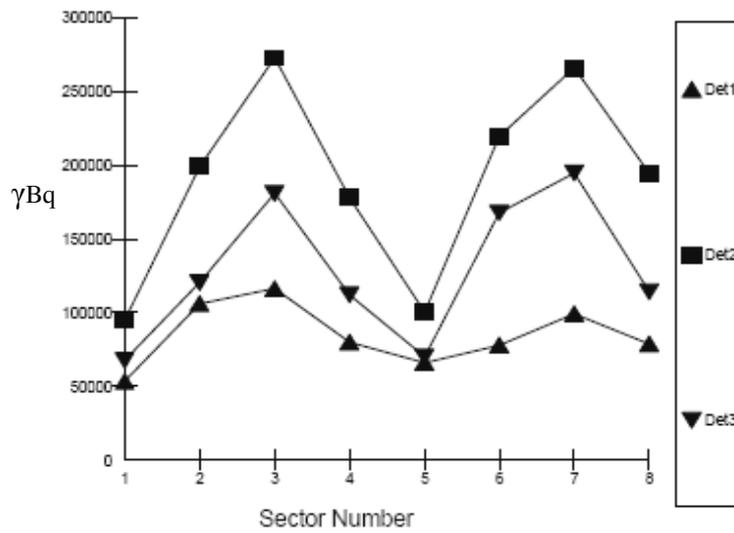
**Figure 56: NUDS plot showing the characteristic double hump effect of $^{235}$U activity from the zebra plates in a rotated drum, for 81.4 g U at the centre of a soft matrix drum (ID 9).**
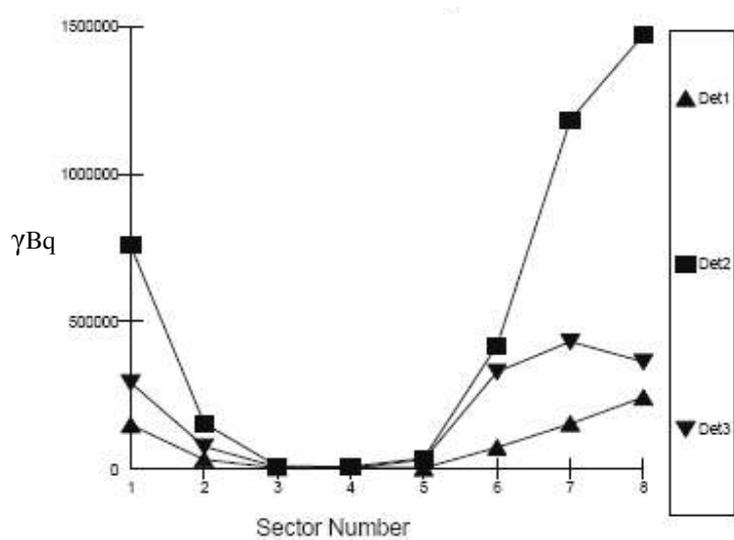


**Figure 57: NUDS plot showing the characteristic double hump effect of $^{235}$U activity from the zebra plates in a rotated drum, for 81.4 g U at the edge of a hard matrix drum (ID 12).**

**Table 13: Summary of the measured U results in the AQ2.**

| ID | U mass (g) | Location | Matrix | MGAU | Source of $^{238}$U mass* | Measured U mass (g) | +ive (1σ) | -ive (1σ) | Residual (s.d.) |
|----|-----------|----------|--------|------|--------------------------|---------------------|-----------|-----------|-----------------|
| 1  | 1.24 | Centre | Soft | No  | G,G,G       | 0.137 | 0.407  | 0.012 | 2.71 |
| 2  | 1.24 | Centre | Hard | No  | G,G,G       | 0.063 | 0.143  | 0.013 | 8.23 |
| 3  | 1.24 | Edge   | Soft | No  | G,G,G       | 0.185 | 0.709  | 0.016 | 1.49 |
| 4  | 1.24 | Edge   | Hard | No  | G,G,G       | 0.338 | 2.091  | 0.071 | 0.43 |
| 5  | 9.56 | Centre | Soft | Yes | IR,IR,IR    | 1.16  | 6.96   | 0.32  | 1.21 |
| 6  | 9.56 | Centre | Hard | No  | G,G,G       | 0.34  | 1.83   | 0.06  | 5.04 |
| 7  | 9.56 | Edge   | Soft | Yes | IR,IR,IR    | 1.45  | 11.32  | 0.38  | 0.72 |
| 8  | 9.56 | Edge   | Hard | Yes | IR,IR,IR    | 3.16  | 32.95  | 1.15  | 0.19 |
| 9  | 81.4 | Centre | Soft | Yes | IR,IR,USAC  | 24.60 | 101.18 | 2.49  | 0.56 |
| 10 | 81.4 | Centre | Hard | Yes | IR,IR,IR    | 3.93  | 50.70  | 1.15  | 1.53 |
| 11 | 81.4 | Edge   | Soft | Yes | IR,IR,IR    | 9.41  | 163.80 | 2.46  | 0.44 |
| 12 | 81.4 | Edge   | Hard | Yes | IR,IR,IR    | 14.21 | 401.30 | 3.45  | 0.17 |

\* $^{238}$U source column gives the source from each segment 1,2,3 respectively.

For measurement 1 (1.24g in the centre of a soft matrix) MGAU has not run and all segments were marked as "G" for the reported $^{235}$U which means that the mass was deduced directly from the 186 keV line (as opposed to being calculated via MGA or from USAC). The $^{238}$U mass has been reported as an MDA for this case because the line at 1001 keV was not found in the peak search, due to the low intensity of emission from this small source in relation to the sensitivity of the AQ2. The total U mass is therefore derived just from the $^{235}$U mass. The reported mass is only 11.9% of the known mass, because of self-absorption in the sample. The apparent mass from the Zebra plate sample is calculated as 14% of the true mass when viewed normally to the face of the plate. A lower value is expected when the plate is rotating.

For measurements 1, 2 and 6 the large positive TMU is dominated by the lump component, which is based upon an assumption of all the measured activity being concentrated into a single spherical lump (worst case self-absorption) at the +3 standard deviation limit. Measurement 12 also has a very high positive TMU; this arises from the need to cover the possibility that the sample could be at the centre of this highly attenuating matrix.

Only two of the results were found to be inconsistent with the known mass (using a 3 standard deviation limit): measurements 2 and 6. These are both hard matrix drums with a relatively small

source positioned at the centre of the drum. The difference between the known and reported masses arises from the method of computing the uncertainties in which the spatial variation and lump self-absorption are combined in quadrature as though the two sources of error were uncorrelated. For the test case these two extremes occur simultaneously, resulting in under-reporting. The probability of this combination arising in real waste is sufficiently low that this is considered to be an acceptable result.

Measurement 9, detector 3 is the only example where the 1001 keV line for $^{238}$U was found in the peak search and consequently USAC was able to run successfully and resulted in the measured mass being closer to the true mass than if it had not run. However these measurements use DU sources where the 1001 keV intensity is small.

The majority of the tests reported uranium only from the $^{235}$U line at 186 keV, the sample mass matrix and count times (900s) being such that the weaker 1001 keV was not detected. This is not expected to be the case for other U enrichments with longer count times. Where both lines have not been detected and the self-absorption correction could not be performed, a lump correction has been used based upon a worst-case scenario of a single lump (or several lumps, depending on the system set-up). This method produces large positive uncertainties that encompass the true mass of the sample, but may be reduced if a more conservative estimate of the number of lumps is able to be made.

# 6  CONCLUSIONS AND FUTURE WORK

In this thesis a number of new and enhanced algorithms have been proposed for the post-assay analysis of nuclear waste. The main sections and conclusions are discussed below. These methods have been incorporated into the analysis algorithms for a drum assay system which has undergone factory calibration and is currently under evaluation at a nuclear installation using actual waste containing special nuclear materials and other radionuclides.

## 6.1  Pu Self-Absorption Correction

In this work we have re-examined how the plutonium self absorption correction may be derived. A mathematical approach was adopted where the nature of the study involved calculating the behaviour of a large range of lump types (shapes, compounds and densities) and letting the model reveal the correlations with promise. The results of these calculations have been fitted to a numerical SAC algorithm which has been developed into a functional self-absorption engine for Pu.

The correction method has been applied to lumps that are of simple shapes and uniform density and is based on the use of a single pair of $\gamma$-ray lines. In practice the majority of drums will contain multiple lumps with a distribution of lump shapes and sizes. This effect has been studied and the method has been found to perform well across the range.

It is recognised that implementation of a SAC in practice is a challenging undertaking. No method can be viewed as perfect. The expectation for how the SAC can improve the quality of the assay must therefore be realistic. One expression of this is in the uncertainty estimate assigned to the corrected mass. This must include the appropriateness of the underlying model for the unknown situation at hand. For example whether a single lump or a distribution of lumps may be the cause of the apparent mass discrepancy and whether all of the lumps present may be reasonably treated as being of the same shape, composition and density or not. It is recommended that an uncertainty of approximately 6% of the corrected mass should be incorporated into the Pu SAC uncertainty to account for the additional uncertainties caused by the possible existence of multiple lumps within the waste stream.

Also the lump correction must be robust and quantified against imperfections in the gross matrix correction factors applied such as may be introduced by localised shielding effects and the spatial distribution of Pu. The latter situation could arise if a lump of fissile material had been pre-packaged before being placed into the disposal drum. The Pu SAC method has therefore been examined and the model validated, by performing experimental measurements using stainless steel encapsulated sources in controlled experiments. The stainless steel encapsulated sources have been modelled in the point source model and measured directly to rule out any other effects that could affect the results, such as the location of the $PuO_2$ within the source case. A number of the sources were found to have $PuO_2$ that was mobile material within the case and so these sources were not used for the measurements.

The new Pu SAC method has been compared to the Fleissner and Infinite Energy Extrapolation methods using both modelled data and measured data using the AE4043/nn sources (after introducing a correction factor for the stainless steel encapsulation). The Pu SAC method has been found to give more accurate results than the other methods across the mass range studied. For example, for a 25g 1cm-high Pu flat-plate of density $15g.cm^{-3}$, the developed Pu correction produces a result of $(24.9 \pm 8.8)$g compared to $(19.5 \pm 0.9)$g for the Fleissner 2-line method, and $(14.7 \pm 0.4)$g for the Infinite Energy Extrapolation method. The other methods rely on various assumptions about the waste stream and lump type, unlike the proposed Pu SAC method which has been developed for a more broad applicability. The variations from the true mass for the proposed Pu SAC method depend primarily on the extent of the modelled lump types, data fitting techniques and the physical behaviour of the $M_1:M_2:M_T$ curve. The shape dependence at the high attenuation region has been found to be the most influential factor for higher-massed lumps.

The uncertainty estimate of the corrected result could be further improved if $M_2$ and $M_T$ were plotted as functions of $M_1$ (as opposed to $M_1$ and $M_T$ versus $M_2$ as used in the studied Pu SAC algorithm), for example, and the arithmetic or geometrical mean of the two results used to correct the procedural error. Alternatively, the shape dependence of the 3D plot could be utilised with further modelling and the self-absorption corrected mass determined for each material and shape in turn for a given $M_1:M_2$ pair. The set of results per shape would give a range of $M_T$s and could

be used to infer an uncertainty. This uncertainty could also be improved if more information were known about the lump type, material or the number of lumps.

The uncertainties quoted in this chapter have been determined solely from the Pu SAC algorithm itself, as described in section 3.7.1. However this should not be quoted as the uncertainty of the measured result since the Total Measurement Uncertainty (TMU) is required to include all other sources of error (see chapter 5).

The method could also be improved if a fitting technique were established to fit the $M_1$:$M_T$ curve across the range of data, although this has proved difficult in practice. If possible, a manual fit of the curve may offer the best result, particularly for highly attenuating materials, since the user may visually observe and eliminate any anomalies in the data and may fit beyond the 3D surface more accurately than a least squares approximation may offer.

The correction has been shown to perform well and is based on a firm theoretical model. The approach has been published in the proceedings of ICEM'05 (Glasgow, UK) [78] and a comparison to other self-absorption methods has been presented at ICEM'07 [79] at Bruges, Belgium. The performance of the algorithm has been tested for different modelled homogeneous matrices, and has been found to perform satisfactorily but is limited by the accuracy of the matrix correction in face of unpredictable homogeneous matrices.

As part of this work AE4043/nn Pu reference sources have been investigated and the fill-heights, density and internal arrangement have been revisited. Measurement results indicate that the $PuO_2$ powder inside the capsules is approximately constant and has an average density of (2.19±0.04) g.cm$^{-3}$. Observations of the spatial profile of sources AE4043/1, AE4043/9 and AE4043/10 indicate that the PuO2 is mobile within the capsule. This work is to be presented at the 34th Waste Management Conference in Phoenix, Arizona, 2008 [48].

## 6.1 U Self-Absorption Correction

In this work completely new uranium self-absorption approach has been developed by extending the Pu self-absorption correction method to the case of U using the 186 keV and 1001 keV lines for those cases where the $^{235}U{:}^{238}U$ ratio is known or can be determined. An empirical approach was adopted where the nature of the empirical study involved calculating the behaviour of a large range of lump types (shapes, compounds and densities) and letting nature reveal the correlations with promise. The method has been tested using both modelled and measured data.

The correction method has been applied to lumps that are uniform and is based on the use of a single pair of lines. In practice the majority of drums will contain multiple lumps with a distribution of lump sizes. A simple study of multiple lumps has been presented and has been found to perform satisfactorily if the approximate U enrichment band is known.

The method may be applied to real waste streams to provide a very significant improvement in U mass determination compared to gamma-ray assay in which no self-absorption method is being applied. The method does require either that only one type of enrichment is present in a given drum and that the enrichment of the sample is known from details of the waste stream or via spectrum analysis programs such as FRAM or MGAU or if this is not possible, the enrichment may be determined from the apparent mass data provided the enrichment may be selected from discrete enrichment categories. It has been incorporated into an actual system and we await field results. For modelled results however, the U self-absorption correction method has been found to produce results within 30% of the true mass of the sample for the lumps studied.

Modelled results highlight that the engine depends on the amount and quality of data used in the numerical modelling process. Offline analyses are always more accurate since anomalies may be removed.

The developed USAC algorithm has been published in the proceedings of ESARDA 2007, Aix-en-Provence, France [80]. A copy of this paper is attached in Appendix A.

## 6.2   Real Drum Effects

The standard methods for combining uncertainties arising from gamma waste assay systems have been extended to include:

- the use of asymmetric uncertainties for highly non-Gaussian distributions

- methods for combining the spatial and self-absorption uncertainties with the standard method errors

- a description of the methods required for combining segment TMUs in collimated and uncollimated segmented assay systems

- an approach to combining segment less-than values to give a total package result or less-than value

- an indication for how a mixture of less-than values and 'detected' results for different segments should be combined to achieve a total package result

TMU and MDA methodologies have been revisited and enhanced so that the spatial TMU correction may apply for all energies, and the MDA calculation now incorporates corrections for spatial variation and matrix attenuation. This work has been presented at the 47th INMM Conference in Nashville, Tennessee [21].

The effect of a homogeneous matrix on the performance of the Pu SAC algorithm has been observed, however unavoidable uncertainties may arise from matrix correction techniques used with the unpredictable inhomogeneous matrices expected to occur in waste packages. It may be possible to detect any extreme non-uniformities prior to gamma assay using non-destructive examination (NDE) of the drum.

A set of tests have demonstrated the AQ2 performance with $PuO_2$ and HEU sources over the mass ranges 0.099 g to 91.4 g and 1 g to 80 g respectively, using artificial soft and hard matrices. The Pu SAC algorithm and associated measurement TMUs showed results consistent with the known mass after the effect of the source encapsulation was taken into account. The majority of the U tests reported U only from the $^{235}U$ line at 186 keV, the sample mass matrix and count times (900s) being such that the weaker 1001 keV was not detected. U SAC only ran for a single

segment in one test and resulted in the measured mass being closer to the true mass than if it had not run.

The Pu and U self-absorption correction methods developed in this thesis have been designed to perform well over a large range of lump shapes, sizes and densities that may be found in waste drums. Their design has been based upon the observed apparent masses of lines from gamma ray spectra under ideal modelled conditions. In real waste drums there are a large number of factors that influence the results and increase errors in the final result, and consequently limit the accuracy that may be achieved even with perfect self absorption corrections. However, as technology advances and other corrections are developed to deal with drum effects such as matrix absorption, inhomogeneity and isotopic or enrichment determination, these combined effect of these corrections along with the developed self-absorption correction methods will prove to greatly improve the accuracy and precision of nuclear waste assay.

# REFERENCES

[1]    http://www.nda.gov.uk/help/glossary.cfm Nuclear Decommissioning Authority Glossary website (2008). Last accessed: 1/03/08

[2]    "Classification of Radioactive Waste: A Safety Guide" (1994) Published by the International Atomic Energy Agency, Vienna, 1994.

[3]    http://www.lancs.ac.uk/users/csec/isolus2/isolus4-05.htm "The UK nuclear waste classification system", Lancaster University website. Last accessed: 28/08/0

[4]    "Management of UK Low Level Solid Radioactive Waste" (2001), Radioactive Waste Managements Advisory Committee's Annual Report for 2000-2001, Chapter 5.

[5]    G. Knoll (1979) "Radiation Detection and Measurement" John Wiley & Sons, Inc.

[6]    S. Croft, R. McElroy, S Phillips, R. Venkataraman (2006) "A Review of Recent Developments in Self-Attenuation Correction Leading to a Simple Dual Energy Lump Correction Model for use in the Quantitative Gamma Assay of Plutonium" MARC VII Proceedings

[7]    P. McClelland, V. Lewis (2003) "Measurement Good Practice Guide No. 34. Radiometric Non-Destructive Assay" National Physics Laboratory, Crown Copyright.

[8]    "Passive Non-Destructive Assay Manual" Los Alamos National Laboratory, www.lanl.gov/orgs/n/n1/panda/index.shtml Last accessed: 1/08/07

[9]    I. Kaplan (1963) "Nuclear Physics" 2$^{nd}$ Edition, Addison-Wesley Publishing Company Inc.

[10]    G. Knoll (1979) Chapter 2 Radiation Interactions "Radiation Detection and Measurement" John Wiley & Sons, Inc.

[11]    K. Siegbahn (1955) "Beta and Gamma-Ray Spectroscopy" North Holland Publications Co., Amsterdam

[12]    J. Hubbell (1969) "Photon Cross Sections, Attenuation Coefficients and Energy Absorption Coefficients for 10keV to 100GeV" NSRDS-NBS 29.

[13]    F. Bronson, B. Young, V. Atrashkevich "ISOCS Mathematical Calibration Software for Germanium Gamma Spectroscopy of Small and Large Objects" (2007), American Nuclear Society Annual Meeting.

[14]    Private communication with B. Young of Canberra Industries, 800 Research Parkway, Meriden, CT 06450.

[15]    M. Berger et al (1990) "XCOM: Photon Cross Sections Database" National Institut of Standards and Technology website. http://physics.nist.gov/PhysRefData/Xcom/Text/XCOM.html Last accessed: 10/01/06.

[16]    Standard Genie2000 V3.0 example files: NaIdemo and NBSStd

[17]    http://cat.middlebury.edu/~PHManual/gamma.html "Gamma Ray Spectroscopy with NaI(Tl) and Ge(Li) Detectors" (1992), Department of Physics, Middlebury College website. Last accessed: 25/10/05

[18]    "General Theory and Introduction to Gamma/Alpha Spectroscopy" (2004), Canberra Eurisys European Support Group training notes.

[19]    "Genie 2000 Customisation Tools Manual" (2001) Canberra Industries, Inc.

[20]    S. Croft, R. McElroy "The Calibration of Segmented Gamma Scanners using Rod Sources" (2005), Waste Management Conference '05, Tucson, AZ.

[21]    D. Curtis, M. Wormald, S. Croft "An Integrated Method for Treating Uncertainties and Less-Than Values in the Gamma Assay of Fissile Material Waste" (2006), INNM 47 2006.

[22]    R. Mayer, H. Rollen, B. Gillespie, L. Hordijk "Calibration of an IQ3 Gamma-Ray Measurement System for Safeguards Measurements at Pelindaba, South Africa" (2004) INMM 45, 2004.

[23]    F. Bronson "$Q^2$- A Very Low Level Quantitative and Qualitative Waste Assay and Release Certification" (1990) WM'90, Tucson, AZ.

[24]    J. Veilleux, D. Cramer "Comparison of Gamma and Passive Neutron Non-Destructive Assay Total Measurement Uncertainty Using the High Efficiency Neutron Counter" (2005) INMM, Phoenix, AZ

[25]    H. Menlove, D. Beddingfield, M. Pickrell, D. Davidson, R. McElroy, D. Brochu "The Design of a High-Efficiency Neutron Counter for Waste Drums to provide Optimized Sensitivity for Plutonium Assay"

[26]    "Broad Energy Ge Detector" www.canberra.com/Products/485.asp Canberra's corporate website. Last accessed: 1/8/07

[27]    B. Young "Nonuniformity Detection Software" (1995) Version 3.2. Unpublished Software Requirement Specification and Software Design Document.

[28]    "SILWAS Analysis Methodology Document" (2006) Canberra UK Ltd.

[29]    "Genie 2000 Spectroscopy Software: Operations" (2004) V 3.0, Canberra Industries, Inc.

[30]    "NDA 2000 User's Manual" (2003) V 3.2, Canberra Industries, Inc.

[31]    Private communication with M. Wormald of Canberra UK Ltd, B528.10 Unit 1, Harwell Science and Innovation Campus, Didcot, Oxfordshire OX110RA.

[32]    "Neutron Multiplicity Counter Characterization Report for a High Efficiency Neutron Counter (HENC) with Add-a-Source Option" (2004) Canberra Industries, Inc.

[33]    "Neutron Add-a-Source Calibration Report for a High Efficiency Neutron Counter (HENC) with Add-a-Source Option" (2004) Canberra Industries, Inc.

[34]    S. Croft, P. Chard (1993) "Neutronic characterisation of plutonium oxide reference samples at Harwell" ESARDA, Rome, EUR 15214 EN 511-519

[35]    S. Croft, D. Curtis, M. Wormald (2005) "The Calculation of Self Attenuation Factors for Simple Bodies in the Far Field Approximation" INMM 46 2005.

[36]    R. Auguston, T. Reilly (1974) "Fundamentals of Passive Non-Destructive Assay of Fissionable Material" Los Alamos Scientific Laboratory Report LA-5651-M

[37]    J. Parker (1981) "A Correction for Gamma-Ray Self-Attenuation in Regular Heterogeneous Materials" Los Alamos Scientific Laboratory Report LA-8987-MS

[38]    T. Prettyman, J. Sprinkle, G. Sheppard (1993) "A Weighted Least-Squares Lump Correction algorithm for Transmission-Corrected Gamma-Ray Non Destructive Assay" Nuclear Materials Management XXII, 682-690

[39]    T. Prettyman, J. Sprinkle, G. Sheppard (1994) "Performance of an Advanced Lump Correction Algorithm for Gamma-Ray Assays of Plutonium" Nuclear Materials Management XXIII, 893-896

[40]    T. Prettyman, L. Foster, R. Estep (1996) "Detection and Measurement of Gamma-Ray Self-Attenuation in Plutonium Residues" Nuclear Materials Management XXV

[41]    S. Croft, D. Curtis, M. Wormald (2005) "The Calculation of Self Attenuation Factors for Simple Bodies in the Far Field Approximation" Nuclear Materials Management XXXIV

[42]    J. Fleissner, M. Hume (1986) "Comparison of Destructive and Non-Destructive Assay of Heterogeneous alt Residues" RFP-3876, UC-15, prepared under contract for the Albuquerque Operations Office, DOE/TIC-4500

[43]    "NDA2000 Technical Reference Manual" V3.2 (2003) Canberra Industries, Inc.

[44]    J. Morel, M. Etcheverry, M. Vallee (1993) "Adaptation of the gamma spectrometry method based on the Infinite Energy Extrapolation to the measurement of small amounts of plutonium in wastes" 15th Annual ESARDA meeting

[45]    D. Crossley, A. Fudge, J. Peckett, R. Wiltshire, A. Wood (1991) "The Preparation and Characterisation of Plutonium Oxide Reference Material for Non Destructive Analysis" AEA Technology AEA-FS-00374(H)

[46]    S. Croft, P. Chard (1993) "Neutronic Characterisation of Plutonium Oxide Reference Samples at Harwell" 15th Annual ESARDA Meeting, P511-519

[47]    Private communication with S. Croft of Canberra Industries, 800 Research Parkway, Meriden, CT 06450.

[48]    D. Curtis, S. Croft, M. Wormald (2008) "A Non-Destructive Investigation of Pu Reference Items used for Calibration" To be presented at Waste Management '08, Phoenix, AZ.

[49]    http://www.canberra.com/products/835.asp Genie[TM] 2000 Gamma Analysis Software, Canberra website. Last accessed: 10/08/06

[50]    Canberra UK Factory Acceptance Tests at Harwell.

[51]    J. Wood (1982) "Computational Methods in Reactor Shielding" Pergamon Press p364-5

[52]    E. Friend (1956) "Sorting on Electronic Computer Systems" Journal of the ACM 3(3) 134-168

[53]    J. Green, D. Mergerison (1977) "Statistical Treatment of Experimental Data" Chapter 5, Elsevier Scientific Publishing Company.

[54]    http://www.curvefitting.com/datafit.htm Oakdale Engineering website. Last accessed 3/08/07.

[55]    J. Hansen (2004) "Tomographic Gamma Scanning of Uranium A New Lump Correction Technique" 7th International Conference on Facility Operations - Safeguards Interface

[56]    R. Hagenauer (1986) "Nondestructive assay of uranium in infinitely-thick material" Nuclear Instruments and Methods in Physics Research A242, p574-576.

[57]    J. Rackham, J.Dockray, T. Shaw, S. Morgan (2005) "Improvements in the accuracy of the U235 measurement in Drigg plutonium contaminated material (PCM) waste drums"; The 10th International Conference on Environmental Remediation and Radioactive Waste Management, ICEM05-1101, Glasgow.

[58]    A. Bosko, S. Croft, E. Alvarez "Comparison of MGA and FRAM for radioactive waste characterisation" (2006) INMM 47, 2006, Nashville, TN.

[59]    S. Myers, G. Butler, T. Sampson, D. Vo, D. Mercer, T. Wenz, W. Geist, M. Dempset, M. Gonzalez, J. Valdez, J. Blackadar, J. Bounds, S. Garner, D. Miko,B. Rooney "Using the FRAM Isotopic Analysis Code in the Real World" (2006) INMM 47, 2006, Nashville, TN.

[60]    T. Sampson, G. Butler, D. Vo, T. Wenz, M. Dempsey, M. Gonzalez, S. Myers "The Use of FRAM with a Portable, HPGe Based Nuclide Identifier to Measure the Isotopic Composition of Plutonium and Uranium" (2006) INMM 47, 2006, Nashville, TN.

[61]    R. Gunnink, W. Ruhter, P. Miller, J. Goerten, M.Swinhoe, H. Wagner, J. Verplancke, M. Bickel, S. Abousahl "MGAU: A New Analysis Code for Measuring U-235 Enrichments in Arbitrary Samples" (1994) UCRL-JC-114713 IAEA Symposium on International Safeguards, Austria 1994.

[62]    R. McElroy, S. Croft, B. Gillespie, B. Young "Total Measurement Uncertainty analysis for an integrated waste assay system" (2004) INMM 45, 2004

[63]    B. Ceo, S. Stanfield, J. Wachter "Radioactive Waste Measurements: Contributors to Total Measurement Uncertainty" (2007) INMM 48, 2007, Tucson, AZ.

[64]    D. Davidson, M. Koskelo, B. Gillespie, R. McElroy, T. Nishida "Total Measurement Uncertainty for NDA for SNM in Process Materials and Waste" Canberra Industries publication.

[65]    J. Lochamy (1976) "The Minimum-Detectable-Activity Concept" National Bureau of Standards Report No. NBS-SP456.

[66]    L. Currie (1968) "Limits for Quantitative Detection and Quantitative Determination" Analytical Chemistry, Volume 40, No. 3

[67]    S. Croft, R. McElroy, B. Young, R. Venkataraman "Quantifying SGS Matrix Correction Factor Uncertainties for Non-Uniform Source Distributions" (2004) INMM 45.

[68]    R. McElroy, S. Croft, B. Young "Non Destructive Assay Box Counter" (2005) INMM 46, Phoenix, AZ.

[69]    J. Parker (1984) "The use of calibration standards and correction for sample self-attenuation in gamma-ray non-destructive assay" Los Alamos National Laboratory report LA-10045.

[70] "Sampling Theory: Sampling Distributions: Central Limit Theorem." http://library.thinkquest.org/10030/8stsdclt.htm Oracle ThinkQuest Library website. Last accessed: 21/08/07.

[71] R. Gunnick "MGA: A Gamma-Ray Spectrum Analysis Code for Determining Plutonium Isotopic Abundances. Volume 1: Methods and Algorithms" (1990) Lawrence Livermore National Laboratory, UCRL-LR-103220.

[72] R. Gunnick "MGA: A Gamma-Ray Spectrum Analysis Code for Determining Plutonium Isotopic Abundances. Volume 3: FORTRAN listing of the MGA code" (1991) Lawrence Livermore National Laboratory, UCRL-LR-103220.

[73] S. Croft, R. Venkataraman, R. McElroy, R. Thomason "Subtle Sources of Bias in Gamm-Ray Waste Assay" (2007) INMM 48, Tucson, AZ.

[74] B. Gillespie, M. Zebarth "Comparison of a Variety of Gamma Attenuation Correction Techniques for Different Waste Matrices" (1993) ESARDA 1993, Salamanca, Spain.

[75] B. Young, S. Croft, R. McElroy "The Impact of Matrix Heterogeneity on Gamma-Ray Waste Assay" (2007) INMM 48, Tucson, AZ.

[76] M. Henry, S. Croft, H. Zhu, M. Villani "Representing Full-Energy Peak Gamma-Ray Efficiency Surfaces in Energy and Density when the Calibration Data is Correlated" (2007) WM'07, Tucson, AZ.

[77] H. Zhu, S. Croft, R. Venkataraman, S. Phillips "An MCNP Based Method to Determine the Matrix Attenuation Correction Factors for a Gamma Box Counter" (2007) INMM 48, Tucson, AZ.

[78] D. Curtis, M. Wormald, S. Croft (2005) "A Numerical Approach to Pu Gamma-Ray Self-Absorption Correction" ICEM'05, Glasgow.

[79] D. Curtis, M. Wormald, S. Croft (2007) "Effects of Lump Characteristics on Plutonium Self-Absorption Correction Methods" ICEM'07, Bruges, Belgium.

[80] D. Curtis, M. Wormald, S. Croft (2007) "A Numerical Approach to Uranium Self-Absorption Correction using Lines from Multiple Isotopes" ESARDA 2007, Aix en Provence, France.

# APPENDIX A

The developed USAC algorithm, described in section 4 has been presented and published in the proceedings of ESARDA 2007 at Aix-en-Provence, France [80], with assistance from M. Wormald and S. Croft at Canberra. A copy of this paper is attached in the following pages.

# A Numerical Approach to Uranium Self-Absorption Correction using Lines from Multiple Isotopes

## D. Curtis[1], M. Wormald[1], S. Croft[2]

[1]Canberra UK Ltd, B528.10 Unit 1, Harwell International Business Centre, Didcot, Oxfordshire, OX11 0TA, UK
[2] Canberra Industries Inc, 800 Research Parkway, Meriden, CT 06450, USA
E-mail: debbie.curtis@canberra.com

*Abstract:*

*This paper extends a numerical method developed for Pu self-absorption correction (SAC) to non-destructive gamma spectrometry measurements of waste to apply to the case of uranium for special cases. If it is known that there are only a small number of possible uranium enrichment types that are present within a waste drum, and only one type is present in any given container, then it has been demonstrated that the apparent masses of different isotopes may be used to determine which enrichment is present. The SAC method used for Pu may then be applied using lines from different U isotopes.*

*A point kernel gamma-ray transport computer code has been used to model emission rates from U lumps with a range of masses from 0.001g to 350g and various shapes. A set of 3-Dimensional surfaces have been generated from the results for the true mass expressed in terms of the apparent masses obtained from the 186keV and 1001keV lines for different enrichment types (e.g. DU, natural and HEU). In the proposed U SAC method these surfaces are used to determine the true mass by a dedicated de-convolution technique. The surface to be used is selected by the determined enrichment.*

*The method has been tested against computer modelled data and against some measured data for HEU samples and the results are presented.*

**Keywords:** NDA, Waste, Self-Absorption, Uranium

## 1. Introduction

Although a significant amount of work has been performed on self-absorption of Pu gamma-rays in various materials, especially in relation to the differential attenuation of the viable lines, a standard correction technique for U SAC has not yet been developed. Recent work by Croft et al. [1] and Hansen [2] emphasise the interest in this problem and suggest that new and promising methods of U self-absorption correction (SAC) are currently being investigated e.g. by comparing the closely spaced X-ray lines from Th and U. If the sample may be identified as being between the extremes of 'dilute' or infinitely thick [3,4] then it may be possible to apply a pre-determined self-absorption factor (SAF) in order to obtain a compensated assay value.

Another possible method is to use the Infinite Energy Extrapolation (IEE) method [5], or a variation of it, whereby the apparent assay mass is plotted against the reciprocal of the energy, for example, and extrapolated to non absorbing conditions which is taken as 'infinite energy' on the basis that generally in the energy range of interest mass attenuation coefficients are falling rapidly with energy. This approach has been used successfully for Pu since $^{239}$Pu emits a number of lines of known abundance which are reasonably well spaced in energy. This may be adapted to use the 143keV, 163keV, 186keV and 205keV lines from $^{235}$U, however these lines are comparatively close together and do not offer as much differential absorption (sensitivity to lump size) as experienced by the 129keV and 414keV lines

from $^{239}$Pu and also the dynamic range is limited by similar saturation points. Furthermore the branching ratios are not as favourable. We use the IEE method as a comparison in section 5.

An alternative to estimating and applying a SAC from the measurement data of a particular assay could be to simply introduce an additional uncertainty component, a "lump" parameter for example. This component may be incorporated into the Total Measurement Uncertainty (TMU) associated with the measurement to account for the case where all the U in an item is concentrated into a single spherical (worst case) lump, depending on what may be known about the origin of the item. In so doing the assay value can be bounded in a way that may satisfy certain safety and transport criteria. But as a quantification approach it does not represent the best estimate value.

This paper extends a numerical method for Pu self-absorption [6] to apply to the case of U where the enrichment is known or at least falls into classes or bands. If only a limited number of possible enrichment types may be present within a waste stream and only one type is present in any given drum, then it has been demonstrated that the uncorrected characteristic lines may be used to determine which enrichment is present. This is possible if the source of the waste is known sufficiently well (e.g. from records or knowledge of the facility), however in principle the enrichment could be any value. Once the enrichment has been established the two-line SAC method developed for $^{239}$Pu may be applied. The two main lines used to measure uranium in waste drums are 186keV line from $^{235}$U and the 1001keV line from $^{238}$U (produced from the decay of $^{234}$Pa$_m$ as a second daughter of $^{238}$U if in equilibrium, which should always be the case for waste measurements). Although there are other $^{235}$U lines available (143.8keV, 163.3keV and 205.3kev), the 186keV line is the most prominent of the set, close enough to the U K-edge (115.6keV) to suffer a significant effect from photo-electric absorption for U and offers good differential absorption.

A program has been created to test a new U SAC method based upon the assumption that a waste stream contains only three possible enrichment categories. It has then been extended to perform with any known enrichment, which must be known either from details of the waste stream's origin or using relative isotopic spectral analysis techniques such as employed in the MGAU or FRAM codes.

## 2. U Modelling

A point-source point-detector model has been used to model the behaviour of single unencapsulated U lumps. The model divides the lump up into a specified number of voxels (volume elements), defined by radial, polar and height integration intervals for cylindrical lumps, and lateral, depth, height and rotation integration-intervals for cuboidal lumps.

The model sets the gamma-ray production in each voxel as the volume of the voxel and computes the probability of the gamma-rays reaching the detector without scattering or absorption – both processes remove the line from the detected spectral peak. The voxel contributions are integrated over the whole lump and the calculation repeated with the material density in the attenuation function set to zero, the ratio of these results giving the SAF (self-attenuation factor) for that gamma-ray line. The scattered component of the gamma-ray flux reaching the detector can safely be ignored when high resolution Ge detectors are used in the measurement of the 186keV and 1001keV lines since the scattered photons are almost invariably energy degraded to the continuum below the photo-peak.

It shall be assumed here for illustrative purposes that there are only three possible enrichment categories within waste drums. Although real waste may have different enrichments, modelling and correction may be performed for any U enrichment value, provided the possible enrichments can be grouped into discrete values or bands from prior knowledge of the waste types present. Three commonly used enrichments have been chosen to demonstrate the way enrichments can be estimated from apparent enrichments and consequently fed into a U SAC. The three chosen enrichment types for the purpose of the investigation are: Depleted uranium (DU) 0.5% $^{235}$U, Intermediate enrichment uranium (IEU) 40% $^{235}$U and High enrichment uranium (HEU) 93% $^{235}$U.

The self-absorption curves for U (of density 18.7g.cm$^{-3}$) have been modelled to determine the SAF and hence apparent masses at the 186keV and 1001keV lines for the three possible enrichment types: DU, IEU and HEU. The uncorrected self-absorption behaviour of bare U lumps of various dimensions has been calculated using the point kernel model, over the mass range of 0.1mg to 350g for the following geometries:

- Cylinders with diameter equal to height, with dimensions ranging from $2.0 \times 10^{-4}$m to $2.9 \times 10^{-2}$m
- Square faced plates with a fixed depth of 1mm, with heights ranging from $7.0 \times 10^{-5}$m to $1.6 \times 10^{-3}$m
- Rods with a fixed length of 0.1m, with diameters ranging from $8.3 \times 10^{-6}$m to $1.5 \times 10^{-2}$m
- Cubes of side length ranging from $2.0 \times 10^{-4}$m to $2.7 \times 10^{-2}$m
- Plates of fixed square face length $3.0 \times 10^{-3}$m, with heights ranging from $6.0 \times 10^{-7}$m to $5.9 \times 10^{-3}$m
- Plates of fixed square face length $3 \times 10^{-2}$m, with heights ranging from $6.0 \times 10^{-7}$m to $2.1 \times 10^{-2}$m
- Plates of fixed square face length 0.1m, with heights ranging from $5.0 \times 10^{-7}$m to $1.9 \times 10^{-3}$m
- Plates of fixed square face length $7 \times 10^{-2}$m, with heights ranging from $5.0 \times 10^{-7}$m to $3.8 \times 10^{-3}$m
- 6cm high cylinders, with diameters ranging from $1.1 \times 10^{-5}$m to $2.0 \times 10^{-2}$m
- 1cm high cylinders, with diameters ranging from $2.6 \times 10^{-5}$m to $4.9 \times 10^{-2}$m
- Square faced plates with a fixed depth of 1mm, with heights ranging from $4.0 \times 10^{-5}$m to $7.9 \times 10^{-2}$m
- Zero attenuation geometry (186keV mass = 1001keV mass = true mass)

## 2.1. Results

Figure 1 shows the relationship of apparent masses at 186keV ($M_1$) and 1001keV ($M_2$) and the true U mass ($M_T$) for the selection of shapes for three enrichment types. The DU, IEU and HEU sets are labelled and although the 3-D surfaces for the latter pair are very close together they do not overlap. This may not be the case for other sets of enrichment types however.
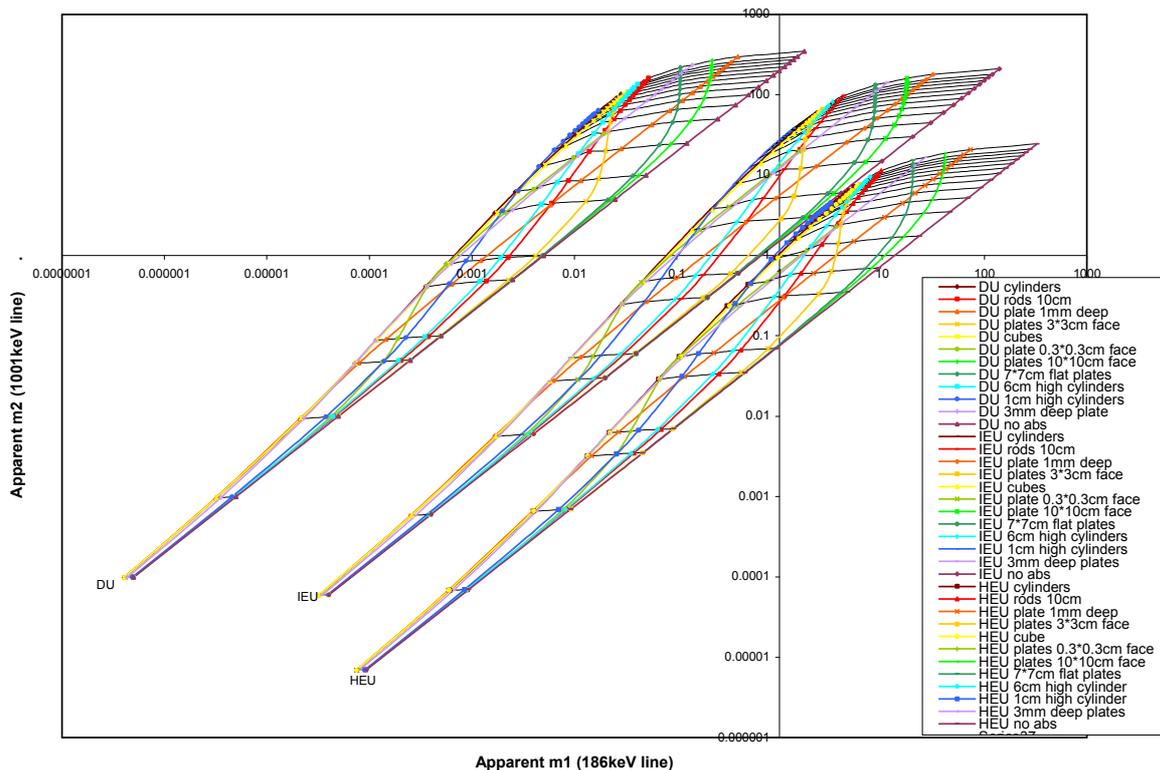


**Figure 1:** Uranium self-absorption for three specified enrichment categories.

Each set of curves follows a similar pattern to those seen for Pu as the U becomes more self-absorbing. The near-horizontal black curves are a selection of constant true mass lines. The diagonal lines (for which $M_2 = kM_1$) are the cases of no attenuation where $M_1$ divided by the [235]U enrichment is equal to $M_2$ divided by the [238]U enrichment. Very small mass lumps will lie on or close to the no absorption lines, and as the lump size increases and the shapes become more attenuated (for the 186keV line), the curves migrate towards the opposite upper edge of the surfaces. As the

mass and lump size increase further they saturate and the points on the curve bunch closer together. No points should lie outside the respective surfaces for the relevant enrichment type.

Based on this database of calculated results a U SAC method (a software engine) has been developed to calculate the mass of U from the two apparent masses $M_1$ and $M_2$, and has been used to demonstrate the effectiveness of the new self-absorption technique. The new method is described briefly below.

## 3. The USAC Algorithm

A Borland[TM] Delphi program has been created to calculate the enrichment based upon the inputted apparent masses (these are the assay results fully corrected for matrix attenuation in the drum and other factors as best as we are able). The apparent enrichment $E_{app}$ may be calculated as:

$$E_{app}(\%) = \frac{m_{U235}(g)}{m_{U235} + m_{U238}(g)} \times 100$$

where $m_{U235}$ is the apparent mass of $^{235}U$ from the 186keV line and $m_{U238}$ is the apparent mass of $^{238}U$ from the 1001keV line. Due to self-absorption the apparent masses will always be less than the true mass and the less energetic line will always be affected more. Consequently the apparent enrichment should be less than the true enrichment (although this may not strictly be the case due to statistical uncertainties in the measurement) where self absorption is significant, and the apparent enrichment may be used to select an enrichment category, provided the regions on the apparent 186keV mass versus apparent 1001keV mass surface do not overlap for the different enrichments.

Using this enrichment category the program will scale the $M_1$ (apparent mass from the 186keV line), $M_2$ (apparent mass from the 1001keV line) and $M_T$ (the true mass) values accordingly and determine cubic spline fits for each enrichment and shape combination, plotting curves for $M_T$ versus $M_2$, and $M_1$ versus $M_2$ to obtain the self-absorption corrected mass and $M_1$ as functions of $M_2$. Using the calculated cubic spline fits and the measured 1001keV line apparent mass ($M_2$) we may take a slice of the 3-D surface with varying true mass and $M_1$ and plot the ($M_1$, $M_T$) pairs calculated. If the locus between successive points may be approximated as a straight line the SAC U mass may be determined from the measured 186keV line apparent mass ($M_1$).

## 4. Modelled Results

The USAC algorithm has been tested with modelled data for three new lump types with a mass range of 0.1mg to 350g. These lumps are 15mm high cylinders, 2mm fixed depth flat plates and 40mm high cylinders. It is necessary to 'test' the method against modelled results for shapes etc that are **not** included in the base data set or 'incestuously' over-optimistic results may be obtained.

The modelled data for each set have been converted for DU, IEU and HEU and run through the U SAC engine. In each case the engine chose the enrichment type correctly. The results are shown in Figure 2.

156
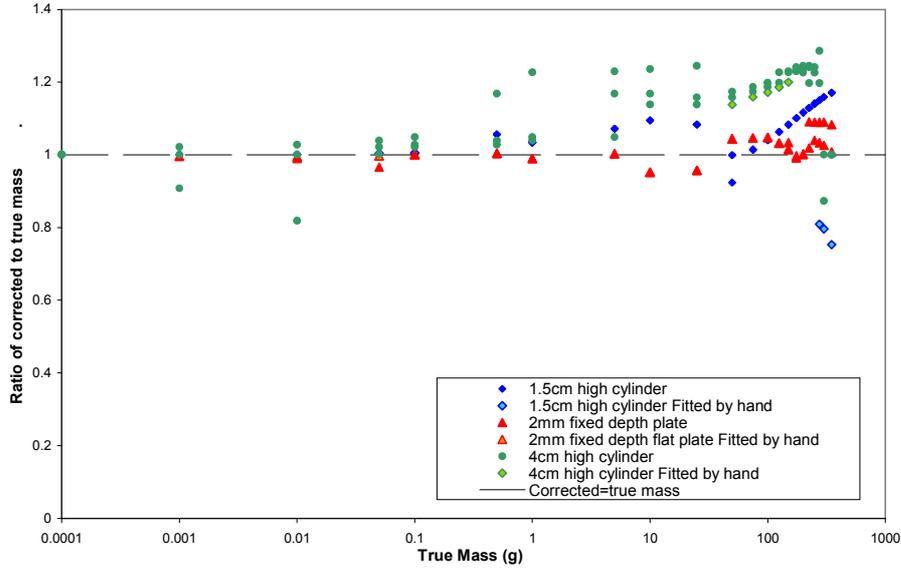
**Figure 2:** Graph showing the calculated to true mass ratio using the developed U SAC method.

.

For each new lump type modelled, there are cases where the engine begins to underestimate the true mass result since the data points fall just outside the 3-D surface and the linear least squares extrapolation method is used to determine the true mass. Since the data points in the high attenuation region are clustered the least squares extrapolation does not offer a good fit to the whole curve.

The results for the 2mm deep plates all fall within 10% of the true mass across the range of masses. The results for the 40mm high cylinders have been found to overcorrect at higher masses, and the results for the 15mm high cylinders begin to overestimate with increasing mass above 100g. Overall the USAC engine appears to work well and the results are within approximately 25% of the true mass which is impressive in the context of the bias that would result without compensation.

## 5. Experimental Results

The program outlined in the previous section has been extended to be applicable for any possible enrichment. The enrichment must be stated by the user prior to its execution and so must be determined externally. Where the enrichment as been determined from the spectral data and cannot be categorised into a discrete enrichment type, there will be an additional uncertainty associated with the $^{235}$U and $^{238}$U isotopic estimations. For these cases the uncertainty in the total U SAC mass has been determined from the standard method for combining uncertainties from multiple independent variables by:

$$\sigma_{M_T}{}^2 = \left(\frac{\partial M_T}{\partial M_1}.\sigma M_1\right)^2 + \left(\frac{\partial M_T}{\partial M_2}.\sigma M_2\right)^2 + \left(\frac{\partial M_T}{\partial En_{235}}.\sigma En_{235}\right)^2 + \left(\frac{\partial M_T}{\partial En_{238}}.\sigma En_{238}\right)^2 (g)$$

where $En_i$ is the estimated enrichment of the sample for isotope $i$, $\partial M_1 = 0.001 \times M_1$, $\partial M_2 = 0.001 \times M_2$, $\partial En_i = 0.001 \times En_i$, $\partial M_T$ in each case are the changes in $M_T$ when $\sigma M_T$ is mapped through the USAC process, $\sigma En_i$ is the uncertainty in the enrichment for isotope $i$, and $\sigma M_n$ are the inputted uncertainties in the 186keV or 1001keV masses at the one standard deviation level providing the total uncertainty in $M_T$ is at one standard deviation.

The USAC code has been tested using U 'Zebra plates' (sections of fuel fabricated for an experimental reactor) with an enrichment of approximately 93%. The source thickness has been estimated based upon the known mass and areas of the plates and an assumed density of 18.7g.cm$^{-3}$ for U metal.

**Table 1:** Uranium Zebra plate data including total U masses and plate dimensions.

| ID | U mass (g) | U-235 mass (g) | Dimensions (mm) |
|---|---|---|---|
| 4005 | 17.91 | 16.66 | 25 x 25 x 1.5 |
| 4006 | 17.94 | 16.68 | 25 x 25 x 1.5 |
| 4007 | 17.99 | 16.73 | 25 x 25 x 1.5 |
| 4008 | 17.95 | 16.69 | 25 x 25 x 1.5 |
| 4009 | 9.56 | 8.89 | 25 x 13.5 x 1.5 |
| 4010 | 4.21 | 3.91 | 11 x 14.0 x 1.5 |

The sources have been measured using a 20mm thick, 70mm diameter BeGe detector, with a polyethylene end cap, at a distance of 100mm from the end cap, in the following combinations:

- 4010          mass = 4.21g
- 4009          mass = 9.56g
- 4008          mass = 17.95g
- 4008-9        mass = 27.51g
- 4007-8        mass = 35.94g
- 4007-9        mass = 45.5g
- 4006-8        mass = 53.88g
- 4006-9        mass = 63.44g
- 4005-8        mass = 71.79g
- 4005-9        mass = 81.35g

Multiple sources have been stacked behind one another, positioned vertically with the largest face of each towards the detector and with the smaller sources in the group closest to the detector. The apparent masses for the 143.8keV, 163.3keV, 185.7keV, 205.3keV and 1001keV lines have been determined and used with the USAC program for non-discrete enrichments. The data have also been analysed according to the Infinite Energy Extrapolation method with both linear and polynomial fits being applied to carry out the extrapolation to 1/E=0. The results are shown in Figure 3.

The sources have been measured statically (non-rotating) with the face of the source approximately parallel to the face of the detector, whereas the developed U SAC program has been designed to work with lumps which present a changing orientation to the detector (as they are moved along with the contents of the drum as it is rotated in front of the detector and also as the drum is viewed from several vertical positions) and so the apparent masses at all energies are larger than expected for a rotated geometry, with a stronger effect experienced by the lower energy lines. However, the corrected result using the USAC method is more dependent on the change in 1001keV apparent mass and so the overall effect is the method still performs reasonably well. In a sense the 186keV line is indicative of the projected surface area for reasonably large lumps and the 1001keV is more of a bulk indicator in this regime.
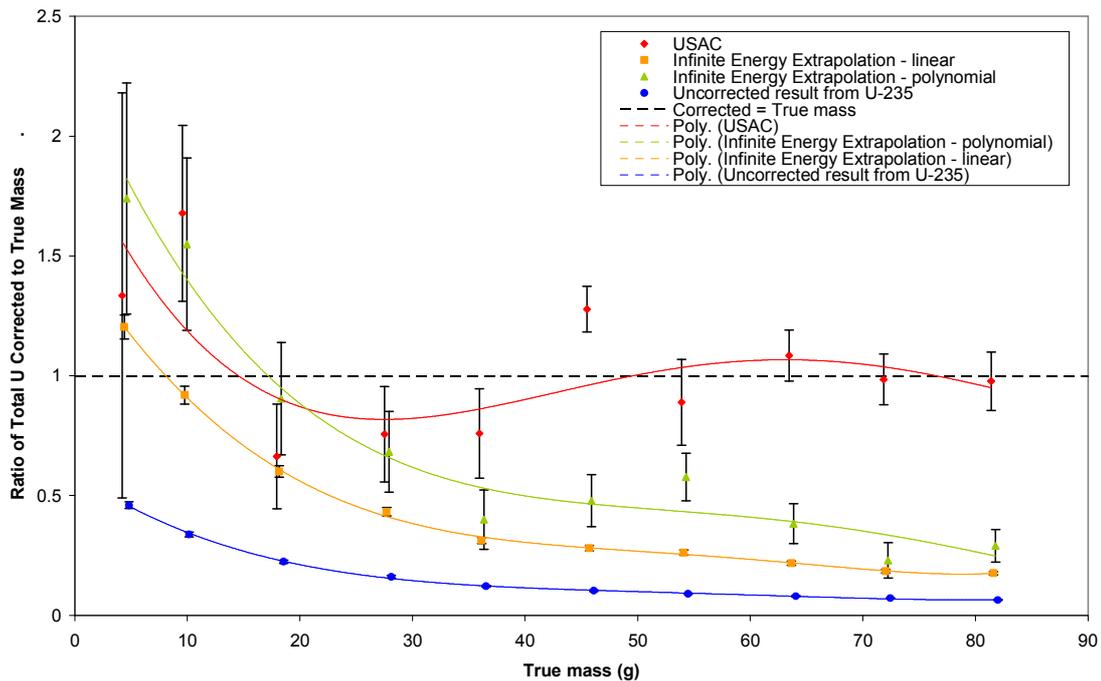
**Figure 3:** The ratio of corrected to true total U mass as a function of true mass for U Zebra plate measurements showing USAC and Infinite Energy Extrapolation correction methods

Figure 3 shows the total U results calculated with the USAC method described. The uncorrected results begin at half of the true mass and reduce continuously as the mass increases. Both IEE fitting methods produce results which reduce to below 0.3 of the true mass for higher massed samples. This may be because the line energies used for the fitting methods are small and so there is not a high energy (less attenuated) line to improve the extrapolation to $1/E = 0$, resulting in a lower U mass from these more attenuated lines.

The USAC algorithm has been shown to perform very well, with the majority of results within 35% of the true mass, offering a significant improvement compared to the other methods. The largest deviations from the true mass have most likely occurred mainly due to statistics since HEU produces very few 1001keV counts, as indicated by the large error bars for these measurements. The sources were measured for live times of between 600s and 1200s depending on the mass of the sample, whereas in real assay systems, especially with heavier matrices, the practical counting time may be too short to obtain enough 1001keV counts for HEU unless the U mass is very large. However, for lower enrichment U samples (with a higher [238]U content) would provide improved statistical accuracy.

One advantage to the USAC method is that it may be used for mixed U and Pu drums without difficulty since it uses only the 186keV and 1001keV lines, whereas the IEE methods and the X-ray fluorescence methods can both suffer from interference from Pu lines.

## 6. Extension to Multiple Lumps

The extension to waste packages that contain U in the form of multiple lumps (which may be of different sizes, shapes and materials) has been investigated. In practice it is rare indeed for a waste item to contain only a single piece of fissile material. Due to the high degree of non-linearity observed in the model, the combination of a series of smaller lumps was expected to produce a smaller self attenuation factor than that expected for a single large lump of equal mass and therefore the model was expected to underestimate the total U in a sample. Thus far we have

considered the impact on DU result only but due to the nature of the algorithm the other enrichment results ought to behave similarly.

The apparent 186keV and 1001keV masses for a number of material/shape combinations were summed and used as input for the algorithm to see how it would behave for multiple lumps. These combinations include several lumps of the same material and shape, plus random mixed numbers and types of lumps over the range of masses and shapes studied in the USAC algorithm development, plus the series of newly modelled data sets used for the modelled results. The results are presented in Figure 4.
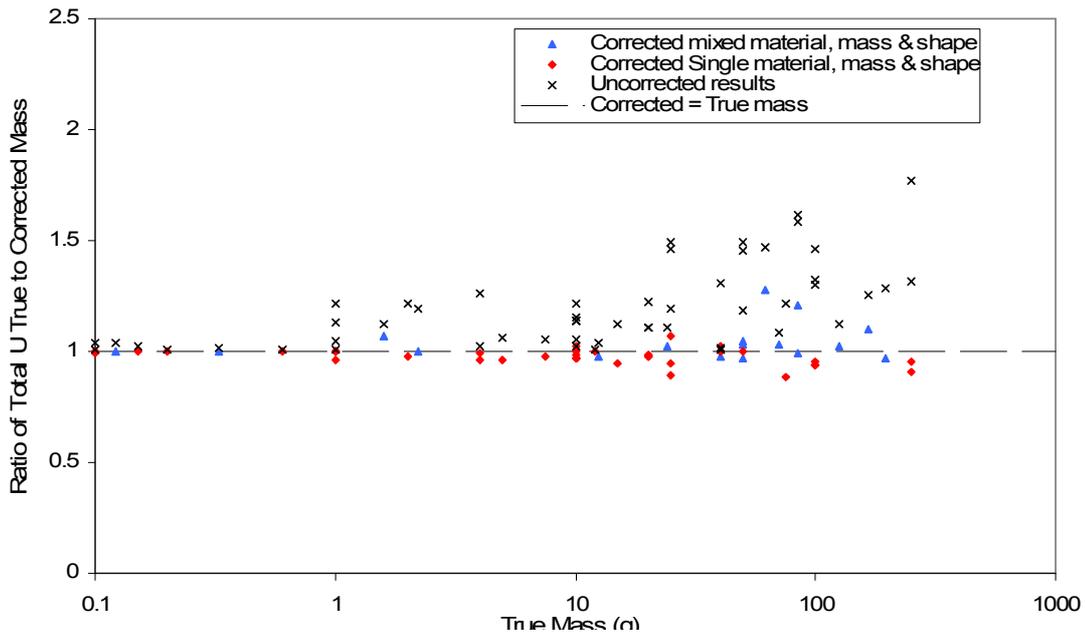


**Figure 4:** Plot of the ratio of true to corrected total U mass versus the total true mass for random combinations of lumps collated from independently-treated single lump modelled data for DU.

The uncorrected total U mass (derived form the186keV apparent masses and isotopics) are also plotted as a comparison. The results do not produce perfect ratios of one, as expected, because as the individual lumps are combined their total 186keV apparent mass will be higher than that of a single lump of equivalent mass, whereas the 1001keV apparent mass will remain relatively similar. Consequently the corrected mass of the combination of lumps is underestimated, demonstrated by approximately 70% of the USAC corrected data points. The remaining corrected masses lie above the ratio equals one. This is line due to fluctuations in the data points in the high attenuation region of the $M_1$:$M_2$:$M_T$ plot.

It should be noted that these lump combinations have been performed by summing the apparent masses of individual lumps, assuming that all lumps are independent and the gamma rays from each lump are not attenuated by any other lump on their path to the detector. However this may not be the case in real waste drums and the resulting apparent mass may, conceivably at least, be attenuated more than for the examples shown above.

The method appears to work well for multiple lumps of various compositions. All of the modelled results are within 28% of the corrected equal to true mass line, with 79% of the modelled results achieving values within 5% of the true mass. These observations could be developed with a more detailed study to implement a contribution to the TMU of the sample from the U self-absorption in the case of multiple lumps. For example, if a 1-σ uncertainty is required by the user (68% of the results should lie within the area if a Gaussian distribution applies, for example), this equates to a 3.5% uncertainty if the uncertainty is assumed to be constant across the mass range.

It may also be observed that the variation from the corrected equal to true mass line appears to increase with increasing true mass and so the TMU contribution from multiple lumps could be refined to be a function of the apparent mass with a more in-depth study.

# 7. Conclusions

In this work we have re-examined how the self absorption correction may be derived and have extended a Pu self-absorption correction method to the case of U using the 186keV and 1001keV lines for those cases where the $^{235}$U:$^{238}$U ratio is known or can be determined. An empirical approach was adopted where the nature of the empirical study involved calculating the behaviour of a large range of lump types (shapes, compounds and densities) and letting nature reveal the correlations with promise. The method has been tested using both modelled and measured data.

The correction method has been applied to lumps that are uniform and is based on the use of a single pair of lines. In practice the majority of drums will contain multiple lumps with a distribution of lump sizes. A simple study of multiple lumps has been presented and has been found to perform satisfactorily.

The method may be applied to real waste streams to provide a very significant improvement in U mass determination compared to gamma-ray assay in which no self-absorption method is being applied. The method does require either that the enrichment of the sample is known from details of the waste stream or via spectrum analysis programs such as FRAM or MGAU, or if this is not possible, the enrichment may be determined from the apparent mass data provided the enrichment may be selected from discrete enrichment categories – iteratively if need be.

The USAC engine has been incorporated into an assay system and we look forward to reporting future results of plant performance. In addition the TMU estimation and performance estimates for lump distributions are being refined.

# 8. References

[1] S. Croft, D. Curtis, M. Wormald; "The Calculation of Self Attenuation Factors for Simple Bodies in the Far Field Approximation"; *Nuclear Materials Management XXXI,* 2005.

[2] J. Hansen; "Tomographic Gamma Scanning of Uranium A New Lump Correction Technique"; *7$^{th}$ International Conference on Facility Operations - Safeguards Interface*; 2004.

[3] R. Hagenauer; "Nondestructive assay of uranium in infinitely-thick material" *Nuclear Instruments and Methods in Physics Research* A242; 1986; p574-576.

[4] J. Rackham, J.Dockray, T. Shaw, S. Morgan; "Improvements in the accuracy of the U235 measurement in Drigg plutonium contaminated material (PCM) waste drums"; *The 10$^{th}$ International Conference on Environmental Remediation and Radioactive Waste Management; ICEM05-1101*, Glasgow*;* 2005*.*

[5] J. Morel, M. Etcheverry, M. Vallee ; "Adaptation of the Gamma Spectrometry method based on the Infinite Energy Extrapolation of the measurement of small amounts of plutonium in wastes"; *Safeguards and Nuclear Material Management, ESARDA*, Rome; 1993.

[6] D. Curtis, M. Wormald, S. Croft; "A Numerical Approach to Pu Gamma-Ray Self-Absorption Correction"; *The 10$^{th}$ International Conference on Environmental Remediation and Radioactive Waste Management;* ICEM'05, Glasgow; 2005.